POLITECNICO DI MILANO

School of Industrial and Information Engineering

Master of Science in Materials Engineering and Nanotechnology

SYNTHESIS AND CHARACTERIZATION OF

TWO-DIMENSIONAL ZINC OXIDE:

A SCANNING TUNNELING MICROSCOPY STUDY

Supervisor: Prof. Carlo Casari

Co-supervisor: Francesco Tumino

Master Thesis of:

Riccardo Cristina

820124

Academic Year 2014-2015

If I have seen further,

it is by standing on the shoulders of Giants

Isaac Newton

ABSTRACT

This thesis work reports an experimental analysis of ZnO nanostructures and ultrathin films on the Au(111) surface, by means of Scanning Tunneling Microscopy (STM). The ZnO/Au(111) system is obtained with two different techniques: Electron Beam Physical Vapor Deposition (EB-PVD) of metallic zinc, which is then oxidized, and Pulsed Laser Deposition (PLD), by ablation of a stoichiometric ZnO target. The study focuses on the synthesis and characterization of the two-dimensional phase assumed by ZnO in these systems, defined Graphene-like Zinc Oxide (g-ZnO), the structural and morphological properties of which are discussed thanks to high-resolution STM images. Emphasis is given to the influence of the different parameters, which characterize the deposition processes, on the morphology of the structures obtained. Experiments are carried out at different coverages, allowing the study of the growth mechanisms of this ZnO phase on the chosen substrate.

SOMMARIO

Il presente elaborato di tesi riporta un'analisi sperimentale della crescita di nanostrutture e film ultrasottili di ZnO su una superficie Au(111), tramite microscopia a effetto tunnel (STM, Scanning Tunneling Microscopy). Il Sistema ZnO/Au(111) è stato ottenuto con due differenti tecniche: deposizione fisica da vapore da fascio elettronicoo (EB-PVD, Electron Beam Physical Vapor Deposition) di zinco metallico, che è stato poi ossidato, e deposizione a laser pulsato (PLD, Pulsed Laser Deposition), tramite ablazione di un obiettivo stochiometrico di ZnO. Lo studio si focalizza sulla sintesi e sulla caratterizzazione della fase disimensionale assunta da ZnO in questi sistemi, definita ossido di zinco grafenico (g-ZnO, Graphene-like Zinc Oxide), le cui caratteristiche strutturali e morfologiche sono discusse grazie ad immagini STM ad alta risoluzione. E' stata data enfasi all'influenza dei diversi paramentri, che caratterizzano i processi di deposizione, sulla morfologia delle strutture ottenute. Sono stati eseguiti esperimenti a diversi ricoprimenti, che permettono di studiare le modalità di crescita di questa fase di ZnO sul substrato scelto.

TABLE OF CONTENTS

TABLE OF FIGURES

INTRODUCTION

This thesis focuses on the study of zinc oxide ultrathin films and nanostructures, and particularly on the synthesis of two-dimensional, graphene-like zinc oxide (g-ZnO), with the aim to improve knowledge of its morphology and the conditions in which it can be successfully obtained.

There are numerous reasons for the interest in this material, which will be briefly described. Firstly, bulk zinc oxide is itself a multifunctional material, with many technological applications: from structural ceramic to additives, to piezo electronics, etc; there are also high hopes for future developments in the field of light emission. ZnO can also form an extremely wide range of nanostructures[13].

There is also growing interest in the scientific community regarding the formation of ultrathin oxide films on metals, since the properties of these systems are determined by the combination of substrate and overlayer materials, and are further greatly influenced by the thickness of the grown film. One major motivation for the attention on these materials is their expected significance in the context of catalysis[8].

Finally, after the successful synthesis of graphene, 2D materials has been one of the fastest growing fields in material science, and the attention is now shifting to the realization of new planar materials presenting innovative combinations of properties[3]. An enormous amount of theoretical research has been carried out on these hypothetical compounds, but very few have actually been successfully synthetized, one of them being g-ZnO.

In this work, the structures were grown on the Au(111) surface, and the deposition on the gold substrate were performed both by Electron Beam Physical Vapor Deposition (EBPVD) and by Pulsed Laser Deposition (PLD). The samples were then characterized in situ by means of Scanning Tunneling Microscopy (STM). In the case of EBPVD the evaporant was made of pure zinc, which was later oxidized, whereas in PLD the target employed was composed of stoichiometric zinc oxide.

The characterization of the obtained surfaces and nanostructures required a technique characterized by an extreme spatial resolution, and STM was an obvious choice, being capable of collecting atomic resolution images. In fact, it is one of the most important instruments for experimental research in the fields of nanotechnology and surface science.

Gold, and specifically the Au(111) surface, was considered a suitable substrate for this thesis work, since it shares with g-ZnO a hexagonal symmetry and possesses similar lattice dimensions, which should help stabilize the two-dimensional conformation of the oxide. Moreover, this substrate is well-known in surface science, it is chemically resistant to oxidation and corrosion and presents an easily recognizable "herringbone" surface reconstruction, which can sometimes give place to preferential nucleation.

Based on all of the aforementioned considerations, this thesis work aimed to synthetize and characterize graphene-like zinc oxide nanostructures on the Au(111) surface, carrying out the depositions by EBPVD and PLD and analyzing the results by means of STM imaging.

A few recent papers have reported similar studies, and will be discussed thoroughly in this thesis, but the information regarding the morphology of g-ZnO, and especially the conditions for its synthesis, resulted unclear and in need of further research.

This thesis is structured in three main chapters, followed by a conclusion:

- o **Chapter 1 – Two-dimensional materials:** a brief overview is given of the peculiarities of 2D materials, along with some noteworthy examples of such compounds. Afterwards, a more focused introduction to 2D oxides is presented, and the properties of bulk zinc oxide and some of its surfaces are described. The state of the art on the theoretical and experimental studies regarding graphene-like ZnO is then reviewed; finally the thesis objectives are more specifically discussed.

- o **Chapter 2 – Synthesis and characterization techniques:** the working principles of the two deposition methods employed in this thesis, electron-beam physical vapor deposition and pulsed laser deposition are defined. A similar explanation of the functioning of scanning tunneling microscopy is then given, along with a more in depth discussion on the theoretical models for electron tunneling. It is present also a simple description of the experimental apparatus present in the laboratory.

- o **Chapter 3 – Experimental results and discussion:** the results obtained in this research are illustrated, divided according to the respective deposition approaches. A comprehensive discussion and interpretation of the experimental results can then be found.

- o **Conclusion and perspectives:** the main results and considerations are summarized, and possible further studies to be carried out on the subject of this thesis are outlined.

The synthesis processes, STM measurements, as well as their analysis, of graphene-like ZnO on Au(111) have been performed in the Micro and Nanostructured Materials Laboratory (Nanolab) of Politecnico di Milano. I personally worked on all these activities.

1 TWO-DIMENSIONAL MATERIALS

This chapter will focus on depicting the current research in the field on two-dimensional materials, especially of graphene-like zinc oxide, and on providing the reasons that led to the analysis carried out in this thesis.

To this aim 2D materials will first be introduced, along with a description of the properties of the most notable members of this category (Section 1.1), whereas in Section 1.2 the attention will shift to two-dimensional oxides.

After an overview of the structure and properties of bulk zinc oxide (Section 1.3), a presentation will be found of the results obtained by theoretical studies on two-dimensional zinc oxide (Section 1.4.1) and by experimental works on its synthesis and characterization (Section 1.4.2).

Finally in Section 1.5 the objectives of this thesis work will be more clearly defined.

1.1 INTRODUCTION TO 2D MATERIALS

The last few decades have been characterized by an ever increasing rate of development of new technologies and products, but at some point the classical, macroscopic materials were unable to satisfy the need for specific combinations of properties and also for decreased device size.

Researchers then started to study the effect of dimensionality. Dimensionality is one of the most fundamental material parameters, which not only defines the atomic structure, but has also a large impact on the properties of the material. As demonstrated by quantum physics, at the nanoscale the same compound can express completely different properties with a variation in dimensions.

Based on this, several different categories of nanostructures have been established, making nanotechnology one of the fastest growing fields in the recent years. One of this categories, 2D materials, initially didn't generate much interest, since there were great doubts about the stability of such a perfectly planar structure[1].

The synthesis of graphene, and even more its impressive properties, however, caused an explosive increase in the research carried out regarding 2D materials, which are now thought to hold the potential to usher a new era for Material Science.

This is because when heat and charge transport are confined in a plane, unique physical singularities arise which cannot be found in bulk materials, for example massless Dirac electrons, discussed later in this section.

A new range materials are available, atomically flat, mechanically, thermally and electronically stable, which can be assembled in ultra-thin devices and promise to have great influence in a large array of applications in the near future: high performance sensors, gas separation and storage, catalysis, support membranes, inert coatings, etc., but most importantly, nanoelectronics. They are also extremely interesting from a medical and biotechnological perspective[2].

Two-dimensional materials exist which belong to all typical classes of 3D materials[3], from metals to semimetals, to direct and indirect semiconductors with a variety of band gaps, to insulators, and their properties can furthermore be easily tailored for specific requirements thanks to their "all-surface" nature. This can be done by surface treatments, for example chemical functionalization, but also doping results very important for controlling the properties of a 2D material.

A quite simple way to exploit 2D materials is through the creation of nanoflakes, which are then dispersed in the chosen matrix to create higher performance composites, since many of the planar material properties are retained.

Here will be presented, as an example of the variety of properties which can belong to these compounds, three of the most important 2D materials: graphene, hexagonal boron nitride and molybdenum disulfide; an overview of ultra-thin metal oxides will be instead found in the next section.
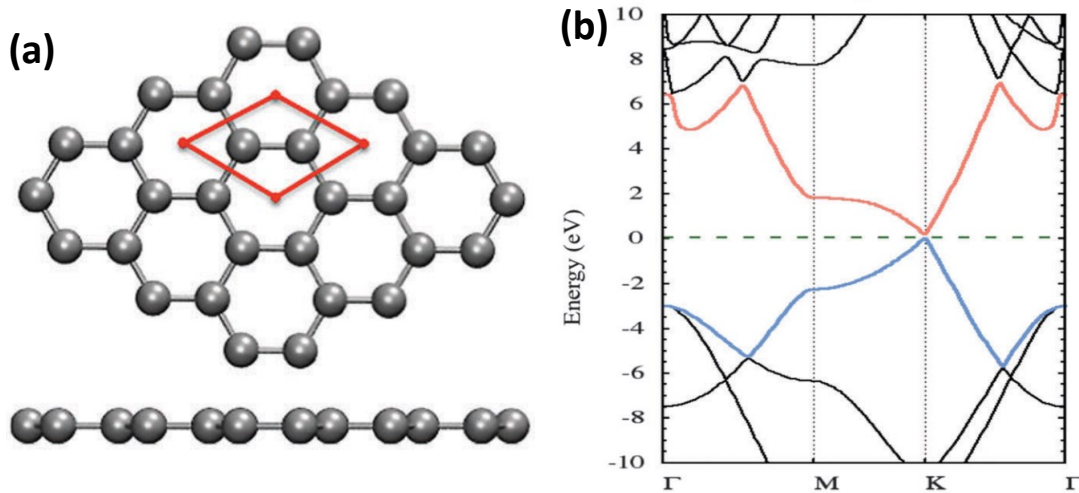
Figure 1.1 (a) Atomic structure of graphene, the unit cell is highlighted. (b) Electronic band structure of graphene, the valence and conduction band are respectively colored in blue and red.

Graphene was first synthesized in measurable quantities in 2004 [4], by means of micromechanical cleavage of graphite, and the main researchers involved, Geim and Noselov, received only six years later a Nobel Prize, due to the importance of their discovery.

This carbon allotrope is characterized by a honeycomb structure, in which every atoms forms planar sp^2 bonds with the three nearest neighbors, at angles of 120°, resulting in the formation of the typical hexagonal rings. The bonds within a graphene layer are about 25% stronger than those of diamond, making it the most stable material known to date and allowing the existence of free-standing sheets.

These strong σ-bonds have lengths of about 1.42 Å, and are the reason for most of graphene's exceptional structural and mechanical properties, such as a specific strength which is more than one hundred times that of steel and extreme elasticity. Due to this, graphene presents an exceptional in-plane thermal conductivity.

The peculiarities in the electronic behavior of graphene are instead due to the fourth, non-hybridized, out-of-plane p_z orbital, which establishes π-bonds, and these in turn create half-filled π bands by conjugation.

In Figure 1.1 is shown the atomic structure as well as the band structure of graphene, and it can be seen that this material presents a semi-metallic character, meaning that while there is no band gap between the valence and the conduction bands, at the Fermi energy the density

of states is zero. This happens at six different positions at the edges of the Brillouin zone, which are called K-points or Dirac-points.

Most importantly, the dispersion relation, i.e. the variation in the band's energy level with respect to the wave vector, is linear at these K-points, creating what are called Dirac cones. Because of the laws of quantum mechanics, this unique dependence leads to the electrons, and holes, at these points being relativistic particles with zero effective mass at rest, named Dirac fermions.

The massless Dirac electrons of graphene at the Fermi energy produce the highest known electron mobility at a finite temperature, and moreover present ballistic transport, that is, there is no electron scattering. The conductivity of pure graphene is nevertheless quite low, because of the zero density of states at the K-points, but can be greatly increased by doping.

Apart from the mechanical and electronic properties, another element of interest for graphene are its optical characteristics: a single layer of graphene, in fact, is capable of absorbing about 2.3% of white light, which is impressive if considering the atomic thickness of this material, also, the addition of a second graphene layer causes the absorbed amount to almost double. It is interesting to note that this value does not depend on specific material properties, but rather on the universal Fine Structure Constant[5].

The second 2D material which will be described is Hexagonal Boron Nitride, or h-BN, a compound which is also colloquially known as "white graphene".

This is because h-BN is an isoelectronic analogue of graphene, sharing the same kind of hexagonal atomic structure, but, in this case, made by alternating boron and nitrogen atoms, each forming three hybridized sp^2 bonds with atoms of the other element, presenting bond length slightly larger than the C-C distance in graphene, at 1.44 Å.

The result is that most of the mechanical properties of graphene can also be found in planar boron nitride, such as great in-plane strength and thermal conductivity, albeit a bit smaller than in the carbon compound. The absence of conjugated p-orbitals, however, along with the ionic character of the B-N bonds, drastically changes the electronic and chemical properties of h-BN.

In fact, while the former is a semi-metal, as mentioned earlier, 2D boron nitride is an insulator, and possesses a large bang gap of about 4.6 eV; this is also the origin of the adjective in "white graphene". The combination of electrical insulation with high thermal conductivity, is extremely interesting for the development of new heat dissipation solutions in electronics, which are impossible with conductive graphene.

H-BN is characterized by a very low light absorption, and can thus be employed in applications where transparency is important. Furthermore, its completely "closed" electronic configuration translates in exceptional thermochemical stability: for example, it is stable and does not oxidize in air even at high temperature, up to 1000° C. This makes it a perfect material for future applications at high temperatures and in chemically-hazardous environments[6].

A single molybdenum disulfide is not, contrary to graphene and hexagonal boron nitride, an atomically thin material, but is instead three atoms thick, with each molybdenum positioned on a plane and bonded to six sulfur atoms, which in turn form two other parallel planes, one above and the other below.

The structure assumed by MoS_2 is illustrated in Figure 1.3. It must be noted that there is another configuration for MoS_2, defined as the T-polytype, since it has an octahedral
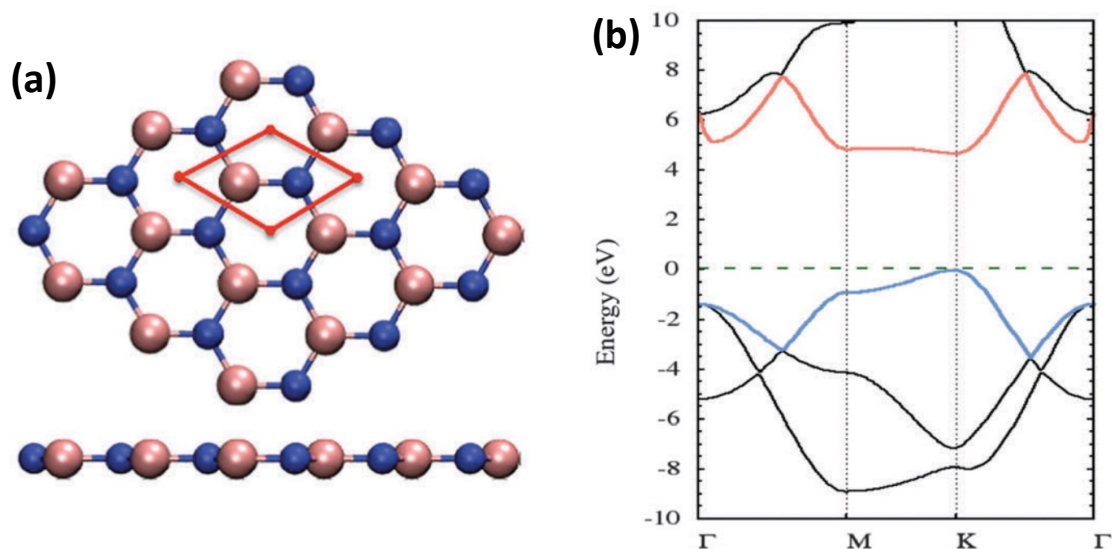
Figure 1.2 (a) Atomic structure of h-BN, the unit cell is highlighted, B atoms are pink, N atoms blue. (b) Electronic band structure of h-BN, the valence and conduction band are respectively colored in blue and red.

(a)

(b)
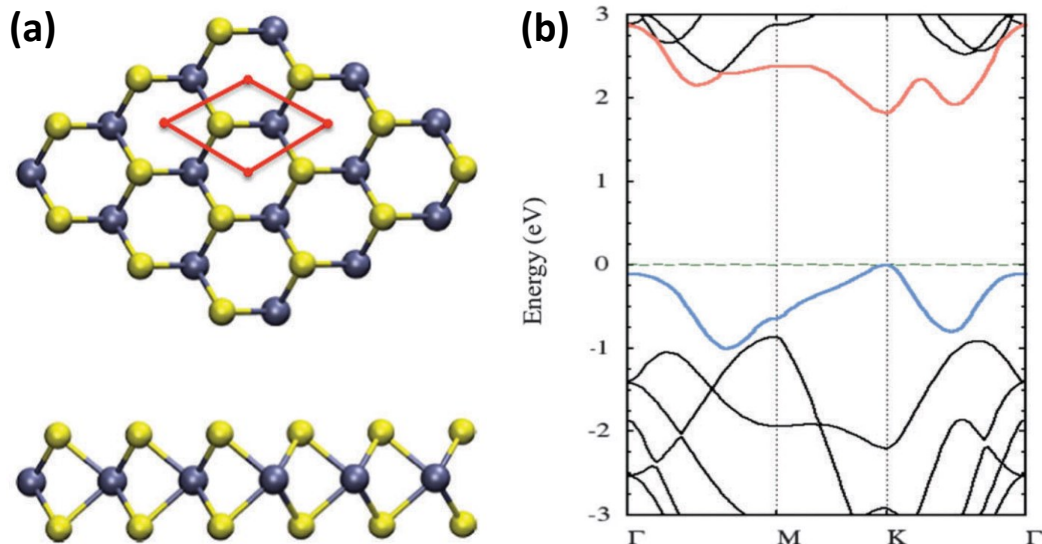
Figure 1.3 (a) Atomic structure of MoS_2, the unit cell is highlighted, S atoms are yellow, Mo atoms blue. (b) Electronic band structure of MoS_2, the valence and conduction band are respectively colored in blue and red.

structure, which is however less thermodynamically stable, and presents different properties than the one considered here, the H-polytype (as in hexagonal).

Molybdenum disulfide is actually one the most important members of a category of planar materials, the Transition Metals Dichalcogenides (TMDs), which have a common stoichiometric formula MX_2, where M is a transition metal, the most important being Mo and W but also Ti, Zr, Hf, Pd, Pt; while the X typically stands for S or Se.

As described earlier, graphene is a semi-metal and h-BN is an insulator, and as such in both cases complex band engineering is needed in order for them be used in logical circuits for electronics. The MoS_2 monolayer is instead a semiconductor, with a direct band gap of about 1.8 eV, which makes it easy to employ in this kind of applications; moreover, other TMDs share this nature, each with a different energy gap; the material utilized can be thus be tailored for the specific system.

The electronical properties of molybdenum disulfide are very dependent on the number of layers present, and just the addition of a second layer is sufficient to change its nature to that of an indirect semiconductor, with a smaller band gap of 1.6 eV, which decreases with the number of layers down to 0.9 eV for the bulk structure.

A large amount of research is being carried out about an extremely interesting possible application of MoS_2, and TMDs in general, valleytronics[7]: a valley is a point of the first Brillouin zone which presents both a maximum of the valence band and a minimum of the conduction band.

Some semiconductors, such as MoS_2, possess multiple valleys in the Brillouin zone, and with the term valleytronics is indicated the storage, reading and manipulation of bits of information, as in electronics, but utilizing in this case valleys and crystal momentum to perform this tasks. An immediate advantage would be an increase in multiplicity of the stored bits, compared to the binary 1/0 system of electronics.

1.2 TWO-DIMENSIONAL OXIDES

The term two-dimensional oxides refers to ultrathin oxide films, with a thickness of a few nanometers at most, which are grown onto a substrate.

Differently from the planar materials presented in the previous section, 2D oxides are not characterized by layered bulk structures, and as such they can't be prepared by exfoliation. This means that in order to obtain them, more complex approaches are required: the most commonly used, and perhaps the most intuitive, is the evaporation of small quantities of the oxide which are then deposited onto a substrate.

While the properties of bulk oxides have been extensively examined and are well known, the interest in ultra-thin oxides is relatively recent, and more research is still needed to fully understand the morphology and the properties of these systems.

Oxides are characterized by interesting and varied properties for technological application, and at this scale it is possible to exploit film thickness as a parameter to better obtain the desired features.
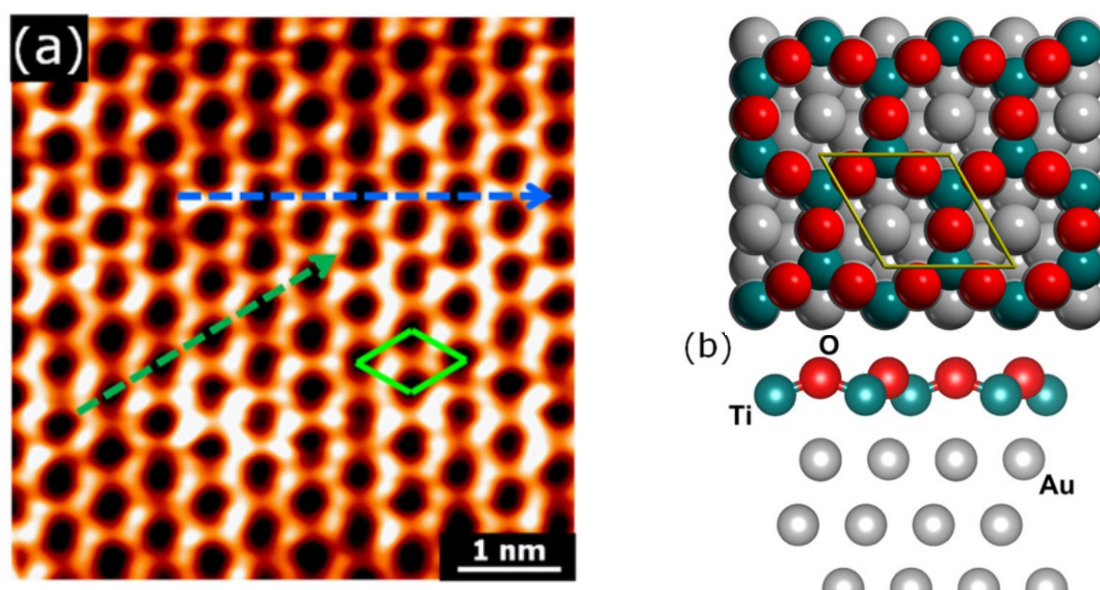
Figure 1.4 Honeycomb phase of TiO$_x$: (a) high-resolution STM image (b) top- and front-view atomic model.

The study of two-dimensional oxides is, however, further complicated by the fact that the characteristics exhibited depend also on the substrate on which they are grown, which can be a metal, a semiconductor or an insulator[8].

Moreover, they sometimes present different, meta-stable phases, which are not found in the bulk material and can be characterized by completely different behavior.

For example, a study which has been recently carried out in this laboratory[9], found that the deposition of TiO_x on a Au(111 substrate resulted in several new phases, different from the rutile and anatase structures of the bulk, one of which is reported in Figure 1.4.

As will be discussed in last sections of this chapter, ultra-thin films of zinc oxide are also characterized by a new, planar conformation: graphene-like zinc oxide.

1.3 PROPERTIES AND APPLICATIONS OF BULK ZnO

Before the next section which describes in depth the state of the art regarding the study and the synthesis of graphene-like ZnO, it may be useful to introduce the characteristics of bulk Zinc Oxide.

ZnO is a II-VI compound, and the difference in electronegativity between zinc and oxygen puts it at the borderline of covalent and ionic semiconductors[10]. It can assume three crystal structures, which are illustrated in Figure 1.5, the most stable and the one observed at standard conditions being the wurtzite phase (w-ZnO).

In this structure, each atom is tetrahedrally coordinated with atoms of the other element, and if a single species is considered, they form a hexagonal close-packed (HCP) sublattice. The crystal is defined by two lattice parameters, which have been experimentally evaluated for w-ZnO and are equal to 3.25 Å for lattice constant a, and 5.20 Å for lattice constant c.

The other two phases are zinc blende and rocksalt: the first one is metastable, and it is possible to stabilize it only by growing ZnO heteroepitaxially upon a substrate presenting a cubic structure, such as ZnS; a transition from wurtzite to rocksalt configuration is instead observed when high hydrostatic pressure, in the order of 10 GPa, is applied to the crystal, which also causes a large decrease in volume of 17%.
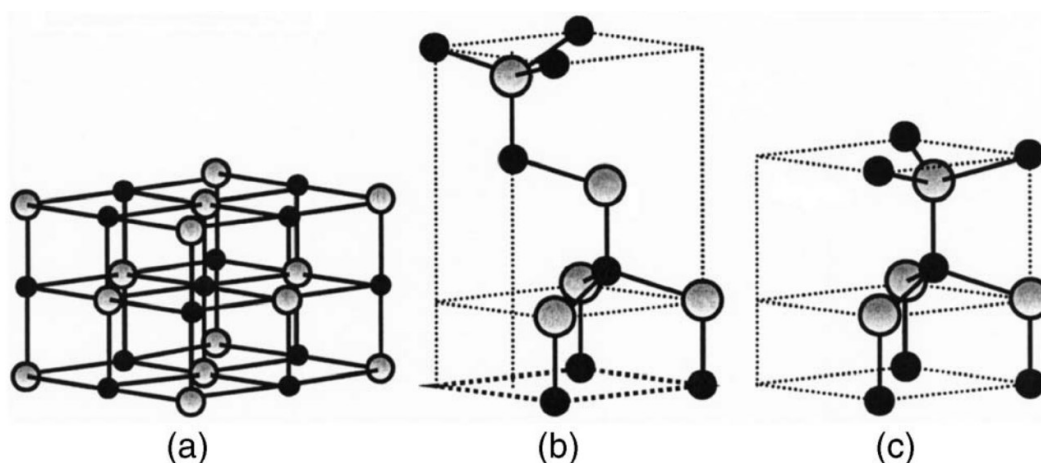
Figure 1.5 Representation of ZnO crystal structures: (a) cubic rocksalt, (b) cubic zinc blende and (c) hexagonal wurtzite. The gray and black spheres denote Zn and O atoms, respectively.

A large part of the recent interest in ZnO is due to its electronic and optical properties. Zinc oxide is, in fact, a semiconductor characterized by a wide direct band gap measured at 3.37 eV, but most importantly it presents a very large exciton bonding energy, 60 meV.

These two factors, along with the ease of growth of high quality crystal when compared to other similar materials, make ZnO an ideal choice for light emission in the near ultra-violet, even better than the most commonly utilized GaN.

The biggest obstacle to its utilization in this field is that ZnO tends to be naturally n-doped, and there are difficulties in the reliable production of p-doped counterparts, which are needed for the development of such devices, because of low solubility of the dopant atoms.

Zinc oxide can be defined as a multifunctional material, since it presents numerous attractive properties which can be exploited in very different technologies. For example, ZnO is piezoelectric (in fact, it possesses the largest measured electro-mechanical coupling) and pyroelectric, and as such it is used in sensors, converters and energy generation.

Moreover, zinc oxide is biodegradable and biocompatible, which means that it can considered in biomedical applications. Finally its hardness and rigidity find use in the ceramic industry.

The wurtzite structure is not characterized by inversion symmetry, and this means that if a crystal is cut perpendicular to the c axis, the two resulting surfaces will be different and will present only zinc or only oxygen atoms.

These surfaces are referred to as (0001)-Zn and $(000\bar{1})$-O, respectively, and because of the difference in electronegativity between the two types of atoms, they are polar. Normally, the presence of a dipole moment perpendicular to the surface should cause the latter to be unstable, but numerous studies have verified that the (0001)-Zn and $(000\bar{1})$-O surfaces of ZnO are stable without the need for reconstruction[11].

The cancellation of the dipole moment is achieved by a reduction of about ¼ of the surface charge, and so far a few theories have been proposed regarding the stabilization mechanism[12], but no conclusive evidence of which is the real one has been found.
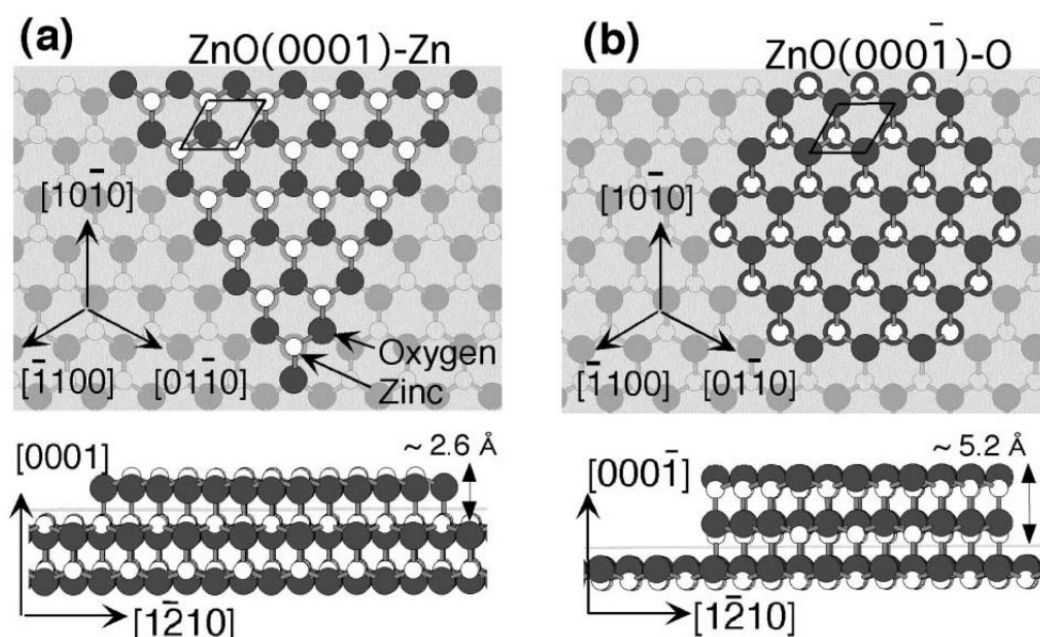
Figure 1.6 Top and side views of atomic models for the bulk-terminated ZnO surfaces: (a) (0001)-Zn and (b) $(000\bar{1})$-O.

Nevertheless, these two surfaces generate great scientific and technological interest, since they present different physical and chemical properties, and have been discovered to be important in the catalysis processes which involve ZnO.

In Figure 1.6 is shown the structure of the zinc oxide surfaces described, along with the typical morphology which they assume when observed at the nanoscale. In fact, (0001)-Zn surfaces tend to be characterized by triangular shaped islands and to present mono-layer steps, whereas $(000\bar{1})$-O terraces appear to be mostly hexagonal and two-layers high.

In addition to the planar zinc oxide discussed in depth in the next section, ZnO creates one of the most abundant assortments of nanostructures among all known material [13], and numerous kinds of 1D structures (needles, helixes, springs, wires, etc) and 3D structures (flowers, dandelions, snowflakes, etc) have been synthesized and studied.

1.4 TWO-DIMENSIONAL ZINC OXIDE

1.4.1 Predicted properties

The first to hypothesize the existence of a "graphene-like" phase of zinc oxide were Claeyssens et al.[14,15] in 2005, who were studying the deposition of thin ZnO films as templates for aligned growth on ZnO nanorod.

They discovered that, when considering films terminating with the polar (0001) and $(000\bar{1})$ surfaces and characterized by a number of layers inferior to 18, or less than 10 if terminating with the non-polar $(10\bar{1}0)$ and $(11\bar{2}0)$ surfaces, ab initio DFT (density functional theory) calculations resulted in a flattened structure.

In this configuration, each Zinc atom is bonded with three Oxygen atoms instead of four as in bulk, and vice versa, in a co-planar disposition which results in the formation of layers composed by flat Zn_3O_3 hexagonal rings, the same kind of structure displayed by graphene and h-BN, while in the wurtzite crystalline structure the same rings can be found in non-planar "boat" and "chair" conformations. The transition between the two can be more easily understood by looking at Figure 1.7.
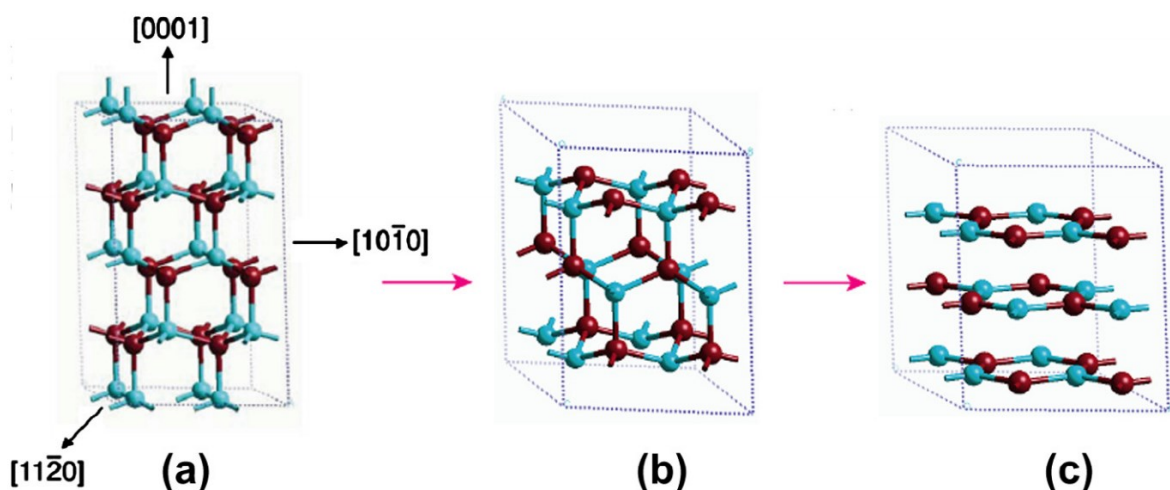
Figure 1.7 (a) Wurtzite structure of bulk ZnO. Zn atoms are depicted in light blue, O in red[14]. (b)-(c): Model for the relaxation of the polar wurtzite structure of a ZnO(0001) film into the graphitic structure[15].

The structural transformation was thought to be driven by surface charge transfer, and since the three sp^2 bonds are stronger than the four sp^3, the derived bond length presents a 3% contraction. Also, the new (0001) surface was found to be semi-conducting, in contrast with the metallic character of the not relaxed wurtzite monolayer.

Further analysis theorized the same kind of behavior for a large number of other compounds which also present a bulk wurtzite structure, such as AlN, BeO, GaN and ZnS, but while various studies (presented in the next section) have demonstrated the synthesis of g-ZnO, until today the graphene-like phase of these materials has not been observed.

These findings led to great interest in the scientific community[16], and a great number of ab initio calculations have since then been carried out to predict what properties this newly announced phase would have, and to find out in which fields its application would be possible.

An in-depth study of the atomic, electronic and magnetic properties of the 2D honeycomb ZnO structure can be found in the work of Topsakal et al.[17]. The equilibrium structure for a ZnO monolayer was confirmed to be planar and characterized by a hexagonal lattice where the two identical Bravais vectors and the ZnO bond lengths were predicted to be $a_1=a_2=3.283$ Å and d=1.895 Å, respectively.

This value is lower than the bond length present in the bulk zinc oxide structure, equal to 2.001 Å, because the bonds present in this configuration are stronger than the tetrahedrally coordinated bonds of wurtzite, as mentioned earlier. Nevertheless, the lattice of g-ZnO is noticeably bigger than that of graphene or h-BN, since zinc is larger than the atoms present in these compounds. Simulations were performed and, while not conclusive, strongly indicated the probable stability of the system, since they were unable to destroy the honeycomb structure.

The derived phonon dispersion curves are presented in Figure 1.8a, with another research[18] having similar results and discovering that at Γ point, the out-of-plane acoustic mode has an asymptotic behavior $\omega(q)=Bq^2$ ($B=1.385*10^{-7}$ m^2/s), while the two in-plane acoustic modes sound velocities are equal to $v_t=2.801$ km/s and $v_r=8.095$ km/s, respectively, which are much smaller than the corresponding velocities of graphene, 15 km/s and 24 km/s respectively. The optical modes have frequencies of 250 cm^{-1}, 566 cm^{-1}, and 631 cm^{-1}.
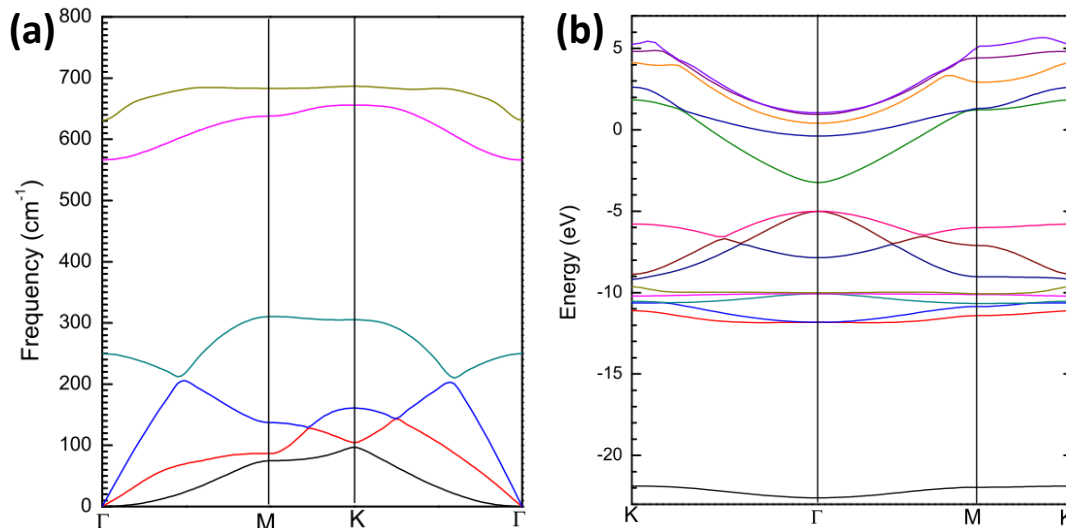
Figure 1.8 (a) Phonon dispersion curves (b) Energy dispersion curves for 9 valence and 5 conduction bands plotted along high symmetry directions in the Brillouin zone.

Figure 1.8b shows instead the electronic structure of graphene-like ZnO, which is predicted to be a wide direct-gap semiconductor; DFT modelling tends to underestimate the band gap, but the value obtained is larger than that of bulk zinc oxide computed with the same approach, and after applying GW correction results in a 3.57 eV gap.

The evolution of some of the characteristics of g-ZnO with an increase in the number of layers up to five was also examined[19], and it gave rise to a progressive reduction in the band gap energy. More information regarding the atomic structure as well as the binding energy is reported in Figure 1.9, it must be noted that with the addition of a second layer and above, the optimized configuration is no longer perfectly planar, but presents a small buckling.

Regarding the predicted mechanical properties, studies[20] suggested that the ZnO monolayer is a much softer material in comparison with graphene or hexagonal boron nitride, characterized by a low in plane stiffness (47.8 N/m) and a high Poisson's ratio of 0.667.

It also exhibits non-linear elastic deformations, with estimated ultimate strains equal to 0.17 along the armchair direction, 0.24 along the zig-zag direction and 0.20 for a biaxial strain. The ultimate strengths at rupture in these three situations resulted being respectively 36%, 33%, and 33% of the values found in the case of h-BN.

N	a	R_{in}	R_{out}	ΔZ	E_b
1	3.284	1.896	–	0	−7.032
2	3.353	1.937	2.360	0.067	−7.191
3	3.377	1.950	2.361	0.049	−7.239
4	3.392	1.959	2.351	0.053	−7.268
5	3.402	1.965	2.344	0.053	−7.285
bulk	3.445	1.989	2.305	0	−7.362

Figure 1.9 The structural parameters and binding energies of ZnO nanofilms. The number of layers N, the optimized lattice constant a (Å), the average bond length within layers R_{in} (Å) and between layers R_{out} (Å), the spacing between Zn and O planes in surface ΔZ (Å) and the binding energy E_b (eV/ZnO) are given.

An interesting aspect examined is the fact that Zn vacancies in the structure generated local magnetic moments, whereas other kinds of lattice defects, for example Oxygen vacancies , Zn+O double vacancies or antisite defects (meaning that one zinc atom and one oxygen atom exchange positions) did not cause any change in the magnetic properties of this material.

Different studies have focused on the effect of doping: the addition of Co was found to promote ferromagnetic coupling [21] , while a transition from non-magnetic to anti-ferromagnetic and finally to ferromagnetic was achieved by doping the oxygen sublattice with C or B atoms[22], which also resulted in transformation of honeycomb ZnO from semiconductor to half metal. The addition of N, instead, created an anti-ferromagnetic p-type semiconductor.

Moreover, computations about the impact of hydrogenation[23] and fluorination[24] have been carried out, which again consisted in variations in the metallicity and magnetic character. The fact that the electronic and magnetic properties of graphitic zinc oxide can be tuned by changing the doping type or the number of layers is of great stimulus in the study of potential future applications in nanoelectronics and spintronics.

Possible use in mechatronics or straintronics was also hypothesized since, differently from what happens in the case of graphene, computations [25] suggested a strong, non-linear dependence of the band gap of a ZnO monolayer on the applied in-plane homogeneous strain.

This coincided with an almost linear decrease in the Fermi velocities of charge carriers with increasing strain. The application of this kind of biaxial tensile strain is also thought[26] to result

in the transition of g-ZnO from a direct gap to an indirect gap semiconductor when the strain value exceeds 8%.

Finally, several recent works[27,28] were dedicated to graphene/graphene-like ZnO (G/g-ZnO) nanocomposites: one of the main problems in the development of graphene based technology is the difficulty in finding a suitable substrate that does not interact with it in a way that modifies its exceptional intrinsic properties, which were described at the beginning of this chapter.

The result of the simulations was that in the G/g-ZnO composite, whose optimized structure is shown in Figure 1.10, the interactions established between the two planar materials are only weak van der Waals forces, there are no chemical interactions and also the respective electronic states are kept separate.

This would mean that in this structure the graphene continues for example to be characterized by a linear dispersion relationship, and the related extremely high carrier mobility is preserved, making g-ZnO an ideal substrate for graphene based devices.
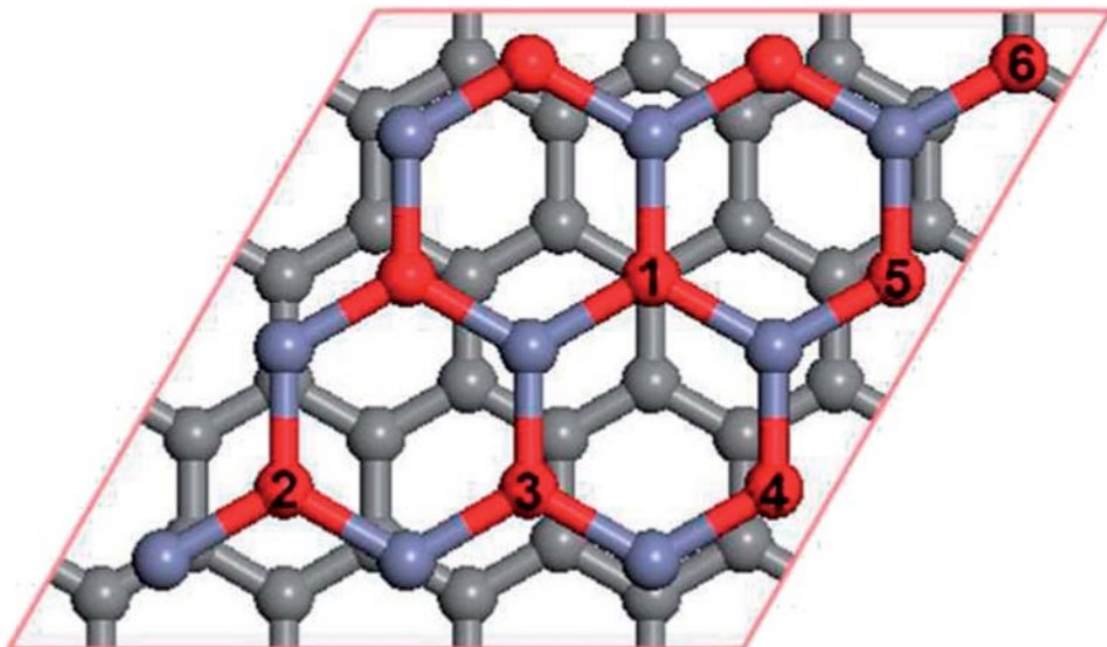
Figure 1.10 Optimized structure of the GZO nanocomposite. The numbers represent six possible positions for an oxygen vacancy. The gray, red, and blue balls denote carbon, oxygen, and zinc atoms, respectively.

1.4.2 Experimental studies

In this section a review will be presented of the articles which can be found in scientific literature regarding the deposition of ultra-thin films of zinc oxide on metallic substrates, and especially those focusing on the synthesis of graphene-like ZnO.

When considering depositions realized by Electron Beam Physical Vapor Deposition or Pulsed Laser Deposition, the techniques employed in the course of this thesis, and which will be discussed in detail in the next chapter, the experimental conditions will be also described, so as to ease the comparison between the results obtained.

Almost all of the images presented in these articles were taken by means of Scanning Tunneling Microscopy (STM), and its working principles will again be illustrated later in this thesis, in Section 2.3.

A term which will often be found in this review is coverage: it is a measure of the quantity of material deposited on the substrate, expressed in monolayers (ML), i.e. the number of uniform atomic layers this quantity of deposit would create on the surface, which can also be lower than one. Coverage can be calculated through different techniques, such as X-ray diffraction (XRD).

The first work showing experimental evidence of the existence of this two-dimensional configuration of ZnO was published in 2007 by Tusche et al.[29].

Their substrate of choice was the (111) surface of a mechanically polished Silver single crystal, which was cleaned by in situ Ar^+ sputtering cycles: this is the most common method of surface preparation for this kind of experiments, and will be used in most other articles described as well as in the course of this thesis.

ZnO was grown by PLD utilizing a stoichiometric zinc oxide target, operating at a temperature of 300K and at a rate of 0.10 ML/s, with a background oxygen pressure of $5*10^{-7}$ mbar. The samples were then annealed up to 680K, after which the presence of stoichiometric zinc oxide films on the Ag(111) surface was verified thanks to x-ray photoelectron spectroscopy. If the annealing temperatures exceeded 750K, the team discovered that problems arose, due to intermixing and surface roughening.
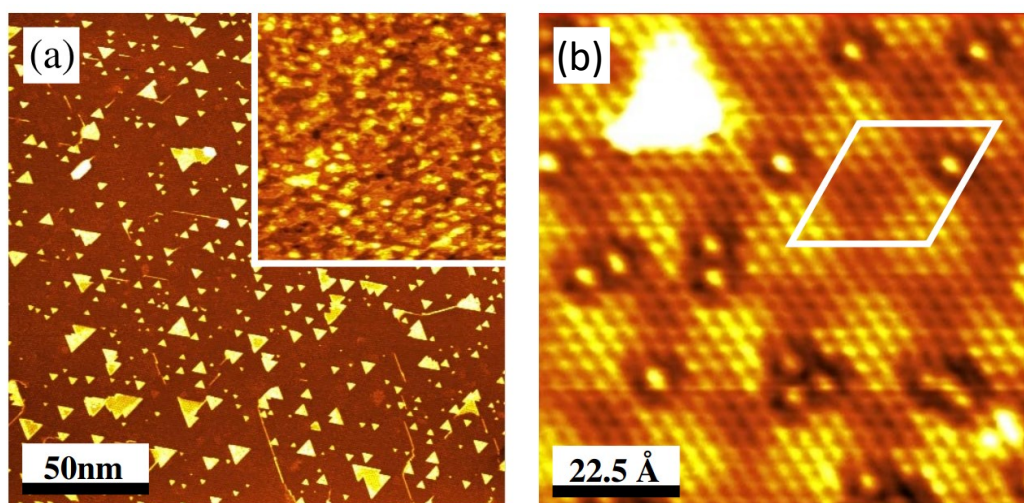
Figure 1.11 (a) (200x200) nm STM image of 2.2 ML ZnO on Ag(111). The inset shows a higher coverage deposition at the same scale. (b) High resolution (9x9) nm STM image of the 2.2 ML film.

The STM measurements were carried out in UHV (ultra-high vacuum), at pressures in the order of $1*10^{-10}$ mbar, and the samples examined showed coverage in the interval from 2.2 to 4.5 monolayers. Figure 1.11a shows a STM image of a 2.2 ML ZnO film, characterized by an atomically flat zinc oxide double-layer, above which small triangular islands formed by a single layer (the third) can be seen, with the edges oriented along high symmetry directions.

Again in Figure 1.11a, the indent shows an image at the same scale, but which is noticeably rougher, relative to a higher coverage of 3.2 ML. According to Tusche, in fact, if the quantity deposited goes too much above 2 ML, the first double-layer is no longer complete, and the morphology changes to isolated, taller structures, interpreted as a progressive transition to the bulk wurtzite configuration, much earlier than what first principle studies indicated.

Images taken at a smaller scale, such as Figure 1.11b, show a distinct moiré pattern: this is a very important characteristic, which was observed in most experimental analyses, as will be shown in this review, and was the main method utilized in this thesis to identify the successful synthesis of graphene-like ZnO.

It is generally produced by the superposition of two lattices with different constants, which in this case are the Ag(111) surface and the zinc oxide double-layers: both present hexagonal symmetry, and so the resulting moiré is also characterized by a hexagonal coincidence lattice.

The Zn and O atoms find themselves in different positions with respect to the Ag atoms underneath, and create a surface corrugation, thanks to which it is possible to deduce the ratio between the respective unit cells, found by Tusche to be 7 ZnO to 8 Ag(111).

A particularly important study is that of Deng et al.[30], since it used the same substrate that has been the focus of this thesis, the Au(111) surface. In this case the ultra-thin films were obtained by reactive deposition of e-beam evaporated pure zinc in an atmosphere of NO_2 at a pressure of $3*10^{-8}$ and at room temperature.

The use of this strong oxidant was reportedly made necessary because the team discovered that even values of $2*10^{-6}$ mbar of oxygen were unable to fully oxidize zinc.

The deposited material was proved to be made of stoichiometric ZnO by using XPS and STM imaging presented two types of nanostructures, both displaying a moiré pattern which has been calculated by DFT as originating from a ZnO(0001)-(7x7)/Au(111)-(8x8) supercell, having periodicity of ~23 Å which translates in an in-place lattice constant of ~3.3 Å for ZnO.
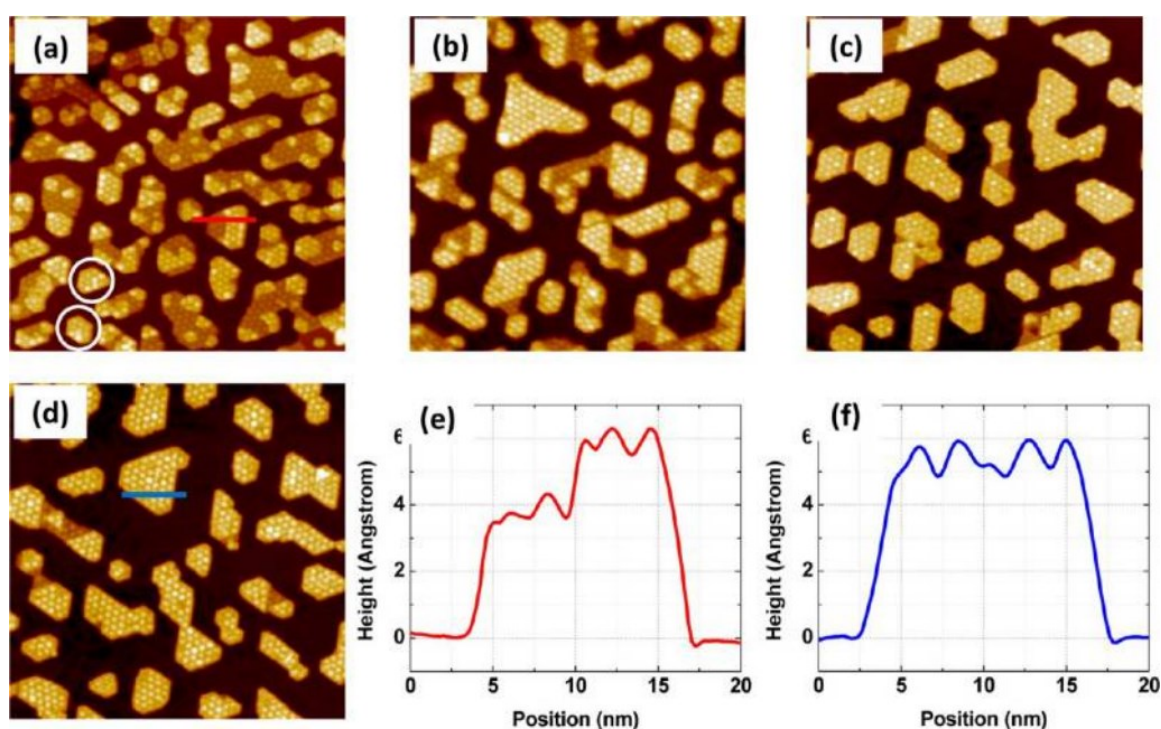
Figure 1.12 Room temperature STM images (100 × 100) nm of 0.9 ML ZnO on Au(111) using the reactive deposition method followed by annealing at 550 K for (a) 5; (b) 30; (c) 60; and (d) 120 min. (e,f) Line profiles specified in panels a and d, respectively.

The two types of nanostructures were however characterized by different heights, respectively measured to be ~3.5 Å (defined low-ZnO) and ~5.5 Å (high-ZnO), and so it was hypothesized that they represented the monolayer and the bilayer configuration of graphene-like zinc oxide.

The images illustrated in Figure 1.12 denote the focal point of the analysis, which was the evaluation of the morphological evolution with respect to the duration of the post-annealing process, carried out in vacuum while the temperature was kept at 550K.

As it is shown, at shorter annealing durations a good portion of the oxide was present in the low-ZnO state, but the ratio lowered as the time at high temperature increased, until after two hours of annealing almost all the nanostructures consisted of high-ZnO. The explanation proposed for this phenomenon was that in those conditions the interaction between layers dominated that between oxide and metallic surface, and thus the bilayer was energetically favored.
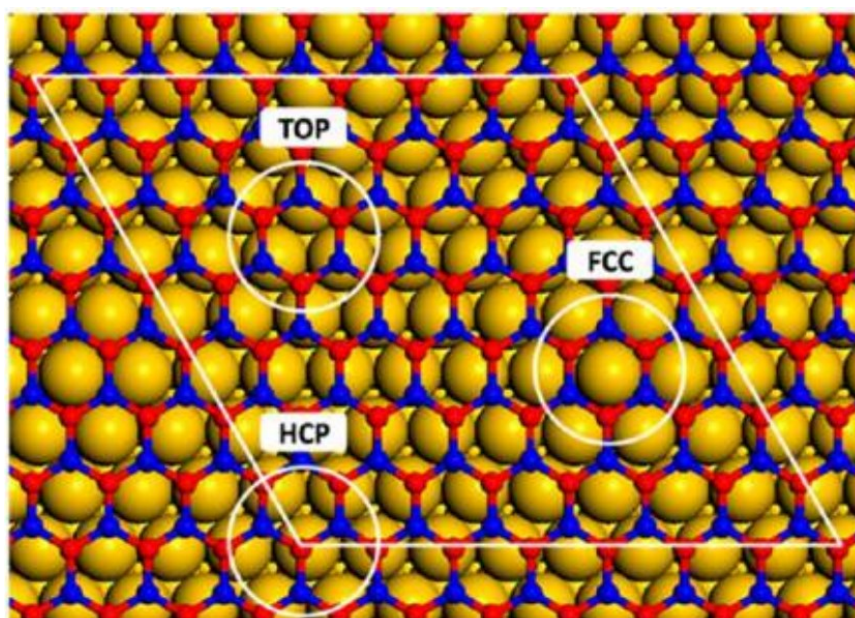
Figure 1.13 (a) Top view of the single-layer ZnO(0001) on Au(111). The Moiré pattern with periodicity of ZnO(0001)-(7×7)/Au(111)-(8×8) and corresponding FCC, HCP, and TOP domains defined by the sites of Zn on Au(111) are indicated by the white parallelogram and circles. The large yellow ball, small red ball, and blue ball represent Au, O, and Zn, respectively.[30]

An interesting model of the configuration of the g-ZnO monolayer upon the Au(111) surface is reported in Figure 1.13, which allows to better understand what is actually observed in the STM images.

Another analysis on the behavior of zinc oxide on Au(111)[31], focused on the transition from the graphene-like phase to the bulk wurtzite structure, which was found to begin after the fourth monolayer. It was also suggested that the moiré contrast did not only depend on the variation in the Zn/O atoms position with respect to gold, but was also enhanced by adsorbates which occupy only distinct sites of the moiré cell.

The fact that the moiré pattern observed in STM measurements is effectively due to an atomic corrugation of the surface, has been however questioned by a research presented by Shiotari et al.[32]. The team analyzed ZnO ultra-thin films made by reactive deposition of zinc in oxygen ($1*10^{-5}$ mbar) on the Ag(111) surface, simultaneously collecting images of the sample by using both a STM system as well as a nc-AFM, non-contact Atomic Force Microscope.

The results are shown in Figure 1.14, where it can be seen that the moiré pattern observed in the STM image is completely absent in the one given by the AFM, which instead shows atomically flat surfaces. This would indicate that the pattern is due, at least for the most part, not to a varying atomic disposition but to a corrugation in the LDOS (local density of states).
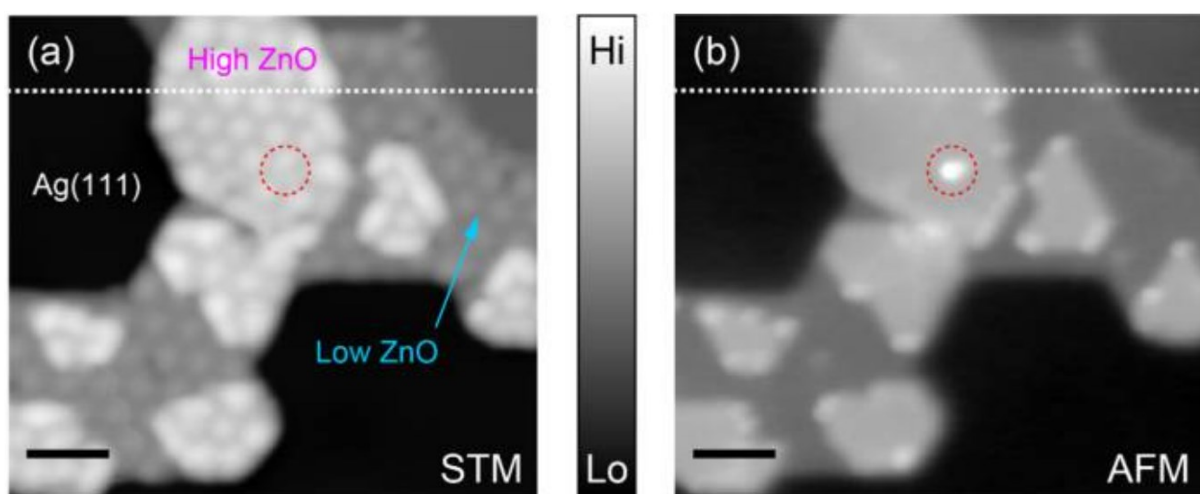
Figure 1.14 (a, b) STM image and nc-AFM image obtained at the same area (scale bar = 5nm) at 5 K. The dotted circle represents a defect on the high-ZnO island.
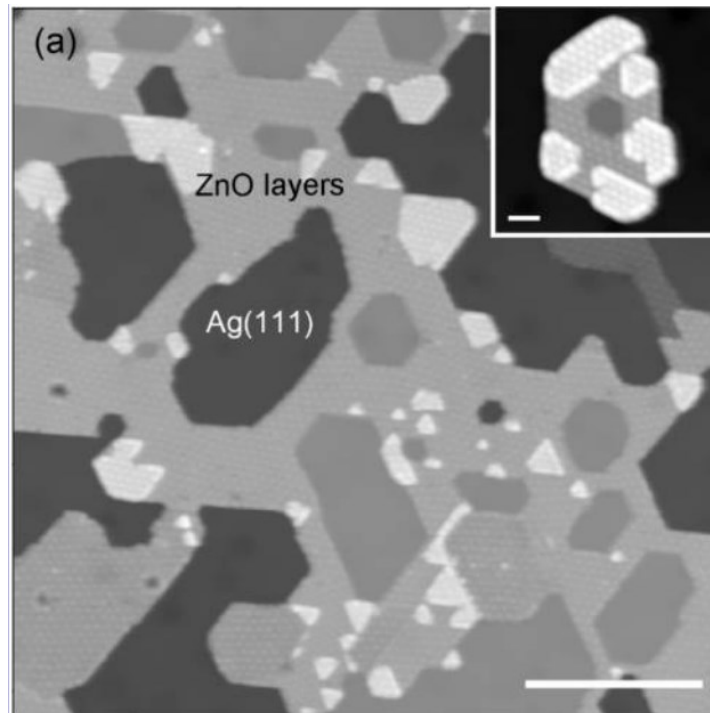
Figure 1.15 STM overview image of ultrathin ZnO layers on Ag(111) (bar = 50 nm) at 5 K, revealing both bare Ag(111) areas and ZnO layers. The inset shows a STM image of a small ZnO island on the Ag(111) terrace (scale bar = 5 nm).

The electronic nature of the moiré pattern was also supported by the detected strong dependence of the corrugation amplitude with respect to the applied voltage.

The surface of silver was subjected to a reconstruction phenomenon during the deposition treatment, with the appearance of small Ag patches, one atomic step high, which were not present on the cleaned surface, as shown in Figure 1.15. Moreover, an annealing temperature of at least 600K was found to be critical in order to achieve ordered deposited structures.

Lastly, the apparent height of the low-ZnO and high-ZnO mentioned in Figure 1.14 was found to be respectively of about four and six angstrom, and so the study suggested that ZnO layers on Ag(111) grow predominantly as bi- and tri-layers under the conditions used.

An interesting experimental analysis is that of Weirum et al.[33,34], which describes the deposition of ultra-thin films of ZnO on a Pd(111) substrate.

In this case the technique used is the deposition of metallic zinc at room temperature by means of a Knudsen cell, which was then followed by a period of post-oxidation in the case

of sub-monolayer coverages, whereas for higher quantities of zinc the use of reactive evaporation was chosen.

In both cases, the sample was then annealed in oxygen at 550K to achieve better structural order, temperature chosen because by applying thermal desorption spectroscopy they found the onset of ZnO loss to be at 570-580K.

In the sub-monolayer range and with very low oxygen pressures, two competing structures were found, as can be seen in Figure 1.16: the first one being a honeycomb-like (4x4) phase, which after further analysis was concluded to have $Zn_6(OH)_5$ stoichiometry, and the second a hexagonal layer with formula $Zn_{25}O_{24}$, containing a (6x6) array of oxygen vacancies, due to O-poor conditions. This latter structure also presents a moiré pattern, this time with a lattice constant 6 times that of Pd and 5 that of ZnO.

By repeating the analysis at progressively higher pressures of oxygen, up to $5*10^{-6}$ mbar, it was observed that both structures tend to transform into a planar hexagonal phase characterized by two layers presenting Zn_6O_6 composition.

Further studies on the Pt(111) surface[35,36,37], in which ZnO was deposited by low-pressure reactive deposition by thermal evaporation, followed by higher pressure post-oxidation, have seen the formation of the two kind of isles earlier described, but in this case the measured height was respectively ~2 Å for the monolayer and ~4 Å for the bilayer.
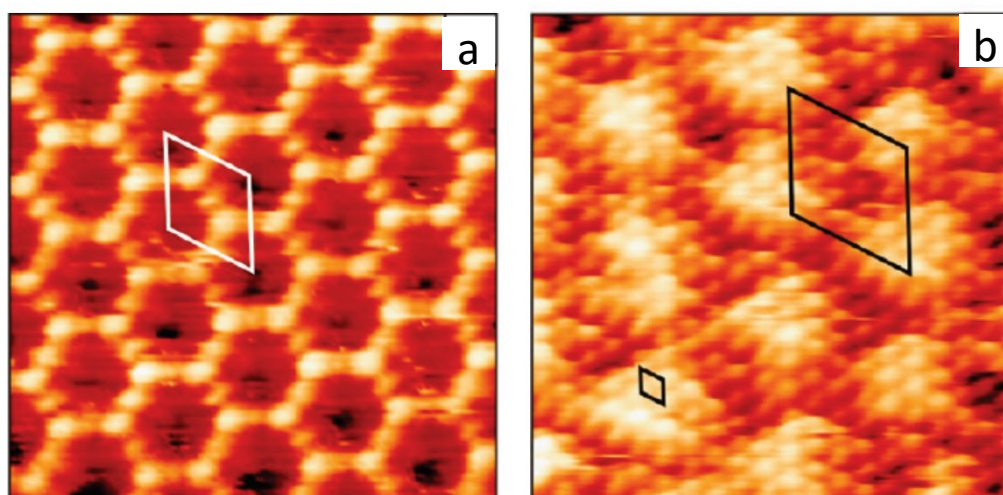
Figure 1.16 (a) High-re STM image of the (4×4) phase (6.5×6.5) nm (b) High-res STM image of the (6×6) phase (5.0×5.0) nm.

The evolution of the (4x4) and (6x6) planar ZnO phases, first described by Weirum on a Pd(111) substrate, was examined, discovering that the transition between them is completely reversible and long term exposition to UHV results in predominant (4x4) structure formation, which after heating and exposing to oxygen re-transforms into mainly (6x6) phase.

The fact that this phases were observed on Pt(111) and Pd(111), was tentatively attributed to the much higher affinity of these surfaces towards hydrogen when compared to Ag(111) and Au(111), on which they were not seen. In this case, the hydrogen which yields to the formation of hydroxyls would be given by the metal surface rather than the gas phase.

Finally, a recent work[38] studied the deposition of ultra-thin ZnO in the Ag(111) surface as well as the same surface of copper, obtained by reactive deposition of thermally evaporated zinc in an oxygen pressure. Two sample images are reported in Figure 1.17.

It was however found that on the Cu(111) surface, after annealing even at low temperatures (450K) there was a progressive loss of zinc detected by Auger Electron Spectroscopy (AES), which was not attributed to sublimation phenomena but to migration of Zno into the bulk copper and subsequent formation of a CuO_x film; this would show that Cu(111) is not a suitable substrate for g-ZnO given these experimental conditions.
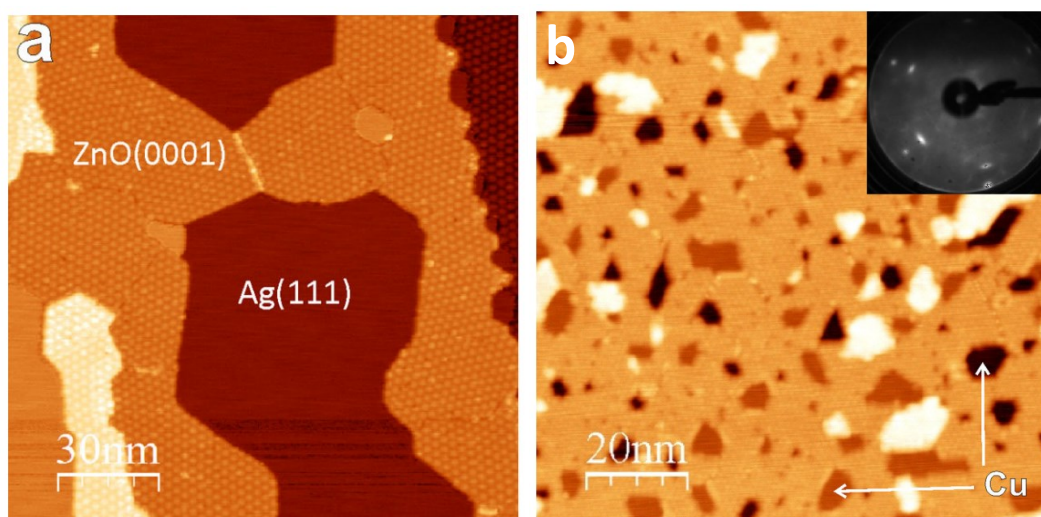
Figure 1.17 STM images of a) ZnO(0001) film on Ag(111) b) 2 ML ZnO(0001) film on Cu(111). The inset shows a corresponding LEED pattern at 60 eV.

1.5 THESIS OBJECTIVES

In light of the considerations which have been pointed out in the course of this chapter, it is possible to more clearly illustrate the objectives of the experimental analysis presented in this thesis.

The main objective was the study of the synthesis and of the morphological and structural properties of two-dimensional zinc oxide on Au(111).

This was done by using two different approaches: electron beam evaporation of metallic zinc which was then oxidized, and pulsed laser deposition from a stoichiometric ZnO target.

The effect of the different parameters, which could be controlled during the deposition process, on the morphology of the obtained g-ZnO nanostructures was also examined. This included the quantity of material deposited and especially the presence of oxygen both during the deposition and during the subsequent thermal treatment.

The characterization of g-ZnO nanostructures and ultra-thin films was performed with the help of a Scanning Tunneling Microscope, since this instrument is capable of very high resolution, required for accurate morphological analysis.

2 SYNTHESIS AND CHARACTERIZATION TECHNIQUES

In this chapter will be described the main deposition and characterization methods employed in the course of this thesis. First the working principles and the features of Electron Beam Physical Vapor Deposition will be presented (Section 2.1), followed by a similar portrayal of Pulsed Laser Deposition (Section 2.2).

In Section 2.3, the Scanning Tunneling Microscope will be introduced, with an in depth description of the theoretical models for electron tunneling (Section 2.3.2), after which an overview on the working principles of this instrument can also be found (Section 2.3.3).

Finally, the experimental apparatus utilized in this thesis work will be briefly illustrated in Section 2.4.

2.1 ELECTRON BEAM PHYSICAL VAPOR DEPOSITION

Electron Beam Physical Vapor Deposition (EB-PVD) is a vacuum evaporation technique commonly employed in Surface Engineering in which, as the name implies, the heat necessary for the evaporation of the material to be deposited (the evaporant) is supplied by a flux of electrons.

It is an evolution of the Thermal Evaporation technique, which is characterized by almost the same structure, but in that case the heat is transferred from the heating element to the source simply by conduction and radiation.

The e-beam is generated by applying a strong potential to a filament, usually made of tungsten, which emits electrons having high energy by taking advantage of the Thermionic Effect or of the Field Emission Effect.
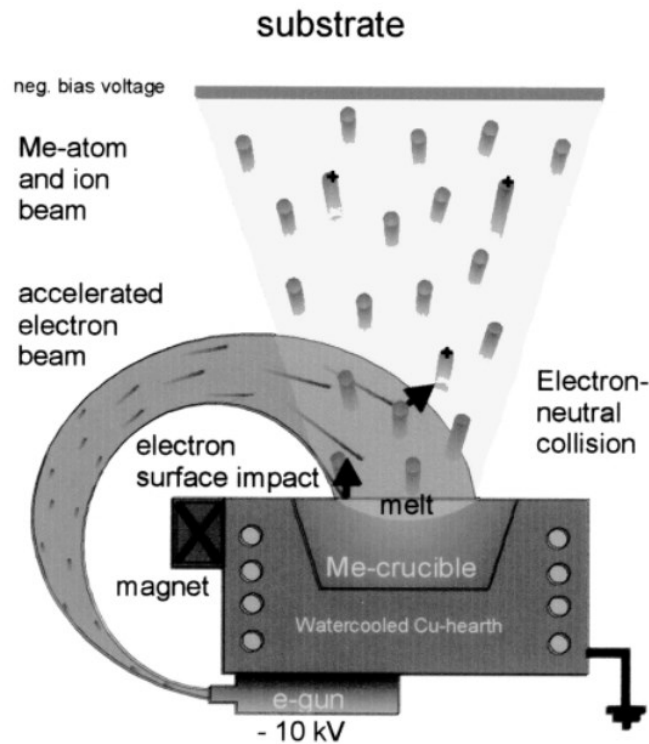
Figure 2.1 Electron Beam Physical Vapor Deposition schematic[39]

When the beam is made to hit the source, this kinetic energy transforms mostly into heat and if the temperature reached is high enough, causes local sublimation.

The structure of a typical EB-PVD system is presented in figure 2.1, but it must be noted that the whole structure has to be placed in a UHV chamber. Apart from the effects on the film's quality, the vacuum condition is needed to allow the electrons to travel from the emitter to the source, without being slowed, deviated or absorbed by the atoms of the gas, and then for the evaporated material to reach the surface of the substrate, by having a mean free path bigger than the distance between the elements.

The evaporation source can be in the form of an ingot or of a rod, and is in most occasions water-cooled: this ensures that the only portion of the system to reach high temperatures is the spot which the electrons hit, while the rest is kept at room temperature or lower, which translates in a lower vacuum contamination and purer deposited films, in fact, e-beam PVD has been for years the most popular deposition technique when high purity is a requirement.[40]

Among the other advantages[41] of this deposition method is the ability to greatly control the deposition rate, from as low as under one nanometer per minute to more than 100 μm/min, as well as to control the composition and the microstructure of the film.

The basic equation for evaporation flux, representing the number of molecules per unit area per second, is given by:

$$\Phi_e = \frac{\alpha_e N_A (P_v - P_h)}{\sqrt{2\pi M R T}}$$

Where α is the coefficient of evaporation ($0 < \alpha_e < 1$), M the molar mass of the evaporant, R the gas constant , and T the temperature; while P_v and P_h are respectively the vapor pressure and the ambient pressure.

When considering deposition experiments, it is however more important to calculate the mass deposition rate per unit area of evaporant surface, which is given by the semi-empirical Langmuir-Knudsen relation

$$R_m = C_m \left(\frac{M}{T}\right)^{\frac{1}{2}} cos\theta cos\varphi \frac{1}{r^2} (P_v - P_h)$$
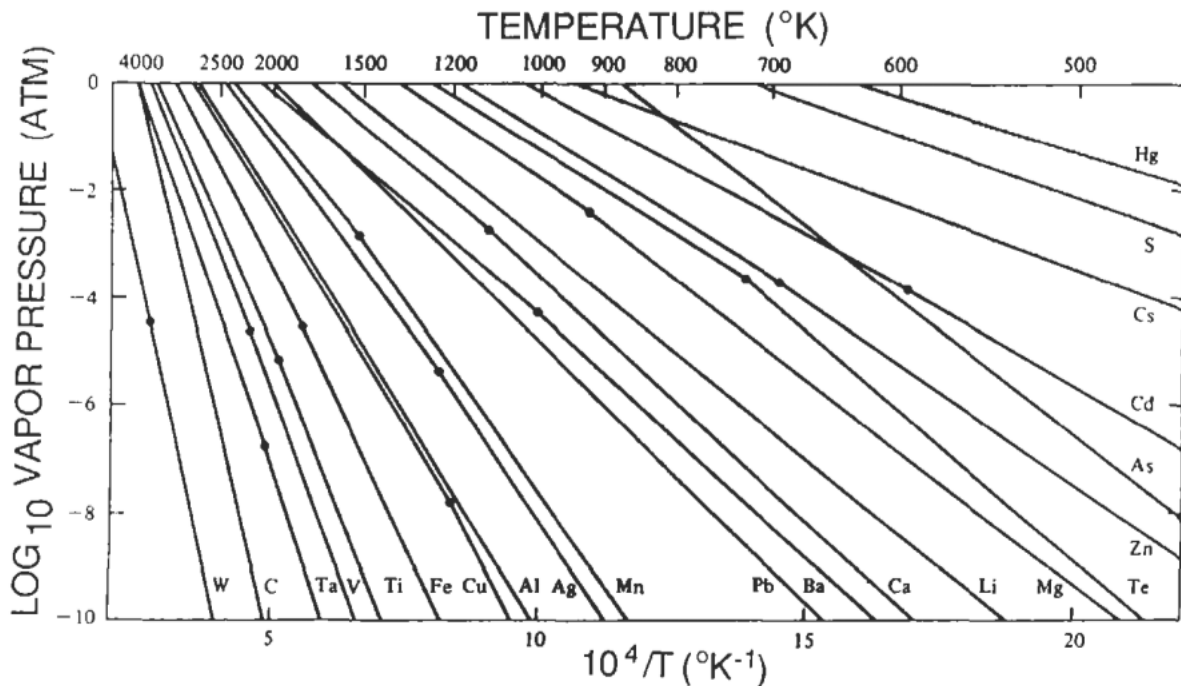
Figure 2.2 Vapor pressures of selected elements. Dots correspond to melting points.

In which r is the source-substrate distance in centimeters, ϑ and φ are the angles made by a line between these two elements and the normals respectively to the source and to the substrate surface, and finally C_m is a constant, equal to $1.85 \cdot 10^{-2}$ if the pressures are expressed in torr.

It is obvious that the knowledge of the material's vapor pressure at the various temperatures is extremely important to derive this quantities, but this value can be hard to correctly derive, so experimental values have been tabulated, as in the graph reported in Figure 2.2.

2.2 PULSED LASER DEPOSITION

Pulsed Laser Deposition (PLD), is a physical vapor deposition (PVD) technique which enables the deposition of high-quality thin films of a very wide range of materials[43]. It can be said to have been first developed in 1965, when Smith and Turner utilized a ruby laser for the first time to deposit thin films[44], and it is presently being employed in numerous experimental studies.

As Figure 2.3 shows, the structure of a PLD system is actually quite simple, compared to other thin-film techniques, and consists only of a vacuum chamber presenting one or more windows, a target carousel and the sample stage.

Although the experimental setup is easy to describe, the underlying physical phenomena are quite complex[45], with some unclear aspects still the subject of numerous studies, and careful analysis needed to describe the deposition process, while empirical attempts are required to obtain a thin film with the desired characteristics.

The key element of this approach is, as the name suggests, the use of a high energy laser capable of short pulses to instantaneously evaporate, melt and ionize the selected target, ablating part of it and creating a luminous "plasma plume" which reaches supersonic speed[46].

The plume is composed of highly energetic neutrals, ions and electrons which upon reaching the substrate, give place to nucleation of the film.

One of the main advantages when using Pulsed Laser Deposition is its capability of maintaining the stoichiometry of the employed target, and even of reproducing the chemical composition of complex materials, like Yttrium Barium Copper Oxide (YBCO).

However, PLD-deposited thin film present two major issues, the first being that because of the high orientation of the plume normally to the target's surface, the area upon which it is possible to obtain films of uniform height is only of about 1 cm^2. The other is that sometimes small droplets (~10μm) of molten material can reach the substrate and solidify, lessening the quality of the thin film.
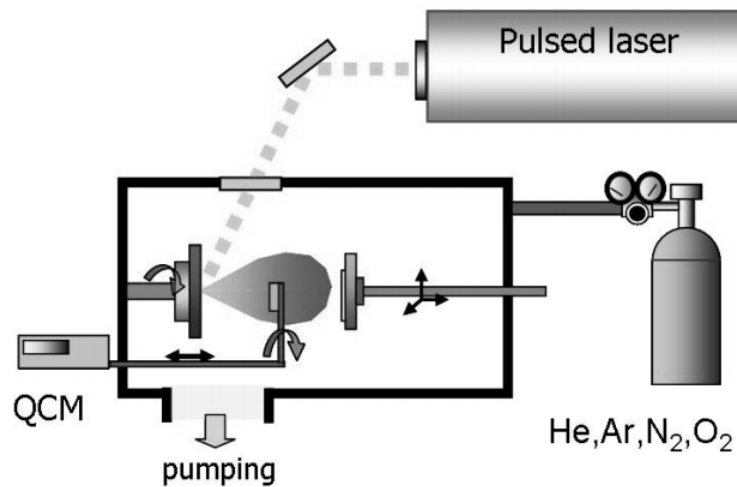
Figure 2.3 Schematic of Pulsed Laser Deposition Setup

The beam produced by the laser is deviated and focused by a system of optical lenses, guiding it through the window so that it hits the target, made of the material that will compose the deposited film. The fact that the energy source is completely external to the deposition chamber and that there is no need for filaments, theoretically makes PLD one of the cleanest techniques for the growth of thin films.

The target is collocated on a carousel, usually this support has the ability to move along at least one axis and to rotate, so that it is possible by using program-controlled motors to make the spot of laser beam hitting the target follow a spiral path. This is done in order to assure that the surface is ablated in a uniform way, and that the shape of the plasma plume doesn't change in the course of the deposition process.

Moreover, the carousel can be fitted with multiple, interchangeable targets of different materials, and this has the very important consequence of being able to deposit multilayered films without breaking vacuum.

The whole deposition process can be divided in several phases, each having influence on the quality and morphology of the resulting film; Figure 2.4 provides an overview of what happens in the first step, the ablation of material from target's surface after the latter is hit by the laser pulse[47]. A parameter belonging to this section which has great impact on many characteristics is the fluence per pulse (measured in J/cm^2) delivered by the laser.

This is followed by the crossing of the ablated particles of the space between target and substrate. When the deposition is not performed in UHV, but with a background gas atmosphere, an important role is played by the distance just mentioned: in fact, depending on if it is larger or smaller than the plasma plume length, different film growth modes can be observed:

- If smaller, not enough collisions can happen, and clusters can't nucleate and the resulting deposition is compact
- If larger, clusters do nucleate before impinging on the substrate, and the film tends to be nanostructured.

The atmosphere can be of both inert and reactive gases and, while it must be low enough for the ablated material to reach the substrate, it can be useful in slowing the more energetic particles, which would otherwise damage its surface or have a sputtering effect on the already deposited film.

Moreover, an O_2 pressure is often employed when depositing oxides from a stoichiometric target, since it enhances the quality obtained by assuring that the layer has the correct composition and doesn't present oxygen deficiency.

The final phase is the actual nucleation and deposition of the film.
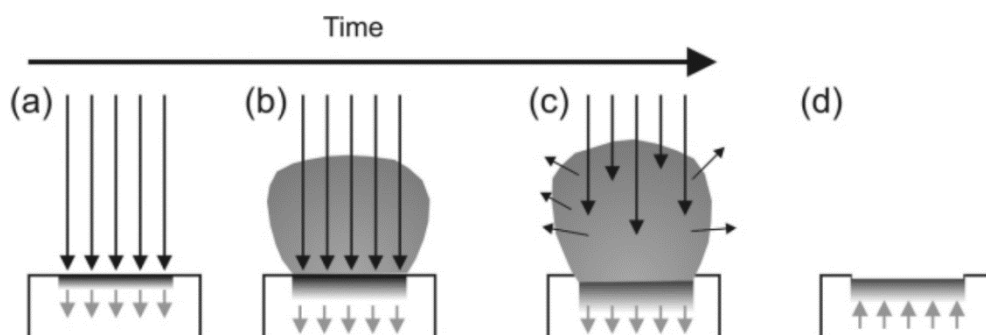
Figure 2.4 Schematic illustration of the key elements of the ablation event. (a) Initial absorption of laser radiation, melting and vaporization. (b) Melt front propagates into the solid, vaporization continues and laser-plume interactions start to become important. (c) Absorption of incident laser radiation by the plume, and plasma formation. (d) Melt front recedes leading to eventual re-solidification.[47]

2.3 SCANNING TUNNELING MICROSCOPY

2.3.1 Introduction to Scanning Probe Microscopy

The use of microscopy has always been of fundamental importance in Surface Science, where a precise knowledge of the superficial structure and morphology of a sample is needed to understand how they influence its physical and chemical properties.

The classical microscopes relied on the optical imaging of a small area of the sample, but these techniques had a very limited resolution, due to the diffraction of light.

So as the interest of the scientific community focused on a smaller and smaller scale, microscopes based on completely different physical mechanisms were needed: these were the electronic microscopes and, later, the Scanning Probe Microscopes (SPMs), able to distinguish the single atoms belonging to the surface.

SPMs are a family of techniques based on the measurement of different kinds of interactions between the sample and a very sharp tip, which can assume different shapes according to the method employed.

These microscopes are able to create the array of measurement points needed for the imaging, and thus to control the relative motion of tip and sample in the three dimensions at this extremely small scale, by utilizing piezoelectric elements, which are materials capable of transforming an electrical input in a mechanical output, or vice versa.

There are numerous different types of Scanning Probe Microscopes, categorized by the kind of physical interaction that the system measures, such as electrostatic, magnetic, thermal, et cetera; but the most common are the Atomic Force Microscope (AFM) and the Scanning Tunneling Microscope (STM).

STM, which was used in the course of this thesis, was the first example of Scanning Probe Microscope developed, having been invented by Binnig *et al.*[48] in 1982, and is still of pivotal importance in the most advanced studies of Surface Science and Nanotechnology, thanks to its very high resolution.

2.3.2 Quantum Tunneling Theory

As was said in the previous section, the key element of a Scanning Tunneling Microscope is a metal tip, usually made of transition metals like Tungsten or Platinum-Iridium, which is brought extremely close to the surface of the sample examined, in the sub-nanometer distance.

At this scale, a physical phenomenon takes place: Quantum Tunneling. It describes the flow of electrons between two electrodes when the distance between them is small enough, even if this middle region forms a potential barrier which should make it impossible, according to classical physics.

This is due to the superposition, inside the barrier region, of the wave functions of electronic states belonging to the two electrodes, resulting in a finite transmission probability, exponentially dependent on the barrier's width, as will be seen later.

Moreover, by applying a small potential bias, it's possible to change the energy levels involved in the exchange, and in this way give rise to a non-zero net electrical current between the two elements, whose direction depends on the sign of the applied voltage.

In a STM system, the two electrodes are represented by the tip and the sample, while the barrier region can be any dielectric fluid, for example air or water. Nevertheless, while not strictly required, STM are almost always performed in vacuum, to ensure no surface contamination during measurement.

Here will be presented what is perhaps the simplest and most intuitive theoretical model for Quantum Tunneling, its main assumptions are:

- Single-particle, stationary system
- The potential barrier is considered only a function of position, U(r)
- For further simplification, a mono-dimensional system with rectangular potential barrier is assumed.

The objective is to find the stationary states of this kind of system, by finding the solutions to the Schrödinger equation, and then to apply the current density operator, so as to obtain the tunneling current and the transmission coefficient.

In these conditions, the potential barrier can be defined as

$$U(z) = \begin{cases} U_0 & if \ z \in (0, z_0) \\ 0 & elsewhere \end{cases}$$

While the time-independent Schrödinger equation for the wave function of the stationary states is

$$\left[-\frac{\hbar^2}{2m} \frac{d^2}{dz^2} + U(z) \right] \psi(z) = E\psi(z)$$

Where E is the total energy of the electron, which from here on will be considered inferior to the potential barrier, E<U_0, since this is the condition that is being analyzed. The general solution for the three regions composing the system can be written in this way:

$$\psi(z) = \begin{cases} A_1 e^{ik_1 z} + B_1 e^{-ik_1 z} & if \ z < 0 \\ A_2 e^{-k_2 z} + B_2 e^{k_2 z} & if \ z \in (0, z_0) \\ A_3 e^{ik_1 z} + B_3 e^{-ik_1 z} & if \ z > z_0 \end{cases}$$

Having introduced k_1 and k_2, respectively denoting:

$$k_1 = \sqrt{\frac{2mE}{\hbar^2}}$$
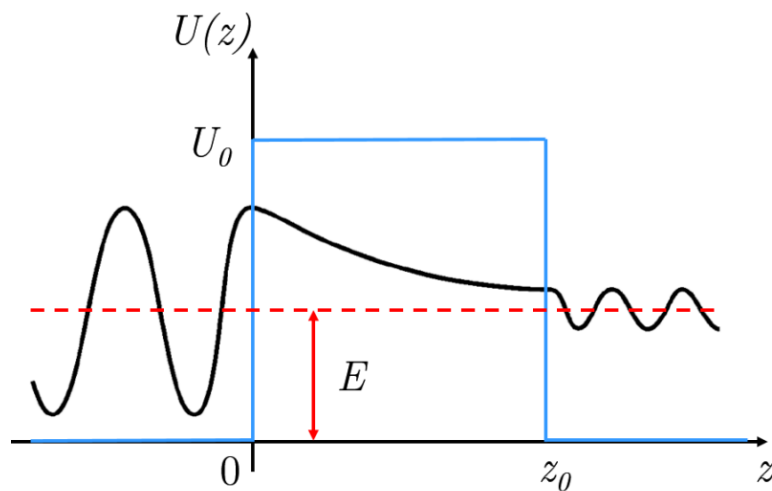
Figure 2.5 Schematic model of the tunnel effect with monodimensional rectangular potential barrier. The depicted oscillating function represents the real part of the wave function of an electron with energy *E*, which passes through the barrier (having width z_0 and height U_0).

$$k_2 = \sqrt{\frac{2m(U_0 - E)}{\hbar^2}}$$

A first assumption that can be made to simplify this system of equations is to consider the electron as coming from the left, in this way A_1 becomes the amplitude of the incident wave, and B_3 can be written off, since in this ideal system an electron moving towards the positive axis in the $z > z_0$ region has no way to be reflected.

The subsequent step is to apply the boundary conditions, which are due to the continuity of the wave function and of its derivative at the interfaces of the three regions, that is to say at z=0 and a $z=z_0$. This allows to write the various constants of the previous system of equations as a function of A_1.

Finally, the tunneling current can be deduced by applying to the solution the current density operator, which has the form

$$J = \frac{i\hbar e}{2m} \left(\psi^* \nabla \psi - \psi \nabla \psi^* \right)$$

The transmission coefficient, the ratio between the incident current and the transmitted one, can also be found, and if the barrier is wide and tall enough, that is to say if the condition $k_2 z_0 \gg 1$ holds true, it can be approximated as

$$T \approx 16 \frac{k_1 k_2}{(k_1 + k_2)^2} e^{-2k_2 z_0}$$

And then by substituting the definitions of k_1 and k_2, this final equation is written:

$$T \approx 16 \frac{E(U_0 - E)}{U_0^2} e^{-2k_2 z_0}$$

The most important element of this formula is the exponential dependence of the transmission on the factor $-2k_2 z_0$, and thus to the electron energy E, to the barrier height U_0 and to the barrier width z_0, remembering the expression for k_2. This relation is precisely what allows the Scanning Tunneling Microscope to reach its sub-atomic vertical resolution, as will be explained later.

The previous analysis, while being an easy way to grasp the concept of quantum tunneling, is also severely limited, since by considering a single-particle, stationary model it can't describe the phenomenon in terms of transitions between the electronic states of the tip and the electronic states of the sample, but only as stationary states of the whole system.

This is clearly insufficient for understanding STM (and especially STS, Scanning Tunneling Spectroscopy) measurements, where the tunneling current dependence on the electronic properties of the sample is one of the fundamental aspects to be known to interpret the experimental data.

A more complex approach is then necessary, such as that proposed by Bardeen[49]: based on the theory of time-dependent perturbations, it makes use of the Transfer Hamiltonian (TH) formalism to express the tunneling effect in terms between the electronic states of the two electrodes.

Bardeen's model considers an initial, unperturbed system, which is composed of the two isolated subsystems, consisting of tip and sample; the interaction due to quantum tunneling is then introduced as a perturbation of this initial system.

Shifting to formulas, since in the unperturbed system the subsystems are isolated, the initial total Hamiltonian operator $\hat{H}_0$ can be expressed as the sum of those of the tip and the sample, respectively denoted by $\hat{H}_t$ and $\hat{H}_s$:

$$\hat{H}_0 = \hat{H}_t + \hat{H}_s$$

When the distance between tip and sample is reduced, the two subsystems cannot be considered as isolated anymore, and so the total Hamiltonian changes with respect to the initial one, $\hat{H}_0$. This variation, due to the quantum tunneling interaction, can be written in the form of a sum of $\hat{H}_0$ and a perturbation operator, expressed as $\hat{H}'$.

$$\hat{H} = \hat{H}_0 + \hat{H}'$$

If the perturbation can be considered small, meaning if $\hat{H}_0 >> \hat{H}'$, it is possible to employ the first order approximation for time dependent perturbation theory. In this approximation, the transition probability per unit time between the eigenstates of the unperturbed system can be calculated by using the famous Fermi golden rule,

$$\tilde{P}_{ab} = \frac{2\pi}{\hbar} |M_{ab}|^2 \delta(E_a - E_b)$$

Here E_a and E_b are the energies of the electronic states involved in the transition, respectively belonging to the tip and to the sample, whereas M_{ab} is the matrix element of the perturbation operator, which can be written as

$$M_{ab} = \langle b|\hat{H}'|a\rangle$$

While it is possible to apply Bardeen theory and the transfer Hamiltonian formalism to a many-particles system, in order to obtain a very general result, it is indeed quite complex, so for the sake of simplicity a new set of assumptions will be introduced, in order to only consider single-particle states, as has been done in various important literature papers.

The most important of this assumptions is to treat the electrons as independent particles, this means not only considering the electron-electron interactions as negligible, but also neglecting the contribution of electronic spin. This last part of the approximation cannot however be applied when spin has a fundamental role in the measurements obtained by the instrument, as is the case for spin-polarized scanning tunneling microscopy and spectroscopy (SP-STM and SP-STS).

The second assumption is called the "exact separability" hypothesis and it permits to obtain an explicit expression for the matrix element present in the previous formula. It says that, if the total system is divided in two regions, one which contains the tip and is called Ω_t, while the other contains the sample and is defined as Ω_s, then the single-particle eigenstates of the entire system coincide with the single-particle eigenstates of the isolated tip in the Ω_t region, and with the single-particle eigenstates of the sample in the Ω_s region.

In this way, it is possible to calculate the matrix element M_{ab} without the need to explicitly define the perturbation operator $\hat{H}'$ and, if consider electronic transitions from the sample to the tip, the result obtained is

$$M_{\nu\mu} = -\frac{\hbar^2}{2m}\int_\Sigma \left(\phi_\mu^*\nabla\psi_\nu - \psi_\nu\nabla\phi_\mu^*\right)\cdot\boldsymbol{n}\,d\sigma$$

Where ϕ_μ is a state of the sample, ψ_ν is a state of the tip and Σ an arbitrary surface belonging to the barrier between the two regions in which we have divided the system, Ω_t and Ω_s. To instead obtain the matrix element corresponding to transitions from the tip to the sample, the position of ϕ_μ and ψ_ν in the formula must be exchanged.

After substituting this expression for the perturbation operator's matrix element into Fermi golden rule, and then calculating the occupation probability of each state through Fermi-Dirac distribution, the tunneling current can be obtained by summing over all possible transitions.

In order to have a resulting non-zero net current, the application of a voltage bias V is needed: it is conventionally considered V>0 when the sample is positively polarized with respect to the tip, since the latter is usually grounded in a STM configuration.

If one final approximation is introduced, that the applied bias is large compared to thermal energy ($k_bT<<eV$), the occupation probabilities of tip and sample can be simplified as Heaviside functions, and the expression for tunneling current becomes:

$$I = \frac{4\pi e}{\hbar} \int_0^{eV} \sum_{\mu,\nu} |M_{\mu\nu}|^2 \, \delta(E_\nu - E)\delta(E_\mu + eV - E) \, dE$$

The interval to which the integral has been applied to is limited by Pauli Exclusion Principle to the range (0,eV), where zero is set as the sample's Fermi level. Only electronic states having energy belonging to this interval contribute to the tunneling phenomenon, and the dependence of this contribution on their configuration is included in the term $M_{\mu\nu}$, as shown earlier.

A schematic representation of the situation can be seen in Figure 2.6, where a positive bias is applied to the sample, shifting its Fermi level to a lower energy level and establishing a tunneling current from the occupied electronic states of the tip to the empty ones of the sample. Should the applied voltage be negative, the effect would be an inversion in the net current's direction.

While Figure 2.6 shows the case of a metallic sample, Scanning Tunneling Microscopy can also be used to study the surface of a semiconductor, but in this case another factor is introduced: the band gap, the prohibited energy interval between conduction and valence bands.

The presence of this region with no states available for tunneling causes the tunneling current to strongly depend on the bias applied, since tunneling is only possible if V is strong enough,

for example as in Figure 2.7; this variation in the data obtained with a different voltage bias is extremely useful in the interpretation of STM images.
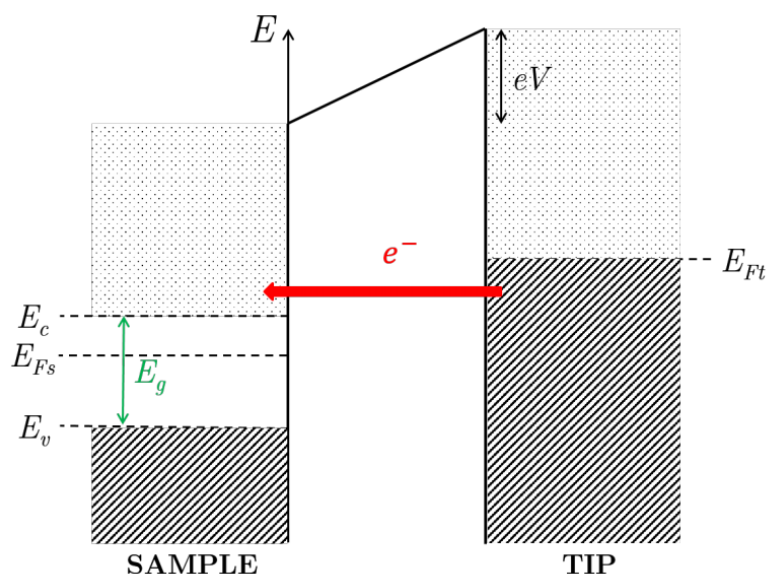
Figure 2.6 Scheme of the energy levels involved in tunneling between the tip and the sample. The sample is positively biased with respect to the tip and electrons perform a transition from the tip occupied states to the sample empty states within the energy interval (0,eV).
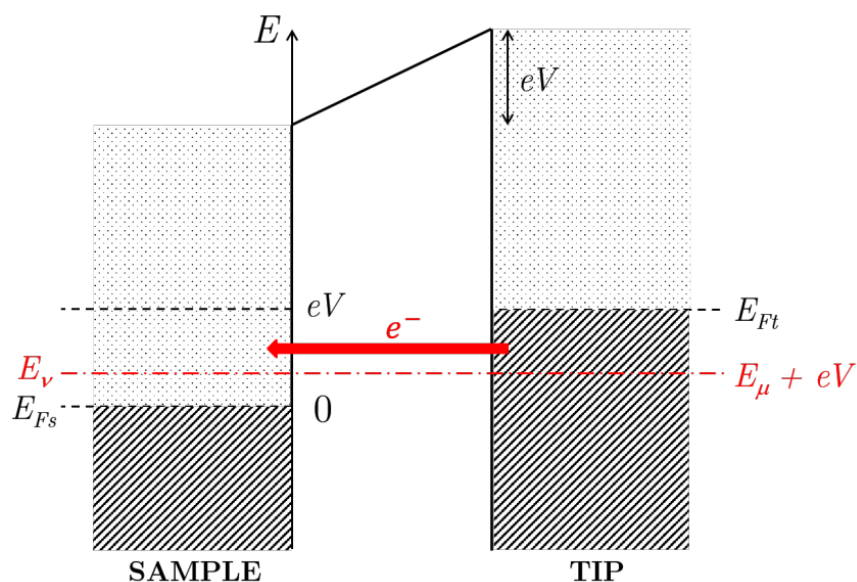
Figure 2.7 Scheme of the energy levels involved in tunneling for a semiconductor sample. The positive applied bias is high enough to let electrons pass from the tip occupied states to the empty states in the conduction band of the sample.

The first model for the interpretation of STM imaging was proposed by Tersoff and Hamann[50,51] in 1983 and builds upon the perturbative approach to Transfer Hamiltonian formalism which has been previously discussed.

The Tersoff-Hamann model assumes the tip's apex to be locally spherical, possessing center of curvature **r₀** and radius R, as is more clearly shown in Figure 2.8: this enables a simplification in the analysis of the tunneling current, by considering it to be due only to states of the tip having spherical symmetry, and neglecting the contribution of states having different symmetries.

In this way, the wave function for a state of the tip can be written as

$$\phi_\mu(\boldsymbol{r}) \propto \frac{e^{-k_t|\boldsymbol{r}-\boldsymbol{r_0}|}}{k_t|\boldsymbol{r}-\boldsymbol{r_0}|}$$

Where **r₀** is again the center of curvature of the tip and $1/k_t$ is the decay length of the wave function. Inserting this in the previously derived formula, is then possible to calculate the matrix element of the TH for a generic state of the sample.
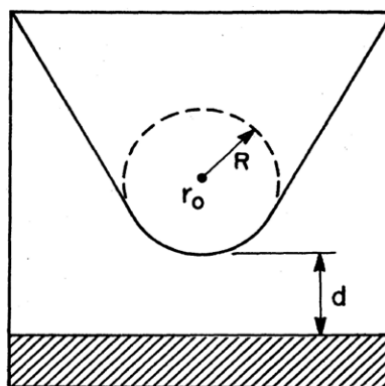
Figure 2.8 Schematic picture of tunneling geometry. Probe tip has an arbitrary shape but it is assumed locally spherical with radius of curvature R, where it approaches nearest the surface (shaded). Distance of nearest approach is d. The tip center of curvature is labeled as **r₀.**

The formula for tunneling current derived by using Bardeen's model can be further approximated in the limit of low temperature and small applied bias, where the integral can be considered as rectangular and simply transformed into a product:

$$I \approx \frac{4\pi e^2 V}{\hbar} \sum_{\mu,\nu} |M_{\mu\nu}|^2 \delta(E_\nu - E_F)\delta(E_\mu - E_F)$$

E_F is the Fermi energy of the sample, which is also that of the tip in the present approximation. If the matrix element obtained for spherical tip wave functions is substituted in the previous formula, the result has the shape

$$I \propto V\rho_t(E_F)\rho_s(E_F, \boldsymbol{r_0})$$

Here ρ_t is the density of states, DOS, of the tip at the Fermi energy, defined as

$$\rho_t(E_F) = \sum_\mu \delta(E_\nu - E_F)$$

While ρ_s is the sample's local density of states, LDOS, at the Fermi energy and in the center of curvature $\boldsymbol{r_0}$ and can be written as

$$\rho_s(E_F, \boldsymbol{r_0}) = \sum_\nu |\psi_\nu(\boldsymbol{r_0})|^2 \, \delta(E_\nu - E_F)$$

Recapitulating, according to the Tersoff-Hamann model, if the STM images are collected at low voltage bias and at constant current, they represent the surface level of the sample's LDOS at the Fermi Energy

The theoretical model examined, which assimilates the tip states to only spherical wave functions, is however unable to explain the atomic resolution imaging that can be obtained even for densely packed metallic surfaces, with the observed spatial resolution (2-3 Å) practically half of the predicted one (6 Å).

The reason for this effect was found by studying the materials that are usually utilized for making STM tips, transitional metals such as Tungsten (W). In fact, Ohnishi[52] and Tsukada[53] have shown that a tungsten tip, ending with a singular W atom, is characterized by having at the apex a d_{z^2}-like electronic state, possessing an energy level just below Fermi energy and a bandwidth in the order of 1ev[54].

Moreover, Doyen et al.[55] found that it's possible for the d-state just described to be at the Fermi energy, instead of just below it. In such a situation the contribution to the LDOS of tip electronic states with non-spherical symmetry not only can no longer be neglected, but becomes dominant.

Because of this, a new model was introduced by Chen[56,57], with the objective to account also for tip wave functions with angular momentum *l* different from zero, and particularly those symmetric with respect to the tip axis, such as p_z and d_{z^2}.

In Chen's approach, the tip wave functions are developed in spherical harmonics, to then reach the following expressions for the matrix element of the Transfer Hamiltonian for the electronic states mentioned:

$$M_{s,v} \propto \frac{1}{k_t}\psi_v(\boldsymbol{r_0})$$

$$M_{p_z,v} \propto \frac{1}{k_t}\frac{\partial}{\partial z}\psi_v(\boldsymbol{r_0})$$

$$M_{d_{z^2},v} \propto \frac{1}{k_t}\left[\frac{\partial^2}{\partial z^2} - \frac{1}{3}k_s^2\right]\psi_v(\boldsymbol{r_0})$$

Indicating with k_t and k_s the inverse decay length of tip and sample states, respectively.

As can be seen, in the case of a tip state having symmetry *s*, the matrix element is proportional to the sample's state wave function, exactly as in the Tersoff-Hamann model, whereas if the state considered has symmetry p_z or d_{z^2} the situation is different: for a *p* state the proportionality is to the first derivative of the wave function, while for a *d* state it's to the second derivative, both considered at the center of curvature. This correlation is called the *derivative rule[58]*.

This different dependence has a few consequences, such as possible inversion of contrast and enhanced atomic corrugation for atomically resolved STM images, and the predicted resolution is confrontable to the experimental ones for metallic surfaces, indicating that Chen's approach is a reasonably correct method for interpreting STM imaging.

2.3.3 Operating principles of Scanning Tunneling Microscopy

Having now concluded an elementary analysis of the physical phenomenon which is exploited for STM imaging, Quantum Tunneling, it is time to more clearly describe the structure and the working mechanism of this microscope, a simplified version of which can be seen in Figure 2.9.

As previously mentioned a metallic tip is brought at an extremely small distance (5-7 Å) to the surface of the sample whose topography one wants to study, while making sure to avoid contact between them, which would damage it; the tip must in fact be as sharp as possible, ideally ending in a single atom in order to have maximum precision in the measurements, and is usually made of transition metals by means of electrochemical etching.

The tip is in most cases grounded, so a small voltage in the order of 1 V is applied to the sample, in order to obtain a tunneling current in the nanoampere range, flowing through the vacuum barrier from the occupied states of the tip to the empty ones of the sample's surface if the bias is positive, and from sample to tip in the opposite situation.

STM is a scanning technique, this means that by having the tip move along the surface, information is collected point-by-point in a two-dimensional array, which is then processed so as to show an image on the display. The scanning procedure consists in the analysis of all
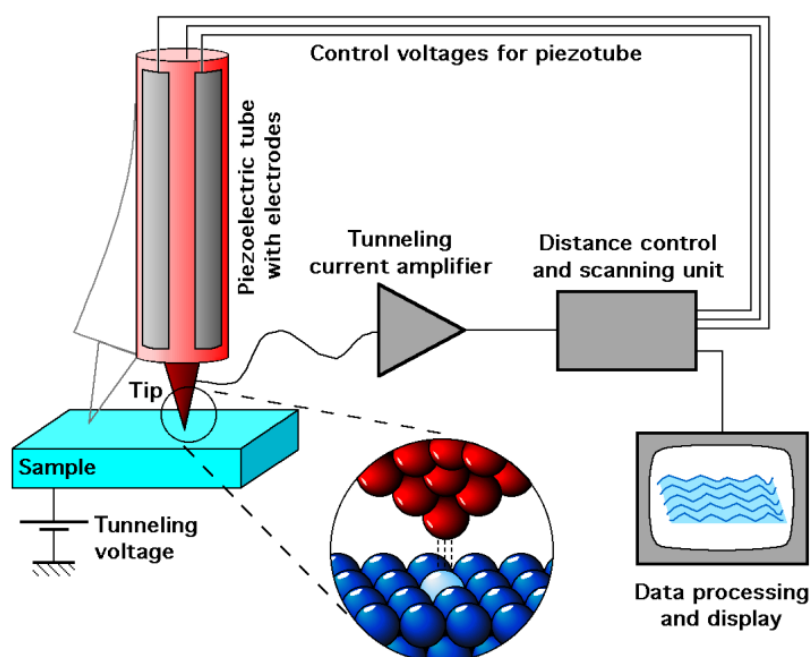

Figure 2.9 Schematic diagram of a scanning tunneling microscope

points in the x-axis, and again on the way back, before advancing one step along the y-axis and repeating: in this way the user can simultaneously check two different images, one defined "forward" and the other "backward", with glaring differences between the two indicating problems in the measure.

The tip's position and movement in the three dimensions can be accurately controlled even at this nanoscopic scale thanks to piezoelectric elements, positioned in its support: this particular category of materials has the ability to transform electrical stimuli in mechanical responses, or vice versa, and can thus be made to expand or retract by a certain amount by applying carefully calibrated voltages.

The tunneling current is exponentially dependent on the distance between tip and sample, and so two operating modes for STM imaging are possible, which are exemplified in Figure 2.10, both of them following the earlier described method for scanning in the x and y axes, but differing in their behavior along the z-axis.

The first, and the one normally used, is called the *constant current mode*: in it, the system tries to maintain the tunneling current at a certain, preset constant value, thanks to a feedback circuit. This means that for each point, the tunneling current is measured and if it is lower than the set value the tip is brought closer, or otherwise the distance is increased, until it matches with the preset.

When this happens, the value of the voltage applied to the piezoelectric is saved, and thus indirectly the height of the tip at constant distance from the sample, producing the image on the display.

The second mode allows for higher scanning speed, and is called the *constant height mode*: in this case there is no need for a feedback circuit, since the z coordinate of the tip is kept

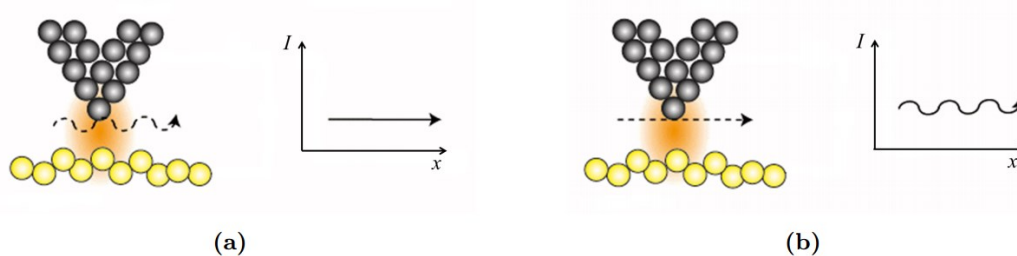(a)   (b)

Figure 2.10 Operating modes of a scanning tunneling microscope. (a) Constant current mode. (b) Constant height mode.

constant during the surface scanning; what is measured is instead the tunneling current as a function of the (x,y) position. This operation mode can however be risky, since if the surface analyzed is rough, or presents large impurities, the absence of the feedback circuit can make the tip crash, damaging it.

It must be noted that the tunneling current depends not only on the distance between tip and sample at a fixed bias, but also on the surface electronic properties of the area measured, and so the images obtained are actually a combination of a morphological and an electronic components, a fact which can be highlighted by taking successive images at different applied bias.

One of the main issues one has to confront when building and operating a STM is the need to stabilize the relative position and distance of tip and sample at a sub-Angstrom scale when the components considered are as much as nine orders of magnitude bigger[59].

This can be done by avoiding thermal drift, for example by making sure that the temperature is kept constant throughout the system, and most of all by minimizing the effect of ambient vibrations by making the structure as rigid as possible and by employing a decoupling mechanism between the structure and the STM elements.

A characterization technique closely related to STM is Scanning Tunneling Spectroscopy, STS, which will be briefly introduced here because of its great importance in surface science.

The objective of STS is to collect information about the electronic structure and the local density of states (LDOS) of the sample by analyzing the behavior of the tunneling current with the variation of the applied voltage, more precisely by measuring the differential conductivity, dI/dV, and then applying normalization methods.

The differential conductivity can be obtained by simply interrupting the feedback system if the STM is working in constant current mode, a voltage ramp (symmetrical to the zero) is then applied and the tunneling current is measured at each step, making possible to compute dI/dV. A more precise method is however almost always employed, which consists in the use of lock-in amplifier.

A lock-in amplifier induces in the applied voltage a small, sinusoidal modulation characterized by a precise frequency, which must be higher than the cutoff frequency of the STM control system, so that the tip does not oscillate at the same frequency due to variations in the current. After separating the constant and modulated values of the the tunneling current, this permits an easier and more accurate way of detecting the differential conductivity, in the form of $\Delta I/\Delta V$, which are respectively the current and the voltage modulation amplitudes.

There are two STS operating modes, the first is the one earlier described and is called point spectroscopy, the seconds is the scanning of a surface in constant current mode while the lock-in modulation is active: in this way for each point of the raster $\Delta I/\Delta V$ at the selected bias is collected, and it's possible to create dI/dV maps (or conductance maps).

2.4 EXPERIMENTAL APPARATUS

The syntheses and characterizations of this thesis were performed in the Micro and Nanostructured Materials Laboratory (Nanolab) of Politecnico di Milano.

The experimental apparatus was composed of three ultra-high vacuum (UHV) chambers, interconnected but with the possibility to be closed off as needed, for example during a deposition process.

This allowed the transition from deposition to characterization without having to expose the sample to atmosphere, and at the same time to avoid contamination of the analysis instruments by the pressures established during deposition

The preparation chamber contained the various elements necessary during the synthesis procedure: it held an ion gun for surface sputtering, an e-beam evaporator for EB-PVD and a sample heater. In addition, facilities for Low-Energy Electron Diffraction (LEED) and Auger Electron Spectroscopy (AES) were also present.

The analysis chamber instead contained the Scanning Tunneling Microscope, in particular an Omicron UHV VT-STM. These first two chambers are commercial, made by Omicron, and usually characterized by a base pressure in the order of 10^{-10} mbar, measured by means of bayard-Alpert hot-filament ionization gauges.

The third chamber was custom-made specifically to hold the PLD system, and contained a motor controlled target carousel and sample holder, with a base pressure of 10^{-8} mbar.
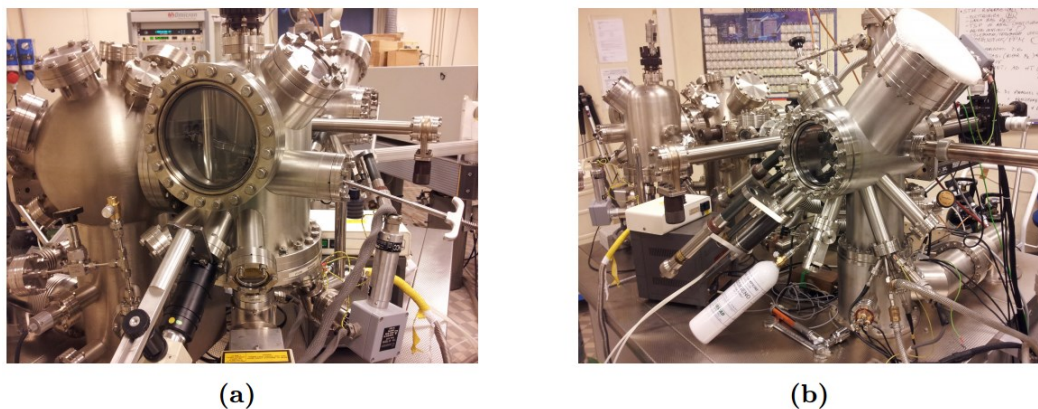

Figure 2.11 STM apparatus: (a) analysis chamber; (b) preparation chamber.

3 EXPERIMENTAL RESULTS AND DISCUSSION

In this chapter, the experimental results obtained over the course of this thesis will be presented and discussed: after an introduction to the structure of the Au(111) surface (Section 3.1.1), the cleaning procedure followed for the preparation of the substrate, necessary to achieve a surface suitable for thin film deposition, will be described (Section 3.1.2).

Afterwards, the work regarding electron beam physical vapor deposition will be presented, first briefly focusing on the deposition of metallic zinc (Section 3.2.1) and then more thoroughly on the ZnO structures observed with this technique (Section 3.2.2).

In section 3.3, will be described the experiments performed by means of pulsed laser deposition and, finally, all the results will be summarized, discussed and compared to those found in literature (Section 3.4).

3.1 THE Au(111) SURFACE

3.1.1 Structural Description

In depositions, the substrate plays an extremely important role, and an incorrect choice in its structure and properties can make it impossible to obtain the desired material. In the experimental studies presented in Section 1.4.2, regarding the synthesis of two-dimensional ZnO, the (111) surface of a metallic substrate was utilized, mainly Pt, Pd, Au and Ag.

This is because, theoretically, the fact that they possess the same kind of hexagon symmetry and similar lattice dimensions should ease the formation of graphene-like ZnO instead of the wurtzite phase. In this thesis, it was decided to use as substrate the Au(111) surface.

Gold has been the substrate of choice for numerous surface deposition techniques and experiments not only because of its resistance to oxidation in standard conditions, which makes it easier to avoid surface contamination and other unwanted phenomena, but also because it presents a distinctive surface reconstruction.

This is a property gold shares with many other metals, but it's the only one[60] with a face centered cubic (FCC) structure to exhibit it on the (111) surface. The reconstruction has been extensively studied with various methods, such as helium atom scattering (HAS)[61], in order to propose a model for its unit cell.

Figure 3.1 shows the unit cell of the Au(111) surface reconstruction, which, as can be seen, is 22 times longer and $\sqrt{3}$ times larger than the unit cell of the unreconstructed Au(111) surface, and is thus defined as a (22x$\sqrt{3}$) reconstruction. Its main feature is however the fact that it presents a transition between different stacking regions: as demonstrated in Figure 3.1, the sides of the cell are characterized by FCC stacking, same as the bulk, but in the central zone it shifts to a Hexagonal close packed (HCP) configuration.

This change between FCC and HCP causes a uniaxial compression of the crystalline structure, which allows the gold surface to allocate 23 atoms along the direction $\langle 1\bar{1}0 \rangle$, one more than the atomic sites of the bulk structure underneath.
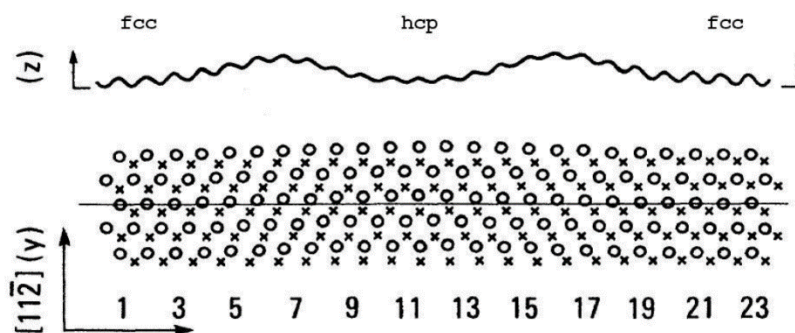

Figure 3.1: Model of the (22 × √3) reconstructed cell. Above, the topographic profile along the $\langle 1\bar{1}0 \rangle$ direction. Below, the schematic representation of the atomic sites within the cell: the crosses denote the positions of atoms in the second layer, whereas open circles denote the positions of atoms in the reconstructed top layer.

It also causes the atoms of the transition zones to be in a bridge position, and in this way higher than the surface plane, giving place to a corrugation of about 0.2 Å, whose two ridges, referred to as discommensuration lines, run parallel to the $\langle 11\bar{2} \rangle$ direction.

The fact that the Au(111) surface presents a $(22 \text{x} \sqrt{3})$ reconstruction has been directly observed and confirmed by STM imaging, as for example in Figure 3.2a, which has atomic resolution and highlights the unit cell of this superstructure and the different stacking regions. As predicted, the two discommensuration lines in the image are characterized by a lighter color, indicating their being higher than the rest of the surface, due to corrugation.

If the surface is however analyzed at a larger scale, like in Figure 3.2b, it is observed that the ridges do not run perfectly straight and parallel, but instead possess a "zig-zag" path, the so-called herringbone reconstruction.

This particular kind of superstructure is energetically convenient since thanks to symmetry the system has three directions equivalent to $\langle 1\bar{1}0 \rangle$, positioned at angles 120°, and by developing a regular pattern of domains aligned along different directions, it can relax the uniaxial stress caused by the reconstruction.

It is clearly shown in Figure 3.2b that there are actually two types of discommensuration lines, depending on their behavior at the bending points, the "elbows" of the superstructure, and that they always exist in pairs.

The ones that follow a more regular path are called Y ridges, while the others, the X ridges, tend to diverge from a simple zig-zag shape, shifting more towards the FCC region if the turning angle is convex and towards the HCP region otherwise, creating what are respectively referred to as bulged and pinched elbows.

In addition, even a clean, freshly prepared surface of Au(111) presents numerous defects, belonging to different categories, which have been studied thoroughly by Barth et al[63]. They consist predominantly of U-shaped connections between adjacent X and Y discommensuration lines, interrupting the regular reconstruction pattern, which typically contain the HCP domain and only rarely a FCC domain. This phenomenon can be observed near certain terrace steps or at the interface between zones of the surface which have different orientations.

(a)   (b)
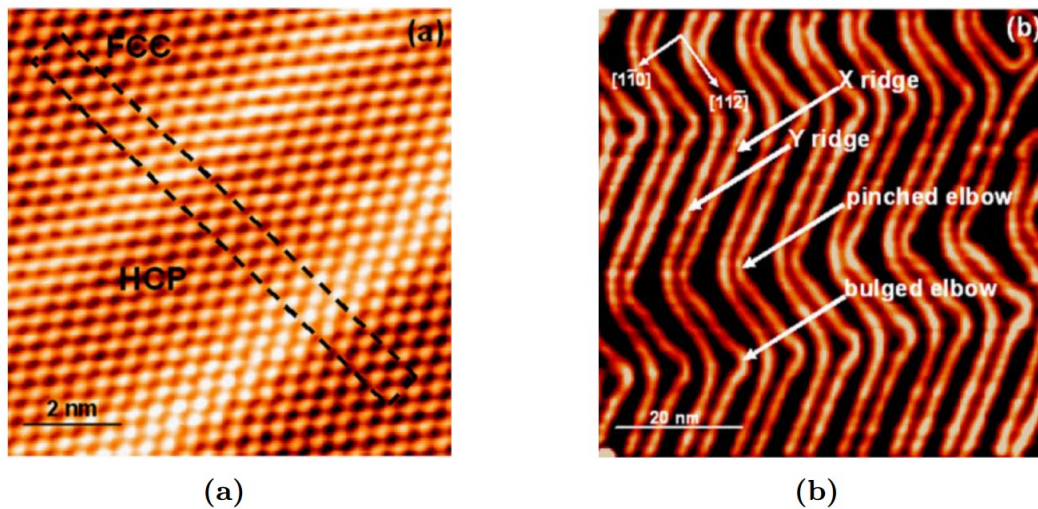
Figure 3.2 Clean Au(111) surface. (a) Atomically resolved STM image (b) Large scale STM of the typical herringbone surface reconstruction of Au(111)[62]

The gold (111) surface presents a superficial lattice constant equal to 2.86 Å in the FCC and HCP regions, which due to the uniaxial compression discussed earlier changes to 2.72-2.75 Å along the ridges and is again lowered to 2.65-2.68 in the presence of elbows[64], where the applied stress is stronger.

The different kinds of lattice sites created by the distortion are energetically non-equivalent and this is why the herringbone reconstruction is one of the reasons for the interest in Au(111) as a substrate in depositions: ridges and especially elbows can be a matrix of ordered preferential sites for the nucleation of nanostructures and thin films.

As will be shown later, over the course of this thesis there was no indication that the nucleation of both Zinc and Zinc Oxide on this substrate is characterized by any kind of preferential site of initiation, and a possible explanation for this will also be provided.

Finally, a secondary effect of the herringbone reconstruction, not as physically relevant but convenient during analysis, is that it makes it easy to distinguish if the surface observed is that of gold during simple STM imaging.

3.1.2 Substrate Preparation

The Au(111) surfaces which acted as substrates for this thesis belonged both to gold single crystals as well as Au thin films on mica samples; since there were no differences in the results produced by the two types, in the following sections no distinction will be made between them.

After introduction in the vacuum chambers, the samples were kept for a few hours at a temperature of about 850 K: this procedure is called outgassing and is done in order to completely eliminate adsorbed gaseous species, by using a sample heater system.

This system can work in two ways, resistive heating or direct heating: in the first mode a current goes through an electrical resistance placed just below the sample, while in the other the current can pass directly through the sample holder itself, this allows for higher temperatures, up to 1500 K instead of 1000 K. The temperature reached is measured with very good approximation by a thermocouple positioned in close proximity.

The samples' surface was then cleaned by means of one or more cycles of Ar^+ sputtering at high temperature, and the same was done after each deposition experiment. In the sputtering system an external Argon line is connected to the chamber by a high precision valve, which makes it possible to regulate the very small gas flux needed.

The entrance of the Argon is close to an ion gun, where a filament produces electrons by thermionic emission, which are accelerated by an applied positive potential and by impacting on the gas atoms create Ar^+ ions. The ions are in turn accelerated by a negatively polarized grid and deflected by a magnetic field, resulting in an ion beam that can be focused on the surface of the sample.

When the high energy ions hit the surface they give place to the sputtering process, which is the removal by impact of the first atomic layers of the surface, where there may be impurities as well as previously deposited films, leaving only the pristine metallic surface underneath. The various properties of the beam can be modified by regulating the parameters of the system, for example the ion's kinetic energy by varying the voltage applied to the negative grid or the spot size by means of the magnetic field.
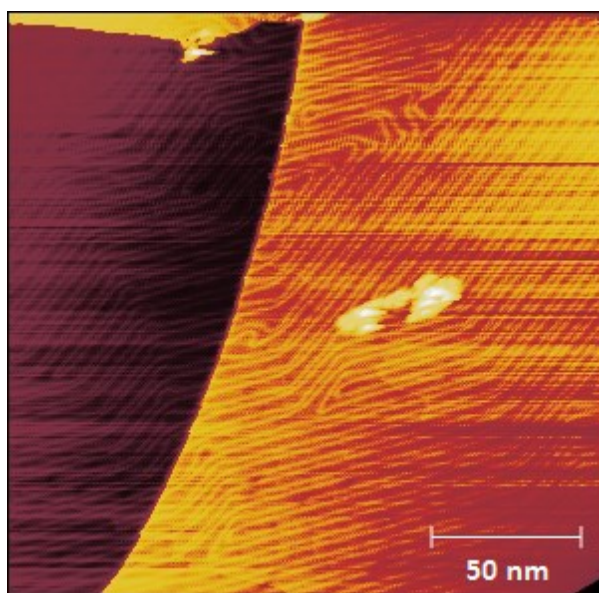
Figure 3.3 STM image of the Au(111) surface, (200x200) nm. It shows the presence of clean terraces and the ordered herringbone reconstruction.

In the course of this thesis the standard procedure has been 10 minutes of Ar^+ sputtering at 1 KeV at about 850 K, followed by an annealing process were the sample was left for at least 30 minutes at that temperature. This was done in order to allow the surface to reconstruct and regain order after the damage caused by the disruptive sputtering process, promoting the release of any remaining adsorbed species and the growth of large area atomic terraces, necessary for thin film deposition and characterization.

Before beginning the subsequent deposition process, the sample was transferred to the analysis chamber and, after having waited for it to cool down to room temperature in order to avoid distortions by thermal drift, the surface was checked by STM imaging to control that the cleaning procedure had been successful. The condition of the Au(111) surface of a sample, shortly after the preparation procedure described, is shown in Figure 3.3.

Figure 3.3 is a "large scale", (200x200) nm image of the cleaned substrate, and it can be seen that there are large atomically flat regions, presenting sharp edges and extremely few impurities. The presence of well-arranged discommensuration lines, which were discussed in the previous section, proves that a good level of structural order was obtained.

All these factors confirm that this process results in a suitable substrate for thin-films deposition while profile measurements indicated an apparent height of 2.7 Å for the atomic terraces, comparable with the value 2.4 Å reported in other studies[65].

3.2 E-BEAM PHYSICAL VAPOR DEPOSITION

3.2.1 Metallic Zinc Deposition

The first part of the experimental analysis carried out in this thesis consisted in the deposition of pure zinc on the Au(111) surface of a gold substrate, after having prepared the latter according to the procedure explained in the last section. The morphology of the thin films and nanostructures obtained was then observed with the use of Scanning Tunneling Microscope.

Zinc was deposited by means of an e-beam evaporator, described in Section 2.1, a vacuum technique based on the use of high energy electrons, which are deviated onto the surface of the evaporant, in the case of this system a 99.99% pure zinc rod. This flux of electrons heats the material locally, and causes the sublimation of zinc atoms, some of which pass through a narrow opening directed to the sample holder.

The main goal for this part of the experimental study was to verify that the chosen method was a reliable way to deposit metallic zinc, which was then oxidized in an attempt to achieve graphene-like ZnO.

Of interest was also the observation of the structures formed by pure zinc, to be later able to distinguish those corresponding to the oxide, examining the typical shape and size, the apparent step height as well as if they presented any kind of preferential nucleation.

The evaporator system didn't give exact values of evaporation rate and total quantity of material evaporated, it instead gave information about the charge current and the total charge, respectively, which had passed through its shutter during the deposition process.

With the hypothesis that the concentration of ions in the evaporated zinc didn't change during the deposition, it was possible to obtain a constant evaporation rate by keeping the charge current fixed: in this way the quantity of deposited material resulted proportional to the duration of the deposition.

During the course of these experiments, the detected flux of ions through the opening of the evaporator was kept constant and equal to 2 nanoampere, by regulating two parameters of the evaporator, the current passing through the tungsten filament and the voltage applied to it, which usually had values of about 1.3 A and 500 V, respectively. All depositions of metallic

zinc were carried out at room temperature in UHV, with background pressures in the order of 10^{-10} or 10^{-11} mbar.

Differently from the case of the clean gold surface and the zinc oxide, prior to the imaging of deposited metallic zinc there was no post-annealing process to allow the deposited material to reconstruct thanks to the higher thermal energy.

This is because not only there was no benefit for the successive experimental steps, but also it could have caused damage to the substrate by diffusion of zinc into the gold and intermixing.

In deposition characterized by a low quantity of zinc, commonly referred to as low "coverage" depositions, as in the amount of the gold surface that is covered by the deposited material, it can be observed that zinc tends to grow at step edges, as well as form small islands, which do not present preferential nucleation with respect to the elbows of the discommensuration lines produced by the Au(111) herringbone reconstruction.

This is actually in accord with theoretical predictions made by Meyer et al.[66], who suggested that preferentiality was due to place exchange between adatoms and substrate atoms at the elbows, followed by trapping of further adatoms, and was possible only if the deposited
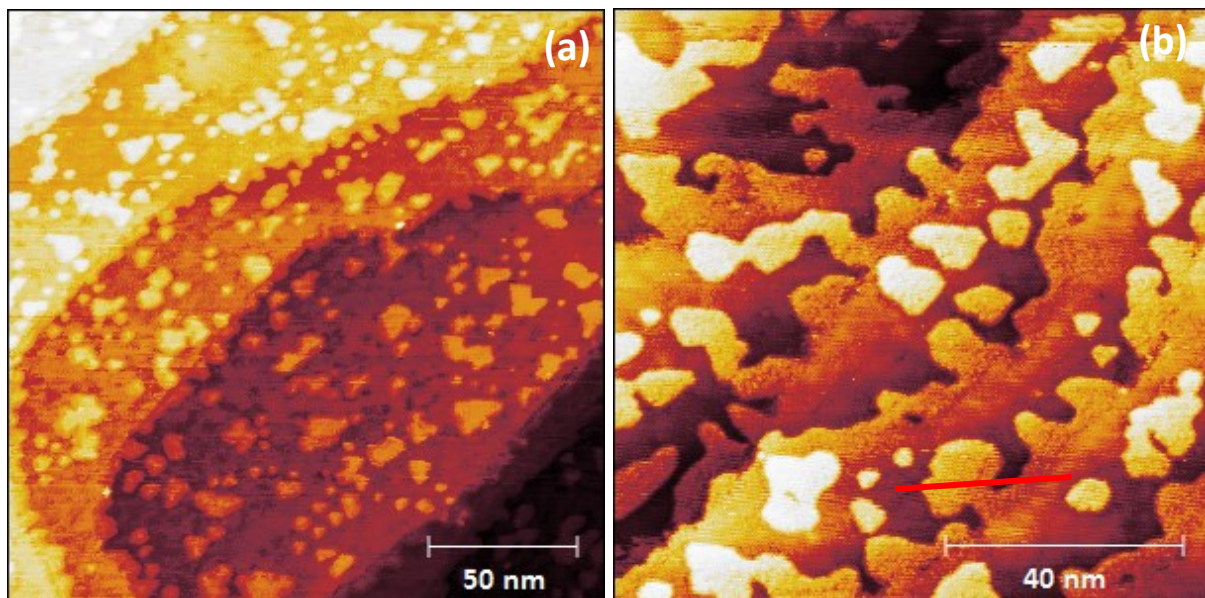

Figure 3.4 STM images of zinc on Au(111): (a) lower coverage, (200x200) nm; (b) higher coverage, (100x100) nm. The different appearance of gold and zinc can be observed.

material had higher than gold surface free energy and heat of sublimation, properties which zinc doesn't possess.

FIgure 3.4 shows two different depositions of zinc, in (a) the duration of the evaporation process was set to 3'20", whereas in (b) it was longer, at 5 minutes, resulting in a visibly higher quantity of zinc. In both images, zinc can be differentiated from the Au(111) surface thanks to a different texture.

Differently from the case of other metals, such as titanium[9], in which an increase in coverage yields to the formation of more small islands, until a saturation level is reached, zinc instead presents a growth of the average dimension of the islands, which tend to coalesce, along with the creation of contiguous zinc structures at the edges of the gold terraces.

In all the experiments conducted, the Zn nanostructures were characterized by a flat surface, and their apparent height was found to be about 2.3 Å, as indicated by the line profile highlighted in Figure 3.4 and reported in Figure 3.5.
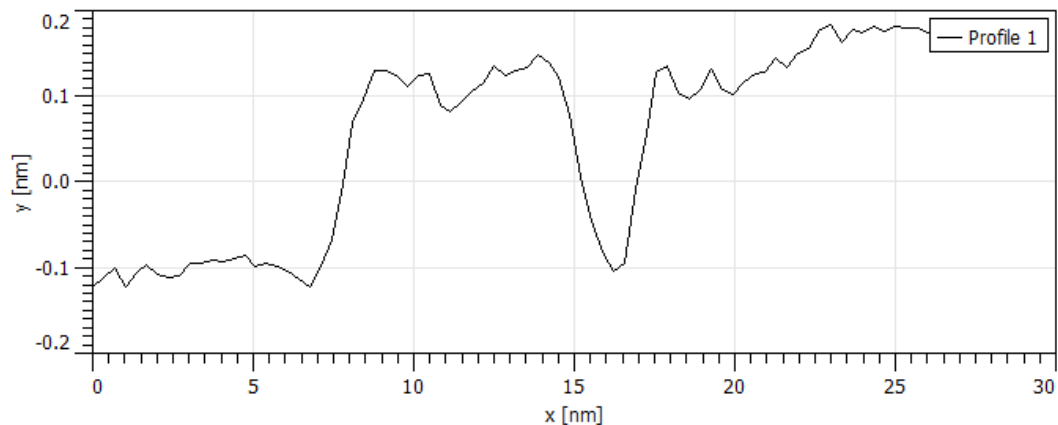

Figure 3.5 Line profile of Zn on Au(111), along the direction highlighted in Figure 3.4

3.2.2 Zinc Oxide Deposition

In this analysis, two approaches were taken for the deposition, by means of electron beam physical vapor deposition, of zinc oxide ultrathin films on the Au(111) surface.

The first approach was the exposure of the samples presented in the previous section to an oxygen pressure at higher temperatures, in order to induce oxidation of the already deposited zinc: this is called the post-oxidation method; while the other consisted in the introduction of oxygen in the sample preparation chamber even before the deposition process began, to make the evaporated zinc react with the oxygen atmosphere and try to directly deposit zinc oxide, in what is referred to as a reactive deposition.

When considering post-oxidation, the parameters which could be modified in an attempt to observe the desired g-ZnO structure were the oxygen pressure present during the process and the temperature at which it was carried out. The duration of the oxidation process was kept mostly constant, at 30 minutes.

It must be noted however that in all the experiments which will be discussed there was a limit to the oxygen pressure admissible inside the vacuum chamber, equal to $5*10^{-6}$ mbar and indicated directly by the system manufacturer, in order not to risk damage to the more delicate components and filaments. This limit was not present in depositions made by Pulsed Laser Deposition, which will be discussed in the next section.

The temperature needed to be as high as possible, so as to better promote the oxidation reaction, but not high enough to cause desorption of zinc or zinc oxide from the substrate; moreover, the presence of oxygen lowered the maximum working temperature of some components, as said above. By utilizing information present in literature (see Section 1.4.2), as well as empirical data, an oxidation temperature of about 570 K was found to be a good compromise.

After the oxidation process, the oxygen was removed from the preparation chamber, and the sample was subjected to a standard post-annealing treatment, at a higher temperature, about 600 K. The aim of this operation was to create better ordered thin films and nanostructures and to facilitate the release of adsorbed but not bonded oxygen.
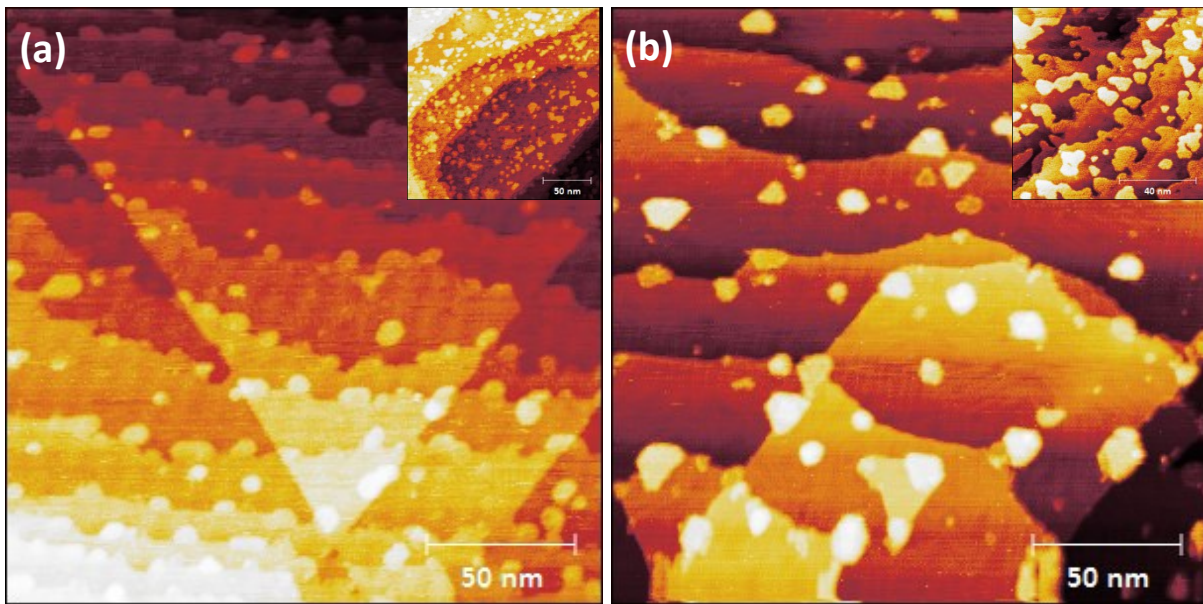
Figure 3.6 STM images of ZnO on Au(111), obtained by post-oxidation in O_2 of different quantities of metallic zinc; (200x200) nm. The insets show the respective samples before the post-oxidation process.

After being kept at this temperature for 10-15 minutes, the sample was left to cool down to room temperature and taken to the analysis chamber, where its surface was analyzed with a scanning tunneling microscope.

The images in Figure 3.6 show the results obtained by using the oxidation procedure described on the metallic zinc on Au(111) samples which were illustrated in the previous section (Figure 3.5), and which are reported here as insets to allow for easier comparison.

Unfortunately, even when the most favorable conditions for oxidation were utilized, only a few of the observed structures showed regular geometry, and their surface was not characterized by an ordered appearance, specifically it didn't show a moiré pattern, which was instead seen in various earlier studies. Also, the STM images were often very disturbed, presenting numerous current spikes, which were however not present when other materials were analyzed, excluding the possibility of it being caused by the instrument itself.

Both factors were concluded to be symptoms of an incomplete oxidation of zinc, the difficulty in oxidizing zinc was also reported in some articles[30], where it was indicated the need to use stronger oxidant agents, such as NO_2, or different techniques like reactive deposition.

On one occasion promising results were obtained, although far inferior to those illustrated later in this section, and are illustrated in Figure 3.7. This indicates that this kind of approach was not intrinsically wrong, but that probably the employed conditions were insufficient to consistently fully oxidize the material.

In the larger scale image is possible to observe that a larger quantity of deposit remained on the gold surface, which exhibited a tortuous and interconnected morphology; most importantly, higher resolution STM images such as Figure 3.7b showed that these planar structures were characterized by a texture called moirè.

With the term moiré is generically indicated a pattern which is created by the superposition of two lattices having different periodicity, the moiré will be characterized by a coincidence lattice, whose size is a multiple of the unit cells of both elements.

In this case it is created by the ZnO atoms of the newly formed layer being positioned in different positions with respect to the gold lattice underneath. Since both the Au(111) surface and the graphene-like ZnO present a lattice with hexagonal symmetry, the resulting moiré lattice is also characterized by this symmetry.

This phenomenon was observed in most of the studies reported in Section 1.4.2 regarding the deposition of g-Zno on metallic surfaces, and as such was considered a sign of its successful synthesis in this thesis.
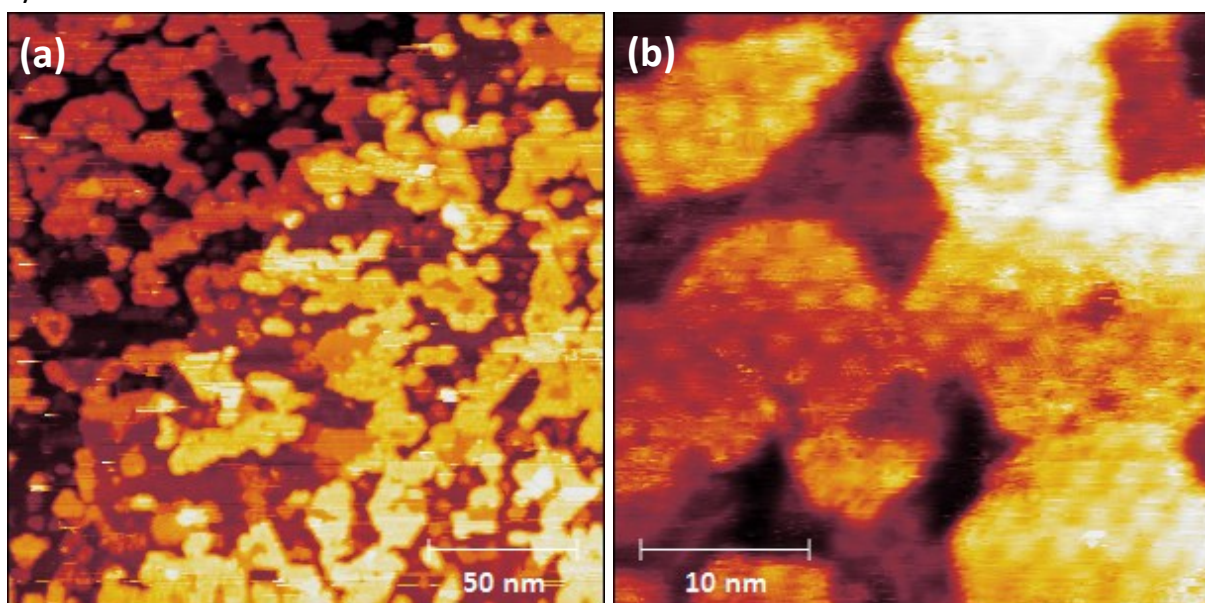

Figure 3.7 STM images of ZnO on Au(111), obtained by post-oxidation in O_2, presenting moiré pattern. (a) (200x200) nm; (b) (35x35) nm.

As described in Section 2.3, the particular working mechanism of a STM means that the data obtained is a combination of the morphological and electronic features of the surface analyzed. This means that the observed corrugation can be structural, i.e. due to an actual displacement of the surface atoms, or it can be a pattern in the electronic states, produced by interactions between substrate and deposited material, or the sum of both.

Later in this section an analysis of the variation in the moiré profile with the applied voltage will be presented, which seems to indicate that this phenomenon has a mostly electronic nature.

As explained above, within the limits imposed by the system and the material, a post-oxidation treatment was found to be insufficient for reliably obtaining g-ZnO thin-films. The focus of the experiments was thus turned to a reactive deposition approach, which is also one of the most employed techniques in the studies presented in Section 1.4.2.

Before the start of the deposition process, oxygen was made to enter the preparation chamber by means of high-precision valve, until the maximum allowed pressure of $5*10^{-6}$ was reached.

The deposition of ZnO was again done by means of an e-beam evaporator, maintaining a constant evaporation rate by adjusting the filament current and the voltage applied (at about 1.3 A and 600 V, respectively).

The samples were then usually subjected to a two-phase thermal treatment: during the first one, which lasted about 30 minutes, the oxygen was not removed from the chamber, and the sample was kept at temperatures of about 540 K, with the objective of reaching complete oxidation and stoichiometry of the deposited ZnO layers.

The second part consisted in further heating up to 600 K, in UHV condition for about 10 minutes, in order to stimulate the release of adsorbed impurities, as well as molecular oxygen, and the re-organization of the nanostructures formed. It can be said that this is basically the same procedure utilized for the post-oxidation approach, the only difference being the addition of oxygen also during the deposition.
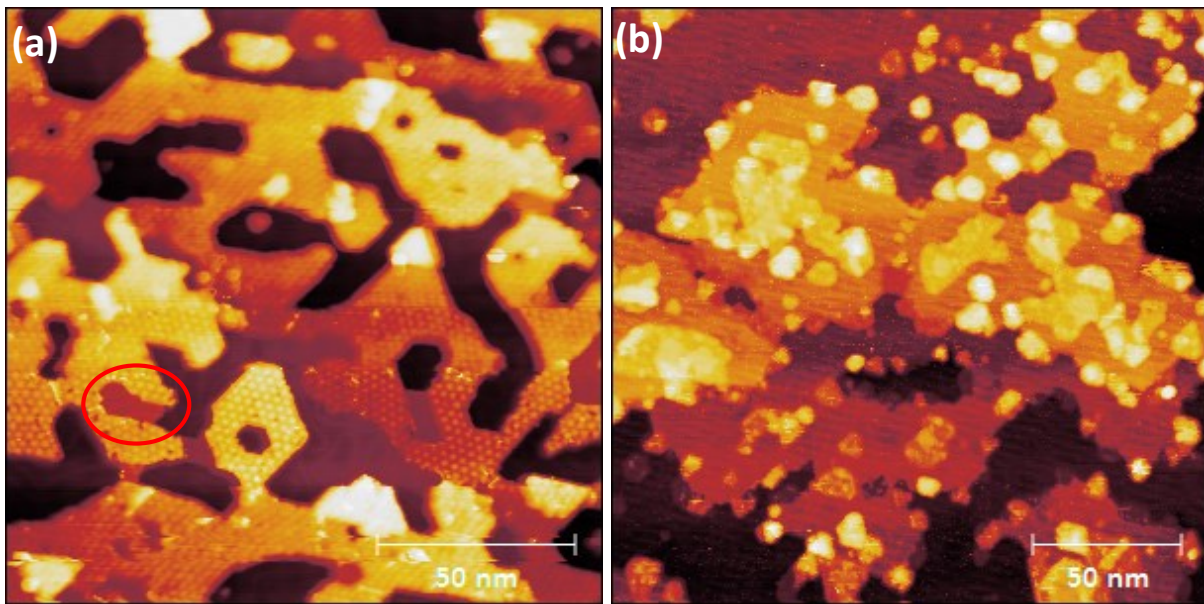
Figure 3.8 STM images of ZnO on Au(111), (a) reactive deposition in O_2, (150x150) nm, the circle highlights a gold "patch"; (b) deposition in UHV, (200x200) nm.

A glaring example of the great impact which the use of reactive deposition had on the resulting structures can be seen in Figure 3.8, the two images depict samples prepared in exactly the same conditions and with the thermal treatment described above, the only difference being the presence of oxygen during deposition (reactive deposition, Figure 3.8a) or its absence (post-oxidation, Figure 3.8b).

Apart from a visible increase in the quantity of material remaining on the substrate, by employing a reactive deposition, the small, irregular islands observed in the post-oxidation case were substituted by ample, interconnected structures. Moreover, an extremely ordered moiré pattern characterized by hexagonal symmetry is shown, which can be said to confirm that what is observed is indeed graphene-like ZnO.

In this particular case, the zinc oxides seems to grow preferentially upon the gold near a step edge, and profile measurements indicated an average height of 1.3 Å with respect to the gold on the same level.

In this image, and also in various others presented later, small gold islands ("patches"), which are one atomic step higher than the surrounding Au(111) surface, can be seen, for example the one highlighted in Figure 3.9. These patches were never present just after the preparation of the Au(111) surface, and suggest that during the growth of zinc oxide thin-films, there is
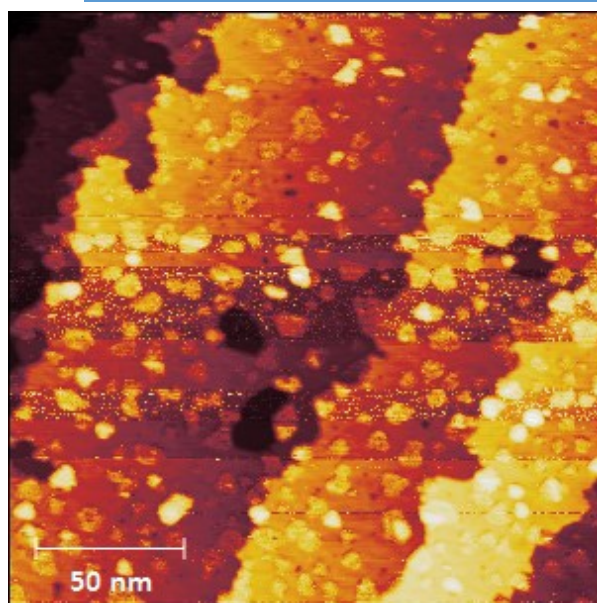
Figure 3.9 STM image of ZnO on Au(111), obtained by reactive deposition not followed by exposure to O2 at high temperatures, (200x200) nm.

also a concurrent diffusion of gold atoms which reconstruct the surface. This further complicates the analysis of the morphology of the deposited thin-film, and was also observed, among others, by Shiotari et al., regarding the deposition of ZnO on Ag(111).

The fact that reactive deposition alone was not enough, and that an exposure to oxygen at higher temperatures was still required even with this method, in order to obtain graphene-like ZnO, was also verified.

To this aim another sample was prepared, with the same quantity of zinc evaporated and in the same conditions as in the one shown in Figure 3.8a, but this time the first phase of the thermal treatment was skipped, and only the UHV post-annealing was done.

It is clear to see, from Figure 3.9, that a "post-oxidation" process is crucial even when considering reactive depositions, since in this case small, irregular structures were again observed, similar to those previously seen in the non-reactive deposition. The instability in the imaging was also probably an indication of the presence of impurities or other defects in the synthesis.

Another aspect considered was whether the duration chosen for the thermal treatments was enough for the system to reach the optimal reconstruction, or if an increase in duration in the

post-oxidation and annealing processes would enable the system to further reorganize itself into more regular structures.

With this objective a pair of identical depositions were again carried out, differing only in the fact that in one the duration of the two phases of the procedure was increased to 45 minutes at 540 K in presence of oxygen and 15 minutes at 600 K in UHV, instead of the usual 30 and 10 minutes, respectively. Although not shown here, since there were only small differences, STM analysis demonstrated that the standard procedure utilized was more than enough for the system structure to stabilize, and subsequent heating only had marginal benefits.

An interesting analysis, on the evolution of the morphology of the ZnO thin-films along with an increase in coverage, was made possible by slightly changing the position of the sample, so that it was no longer perfectly aligned with the evaporator's aperture during the deposition process.

In this way, a coverage gradient was obtained in the different zones of the substrate, and the fact that all the analyzed structures belonged to the same deposition had the major benefit of excluding the possibility of the results being influenced by a variation in parameters other than the quantity of material.

The morphology in four different positions of the sample is shown in Figure 3.10: when the coverage is very low, the smaller oxide islands obtained don't present regular shapes and surfaces, only the few bigger ones do. With an increase in coverage the ZnO structures begin to clearly show the moirè pattern, and assume mostly hexagonal shapes, with the borders aligned along preferential directions of the coincidence lattice.

In Figure 3.10d the nucleation of further layers is observed upon some of the zinc oxide elements; interestingly, in many cases these new layers tend to assume triangular geometry, characterized by three moirè "peaks". In the last image, at higher coverage, this can also be seen, along with the coalescence of the some of the islands, which begin to form the uniform interconnected structure.
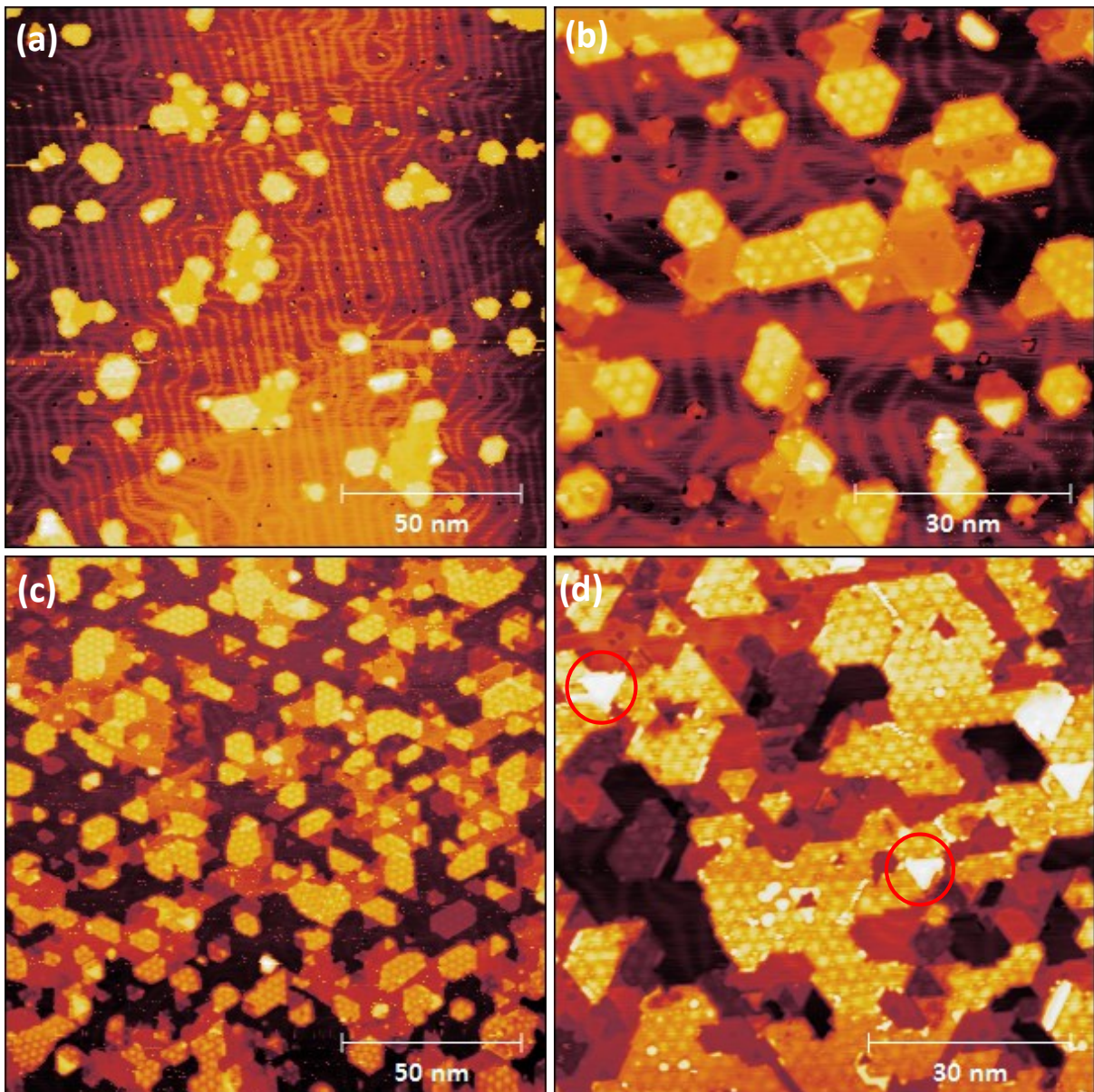
Figure 3.10 STM images of ZnO on Au(111), realized on the same sample thanks to a coverage gradient. (a,c) (150x150) nm, (b) (75x75) nm and (d) (80x80) nm. The triangular geometry of the onsets of successive layers is highlighted.

All the images, however, denote a strong modification in the morphology of the Au(111) substrate, with the formation on the clean surface of small patches of gold, in a measure proportional to the quantity of ZnO present. The oxide can be found in small quantities on the background gold surface, but seems to grow preferentially upon these patches.

Figure 3.11 STM images of ZnO on Au(111), (65x65) nm, at different applied bias: (a) +1.5 V ;(b) +1.0 V ;(c) +0.5 V and (d) +0.2 V. Where significant, line profiles of the moiré pattern are reported.

The height observed for ZnO is about 1.3 Å, compared to the nearest level of Au, while the difference in height between "first" and "second" layer is about 2 Å, this is shown in the line profiles relative to Figure 3.12a and 3.12b, respectively.

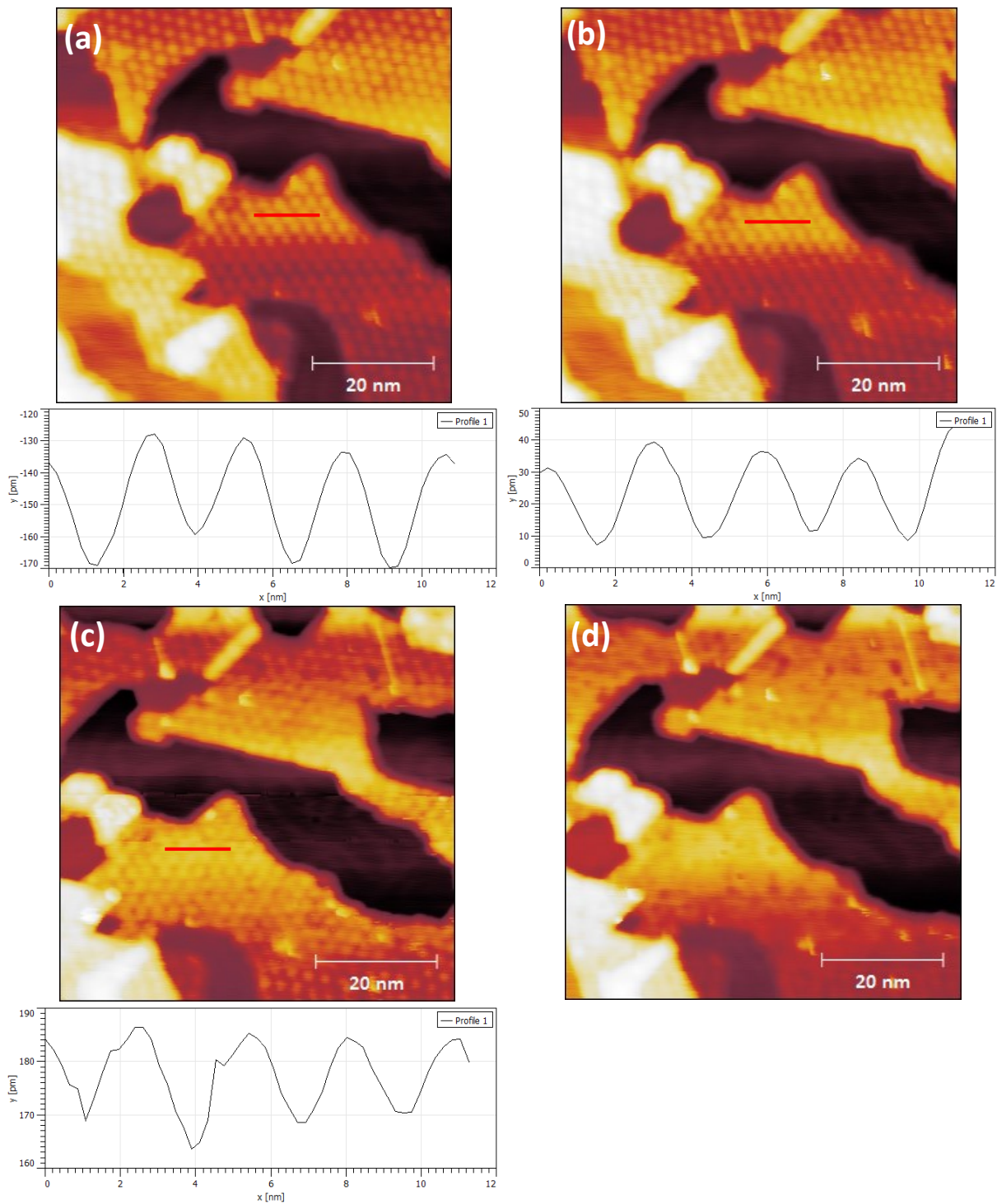Finally, Figure 3.11 shows a few STM images taken in the same position, but each characterized by a different applied voltage, as specified in the caption. The line profiles show a dependence of the corrugation produced by the moiré pattern on the voltage at which the measurements were made.

In fact, its amplitude goes from about 0.4 Å with a +1.5 V bias, to 0.25 Å at +1.0 V, 0.15 Å at +0.5 Å and seems to almost disappear for lower values, as shows the example at +0.2 V. For negative applied voltages, not shown in the figure, the situation was practically the same, with higher modulus bias resulting in stronger corrugation.

As mentioned earlier, this indicates that the observed moiré, instead of being generated by a periodic vertical displacement of ZnO atoms, placed in different positions on the Au lattice beneath, is mostly due to a variation in the local density of states.
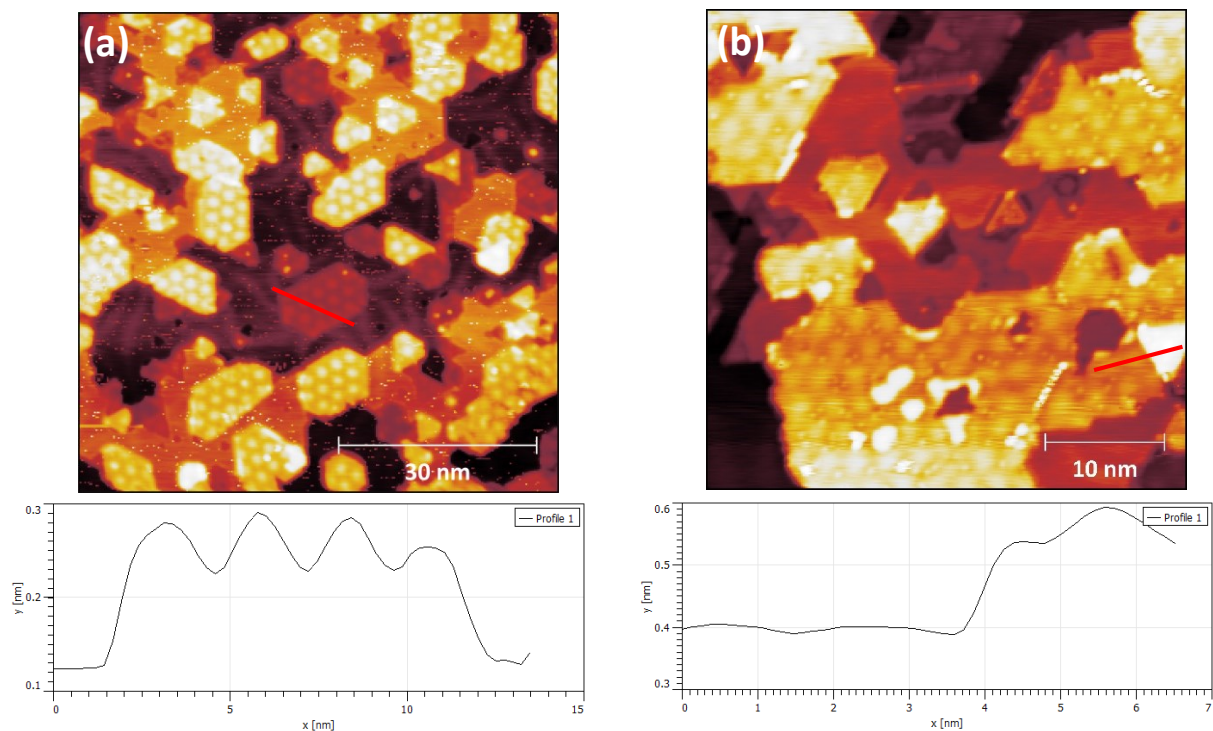
Figure 3.12 STM images of ZnO on Au(111), (a) (80x80) nm (b) (40x40) nm. Line profiles relative to the first and second layer are given.

Summarizing, these were the optimal conditions found in this experimental analysis in order to successfully synthesize graphene-like ZnO by means of EB-PVD:

- Reactive deposition, with O_2 pressure as high as possible, at least $5*10^{-6}$ mbar

- Post-oxidation, in the same atmosphere, at 540 K for 30 minutes

- Annealing, in UHV, at 600 K for 10 minutes.

3.3 PULSED LASER DEPOSITION OF ZnO

The second technique utilized for the deposition of ultra-thin ZnO films on the Au(111) surface was Pulsed Laser Deposition.

In the case of these experiments the target was made of stoichiometric Zinc Oxide. While this eliminates the need for a post-oxidation, numerous studies have demonstrated that a similar exposure to O_2 at high temperature can be beneficial when depositing oxide thin films, since it removes the oxygen deficiencies created during the deposition. This proved to be true also in these experiments.

In the experimental tests performed, the distance between the target and the sample was mostly kept constant at about 5 cm, and a stabilized pulse energy of 200 mJ was utilized. Based on the size of the spot generated, the lens focal length, the angle formed with the target and the energy loss along the optical path, this was found to coincide with a fluence of about 200 mJ/cm^2.

If the value of energy per pulse was lowered too much, it was no longer enough to cause the ablation of material from the target, Figure 3.13a shows the results of using a value of 125 mJ: there is no visible ZnO deposition, only the clean Au(111) surface.

After the deposition process was concluded, the sample was transferred to the preparation chamber, where it was subjected to a standard post-annealing treatment in UHV, and was kept at about 600 K for 10 minutes. As in the case of e-beam deposition, this was done to promote the release of any adsorbed impurities, as well as the reconstruction of the deposited material into more ordered structures.

Other than target-sample distance and pulse energy, the other parameter which could be varied was the number of pulses employed in a deposition. Since this analysis focused on extremely small quantities of deposited material, in the range of a couple of monolayers, only a few laser pulses were needed. Images (b), (c) and (d) in Figure 3.13, in fact, represent the results obtained by using one, five and ten pulses, respectively.
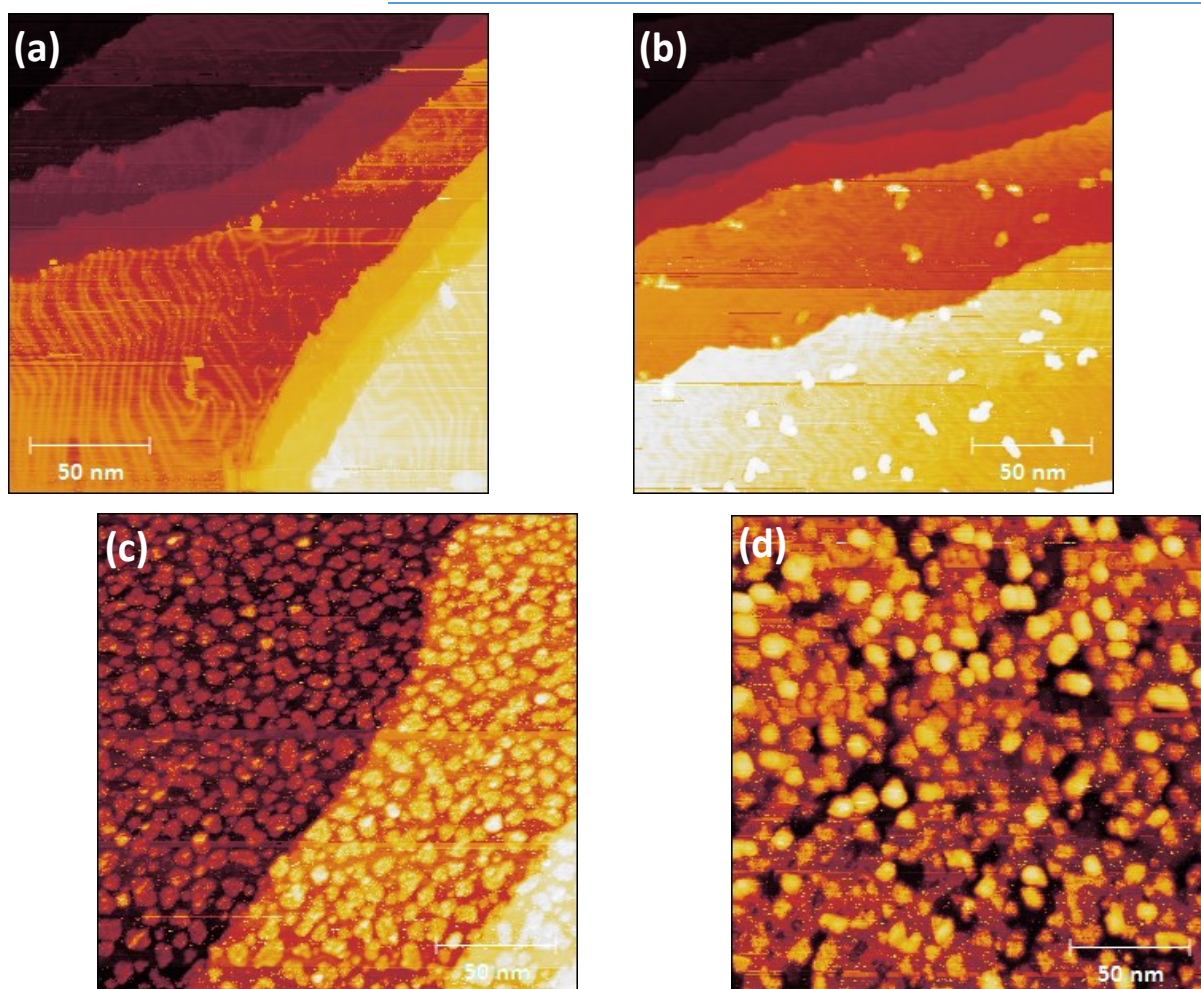
Figure 3.13(200x200) nm STM images of ZnO on Au(111) deposited by PLD: a) 125 mJ, 7 laser shots b) 200 mJ, 1 shot, c) 200 mJ, 5 shots, d) 200 mJ, 10 shots.

The images reported show the correct proportionality between the number of laser shots and the quantity of material obtained, but in none of them the structures formed present structural and morphological order, and the images themselves are disturbed.

It was hypothesized that the reason for this was an imperfect stoichiometry, caused by a loss of oxygen, in the deposited material, which made it unable to form regular zinc oxide structures. In order to verify this, the effect of the introduction of a second thermal treatment was studied.

Two samples were prepared by PLD, in identical conditions (200 mJ pulses, 4 laser shots, distance target-substrate 8 cm), and before the UHV post-annealing described earlier in this section, they were kept for 30 minutes at lower temperatures, about 540 K, one in vacuum
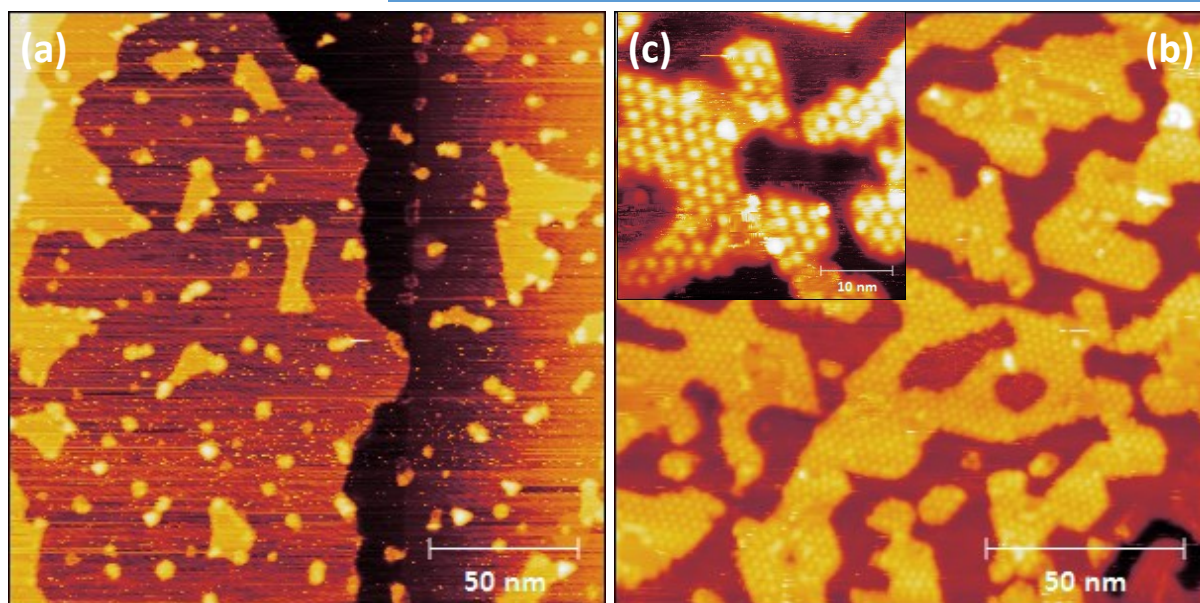
Figure 3.14 STM images of ZnO on Au(111) after 30 minutes of post-annealing: a) in UHV, (200x200) nm; b) and c) in oxygen atmosphere, (150x150) nm and (40x40) nm, respectively.

and the other in a $5*10^{-6}$ mbar pressure of O_2. In the second case, the thermal procedure coincided with the one utilized in the case of EB-PVD.

The results clearly indicated that even in the case of Pulsed Laser Deposition, where a stoichiometric zinc oxide target was used, a "post-oxidation" treatment was nevertheless of fundamental importance for the formation of high quality thin films. Figure 3.14a in fact, shows a STM image of the sample which was exposed to two UHV annealing processes, and it can be seen that only extremely small islands are still present upon the clean surface, along with atomically thin gold patches.

Figure 3.14b shows the same kind of interconnected structure which was already observed with e-beam deposition, and which exhibits very clearly the moiré pattern typical of graphene-like Zinc Oxide, displayed more clearly in the higher resolution Figure 3.14c. In several points the nucleation of another zinc oxide layer can be observed, and this small islands also present a moiré pattern.

Another difference with respect to the analysis presented in the previous section was that in the PLD chamber there were no delicate components, meaning that quite higher pressures were allowed, a fact that was exploited to study the effect of a wider range of oxygen pressure during Pulsed Laser Deposition.

The first aspect analyzed was the possibility to obtain layers of g-ZnO even when the system was not in high vacuum conditions. For this another set of depositions was carried out, in one the PLD chamber was maintained in UHV, in the other during the process oxygen was introduced in the chamber, until the pressure reached a stable value of $5*10^{-3}$ mbar.
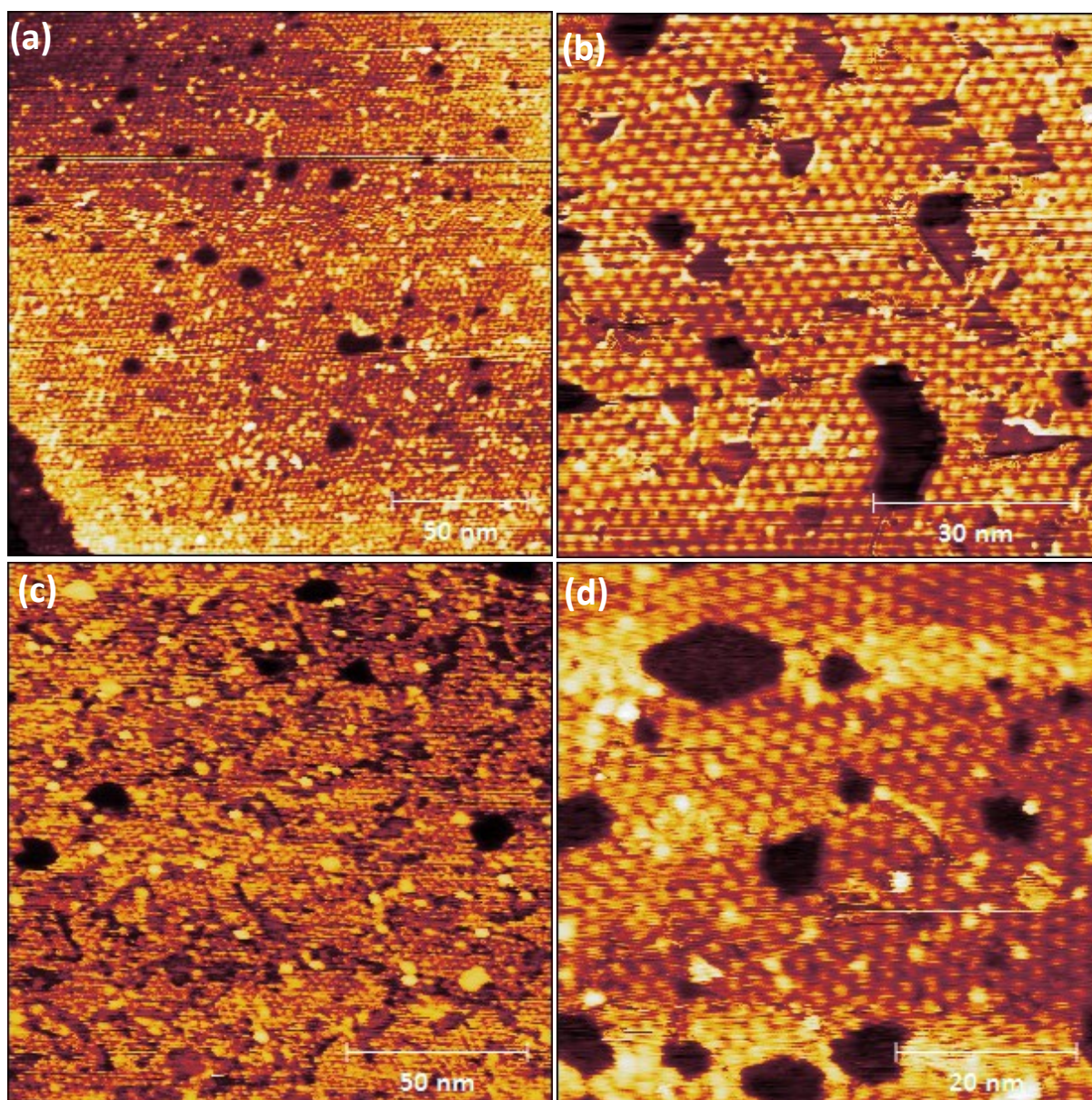

Figure 3.15 STM images of ZnO on Au(111): (a,b) deposition in vacuum and (c,d) deposition in $5*10^{-3}$ mbar O_2. (a,c) (150x150) nm; (b) (80x80) nm; (d) (60x60) nm.

The depositions were realized with 200 mJ pulses, 4 laser shots and a target-sample distance of 5 cm, anticipating that the presence of the oxygen atmosphere would have caused the quantity of material deposited to decrease. Both samples, before being examined with STM, were taken to the preparation chamber and subjected to the standard two-step thermal treatment, first in O_2 and then in UHV.

As it is shown in Figure 3.15, the two experiments showed extremely similar, and quite good, results: in both cases the gold surface was completely covered by an ordered layer of zinc oxide, presenting a clear moiré pattern, as highlighted by the higher resolution images, Figures 3.15b and 3.15d.

The small holes observed, are characterized for the most part by a hexagonal shape, whose edges follow the symmetry of the layer; it must be noted that the bottom of some of these holes also presents the moiré, suggesting that what is observed could be more than a single monolayer.

The only noticeable difference is an increase in the amount of gold surface which can be seen, this could be ascribed to an increased surface reconstruction or to a decreased coverage in the presence of the oxygen atmosphere.

The final analysis regarded the effect of an even higher O_2 pressure in the PLD chamber, and specifically if this increased oxygen presence during deposition resulted in the formation of ordered oxide structures even without the need for a subsequent post-oxidation process.

To study this, two similar depositions were again carried out, using the same parameters utilized above, but this time an oxygen pressure of $1*10^{-1}$ mbar was created in the PLD chamber before the lasing process.

The only difference between them resided in the thermal treatment they were exposed to: in one case it was the usual two-fold procedure, 30 minutes at 540 K in $5*10^{-6}$ mbar O_2, followed by 10 minutes at 600 K in UHV; in the other it consisted of only the UHV phase, but with the duration increased to 15 minutes.
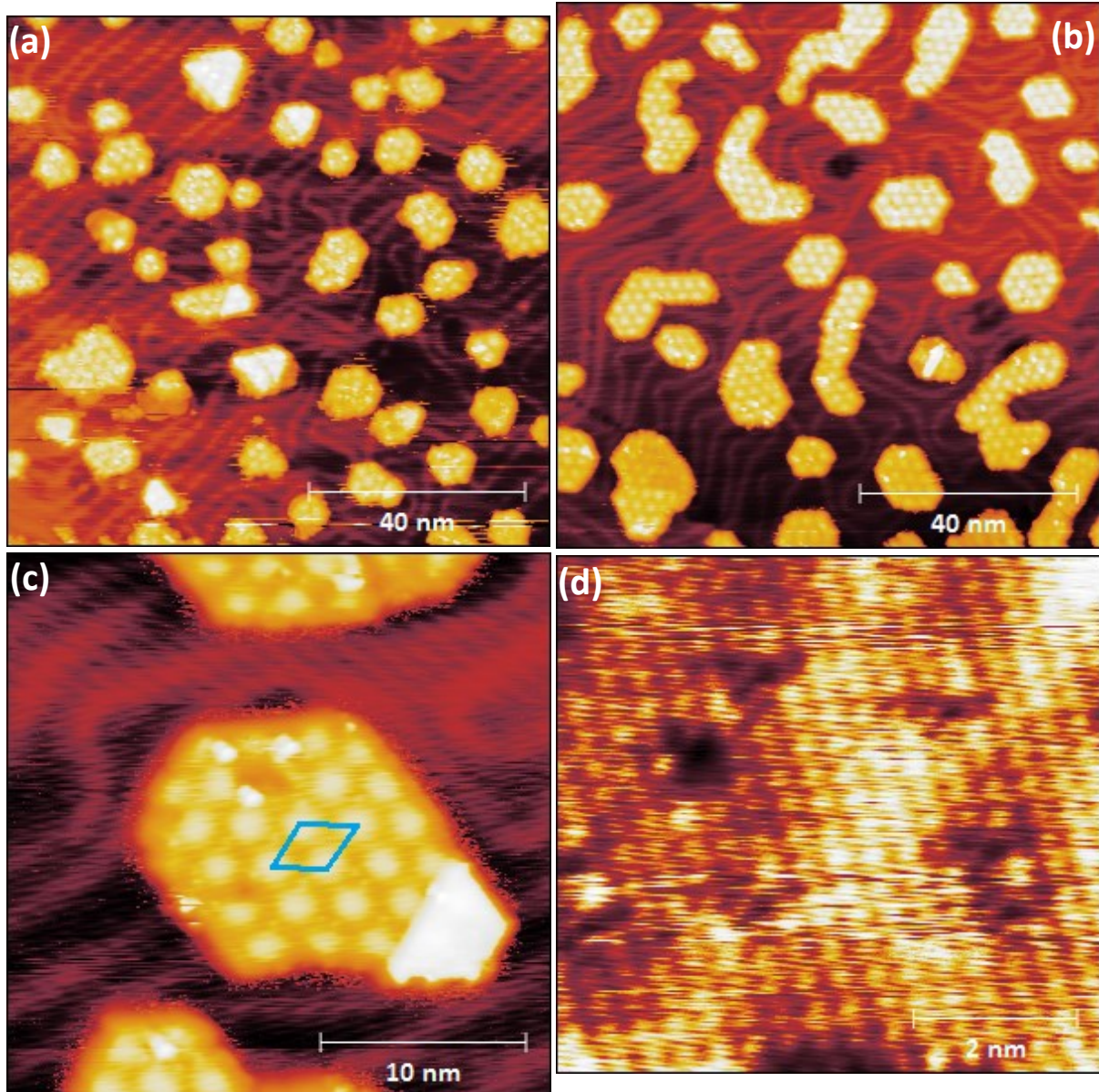
Figure 3.16 STM images of ZnO on Au(111): (a) post-annealing in UHV ,(b,c,d) post-annealing in O_2. (a,b) (100x100) nm; (c) (26x26) nm; (d) (7x7) nm.

As predictable, compared to the previous complete layers, the coverage obtained in the two experiments was lower, since the higher pressure caused the plasma plume to have stronger interactions with the background gas, and less of the ablated material was deposited.

STM images of the structures obtained with and without the post-oxidation phase are shown in Figure 3.16b and Figure 3.16a, respectively. In both, small ZnO islands of similar size were found upon the gold surface, which exhibited very clearly the characteristic herringbone reconstruction of Au(111).
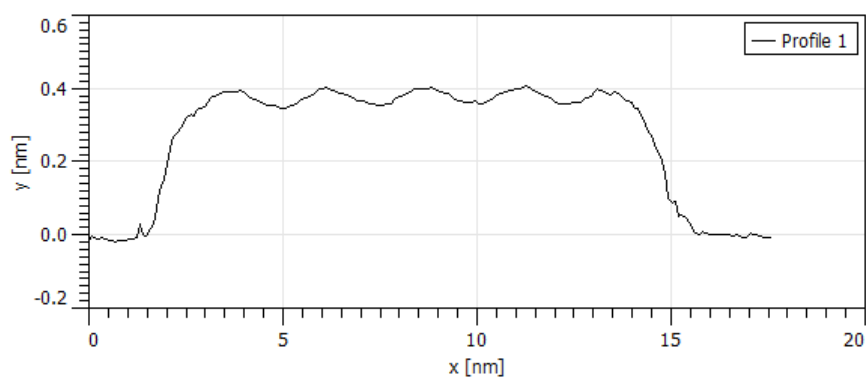
Figure 3.17 Line profile relative to the g-ZnO island of Figure 3.16c.

However, it can be seen that the shape of the islands in Figure 3.16a is more irregular, whereas in Figure 3.16b they show sharp edges, in most cases aligned along certain directions according to the symmetry of the substrate. Moreover, the moiré pattern, which is well-defined in the post-oxidized sample, can also be distinguished in the other image, but it's very disturbed and seems to present a lot of defects.

It can be said that, even if ZnO structures presenting a certain degree of regularity were obtained without the need for a post-oxidation treatment, thanks to the high O_2 pressure present in the chamber, the exposure to oxygen at high temperatures still causes a large increase in their quality.

A higher resolution, (26x26) nm, image of a single ZnO island is shown in Figure 3.16c, which indicates the structural order achieved in this deposition. The unit cell of the coincidence lattice is highlighted, whereas a line profile relative to this structure can be seen in Figure 3.17: the measured height from the gold surface to the peaks of the moiré was about 4 Å, the corrugation amplitude was 0.5 Å and the moiré lattice constant resulted being of approximately 2.6 nm.

Finally, Figure 3.16d is an atomic resolution STM image of the island's surface, which shows the hexagonal distribution of the ZnO atoms.

3.4 DISCUSSION OF THE RESULTS

From the experimental results presented in the previous Sections, and also comparing them to the information present in literature, some considerations can be made.

First of all, both deposition techniques considered, electron beam physical vapor deposition and pulsed laser deposition, resulted suitable for the formation of graphene-like zinc oxide on Au(111).

Attempts to form ordered ZnO structures by post-oxidation of previously deposited metallic zinc ultrathin films proved unsuccessful, probably due to difficulty in completely oxidizing zinc.

However, differently from what suggested by Deng et al.[30], it was possible to obtain g-ZnO on a gold substrate by reactive deposition in oxygen pressure, without the need for stronger oxidants such as NO_2.

Nevertheless, both with reactive deposition and with PLD, the exposure of the sample to oxygen at temperatures about 540 K for medium-long periods (~30'), was found to be of fundamental importance in order to obtain the desired morphology.

The fact that the observed moiré pattern has a prevalently electronical nature, which was suggested by Shiotari et al.[32], was also confirmed in our analysis, since the amplitude of the corrugation was greatly dependent on the applied voltage. Line profile measurements indicated that its height it's proportional to the modulus of the bias, and the moiré pattern effectively disappeared for values below ± 0.5 V.

Also, the disappearance of the pattern at low bias seems to deny the possibility of it being due to preferential adsorption of hydrogen, which was hypothesized in another study[31].

Over the course of this thesis, a standard thermal treatment was developed, which proved to be functional to the synthesis of high quality g-ZnO nanostructures in both of the deposition methods employed.

It consists of two phases, the first being 30 minutes at about 540 K in the presence of $5*10^{-6}$ mbar of O_2, with the objective to eliminate the possible oxygen deficiency in the deposit produced during the deposition process. The second was instead carried out in UHV, at higher

temperatures (about 600 K), in order to promote the reorganization of the material into ordered structures and the desorption of unstable deposit, as well as of other adsorbed elements.

The possibility to deposit graphene-like zinc oxide with relatively high pressures of oxygen was also explored, up to pressures of $1*10^{-1}$ mbar in the PLD chamber. This had never been done before in scientific literature, and the results were more than satisfactory, since, by varying the background pressure, both compact layers and small nanostructures of well-defined g-ZnO were obtained.

Focusing on the morphological analysis, a strong reconstruction of the Au(111) surface was observed, in both of the deposition approaches utilized, consisting in the formation of small atomic terraces, in an extent oftentimes proportional to the quantity of ZnO present. This was highlighted in previous studies regarding Ag(111), but not on gold substrates.

The graphene-like zinc oxide structures were seen to grow preferentially around or upon these gold island, and profile measurements showed a Au step height of 2.7 Å, with g-ZnO instead 1.3 Å higher than the surrounding gold. The nucleation of a second ZnO layer was also analyzed, and found to be about 2 Å high, for a total of 3.3 Å on the nearest gold level.

Based on these considerations, two possible interpretations regarding the growth of g-ZnO and its dimensions can be proposed.

The first is similar to that exposed by Deng, which observed the formation of "low-ZnO" and "high-ZnO" structures on the Au(111) surface, presenting heights of about 3.5 Å and 5.5 Å, respectively, and assumed them to represent the monolayer and bilayer of g-ZnO.

In this case, it could be hypothesized that the zinc monolayer is about 4 Å high, and that the deposition process causes the substitution of some of the atoms belonging the Au(111) with ZnO. By subtracting the atomic step of gold, 2.7 Å, this would account for the 1.3 Å high g-ZnO observed, and the nucleation of a second layer, 2 Å high as in the previous experimental data, would bring the total height to 3.3 Å with respect to the surrounding Au(111).

The second, and the one I support, based on the particular conformation of the observed nanostructures, hypothesizes a strong preference for g-ZnO to grow on these newly formed small gold islands, rather than on the background Au(111) surface.

In this way, the described 4 Å high structures would be gold islands, the surface of which is (almost) completely covered by a g-ZnO monolayer, characterized by an apparent height of 1.3 Å. On the other hand, 6 Å high elements would indicate the formation of a bilayer on the gold islands.

CONCLUSIONS AND PERSPECTIVES

In this thesis work it was reported the synthesis and a Scanning Tunnelig Microscopy (STM) study of the morphology of graphene-like zinc oxide (g-ZnO) on the Au(111) surface. The growth of g-ZnO was achieved by two different deposition methods, electron beam physical vapor deposition (EBPVD) and pulsed laser deposition (PLD).

The study focused especially on the impact of oxygen during the deposition process and/or during the following thermal treatment.

Considering EBPVD, the evaporant material utilized was pure zinc, and the exposure of previously deposited ultrathin films of metallic zinc to oxygen at high temperature was found to be insufficient to completely oxidize them.

Nevertheless, the formation of g-ZnO was obtained by means of reactive deposition, i.e. establishing an O_2 atmosphere in the chamber during the deposition process. This is in contrast to the previously reported[30] need for stronger oxidant agents, such as NO_2.

In PLD, the target employed was composed by stoichiometric zinc oxide, which should have caused this deposition method to not require a subsequent post-oxidation procedure. This was however found to be partially untrue, and exposure to oxygen at high temperatures proved to have a great effect on the quality of the nanostructures formed.

In fact, a single post-deposition thermal treatment was experimentally found to be optimal for both the deposition techniques used in this thesis, and consisted of two separate phases: first the sample was kept for about half an hour at 540 K in the presence of $5*10^{-6}$ mbar of O_2, in order to promote the complete oxidation of the deposited material; then the oxygen was removed and the temperature was raised to 600 K for ten minutes, to cause the release of adsorbed species and further stimulate the creation of ordered structures.

The main way utilized in this thesis to confirm that what was observed was actually graphitic zinc oxide, was to verify that the surface of the deposited structures showed the moiré pattern. This is, generally speaking, a periodic pattern generated by the superposition of two

factors which are characterized by different lattices, which results in the formation of a coincidence lattice.

In this particular case, it was due to the fact that the Zn and O atoms find themselves on different positions with respect to the gold lattice underneath, and shared the hexagonal symmetry of both g-ZnO and Au(111). This phenomenon was observed in most of the experimental articles regarding STM characterization of g-ZnO.

The data obtained with STM measurements presents both a morphological and an electronic nature. In this thesis, the moiré pattern of two-dimensional zinc oxide was confirmed to be for the most part caused by a corrugation in the electronic states of the system: in fact, its amplitude resulted greatly dependent on the applied bias, vanishing for voltage values below ±0.5 V.

By using PLD it was possible to study the possibility of carrying out the zinc oxide depositions at relatively high oxygen pressures, up to $1*10^{-1}$ mbar. The experiment were successful, and apart from a lower quantity of material deposited, because of opposition of the oxygen to the plume's expansion, no meaningful morphological differences were observed.

The variation in the morphology of the nanostructures with respect to the quantity of deposit present was also analyzed: small, prevalently hexagonal islands were found to grow and coalesce into interconnected polygonal planar structures, eventually resulting in the formation of complete g-ZnO layers. In the first two conditions, a strong preferential directionality of the structures' edges was also observed.

Finally, an interpretation of the g-ZnO/Au(111) system morphology, different from that previously found in literature, has been proposed. It revolves on the formation, during the deposition process, of small gold terraces, one atomic step high, by reconstruction of the Au(111) surface in presence of the deposit and of heat, which were not present on the cleaned substrate.

This phenomenon was earlier described in the synthesis of two-dimensional zinc oxide on Ag(111)[32], but not in the case of Au(111).

The islands provide sites of preferential growth for g-ZnO, which tends to almost completely cover them, with only a small quantity of zinc oxide growing directly on the background

Au(111) surface. A similar phenomenon is observed on the steps of bulk gold, where g-ZnO is often seen growing upon the step edges.

Profile measurements indicated that the gold steps were 2.7 Å high, whereas the zinc oxide monolayer was characterized by an apparent height of 1.3 Å. Increasing the quantity of material deposited, the nucleation of a new layer on the larger g-ZnO surfaces was observed, and this new structures resulted 2 Å higher.

Following these considerations, I suggest that the previously described[30] ~3.5 Å "low-ZnO" and ~3.5 Å "high-ZnO" structures, do not simply represent the morphology of respectively the g-ZnO monolayer and bilayer.

Instead, they are composed of small gold islands, upon which one or two layers of graphene-like zinc oxide have grown. The data relative to the apparent heights of this elements is consistent with this interpretation.

Since this thesis focused on the synthesis process and on the morphological analysis, further studies can be considered in order to investigate the electronic properties of graphene-like ZnO, specifically by means of Scanning Tunneling Spectroscopy.

Another aspect which has not been examined is the possibility of obtaining doped g-ZnO, for example with Aluminum, which very recent studies[67] have found to be a stable compound, and the analysis of the changes in the properties of graphene-like zinc oxide induced by this doping.

It could be also interesting to expand the synthesis of g-ZnO to substrates characterized by a non-hexagonal surface symmetry, and observing whether the morphology of the obtained nanostructures is different and how.

Finally, as more of a long term goal, the possible use of g-ZnO in future layered heterostructures could be examined, for example by trying to deposit it on HOPG or on MoS_2. The synthesis of graphene on the surface of g-ZnO could be particularly interesting, since, as mentioned earlier, ab initio studies[27,28] have found that this system could preserve the exciting electronic properties of free-standing graphene.

BIBLIOGRAPHY

[1] Miró, P., Audiffred, M., & Heine, T. (2014). An atlas of two-dimensional materials. Chemical Society Reviews, 43(18), 6537-6554.

[2] Yang, G., Zhu, C., Du, D., Zhu, J., & Lin, Y. (2015). Graphene-like two-dimensional layered nanomaterials: applications in biosensors and nanomedicine. Nanoscale, 7(34), 14217-14231.

[3] Xu, M., Liang, T., Shi, M., & Chen, H. (2013). Graphene-like two-dimensional materials. Chemical reviews, 113(5), 3766-3798.

[4] Novoselov, K. S., Geim, A. K., Morozov, S. V., Jiang, D., Zhang, Y., Dubonos, S. A., ... & Firsov, A. A. (2004). Electric field effect in atomically thin carbon films. Science, 306(5696), 666-669.

[5] Nair, R. R., Blake, P., Grigorenko, A. N., Novoselov, K. S., Booth, T. J., Stauber, T., ... & Geim, A. K. (2008). Fine structure constant defines visual transparency of graphene. Science, 320(5881), 1308-1308.

[6] Gupta, A., Sakthivel, T., & Seal, S. (2015). Recent development in 2D materials beyond graphene. Progress in Materials Science, 73, 44-126.

[7] Mak, K. F., He, K., Shan, J., & Heinz, T. F. (2012). Control of valley polarization in monolayer MoS2 by optical helicity. Nature nanotechnology, 7(8), 494-498.

[8] Pacchioni, G. (2012). Two-Dimensional Oxides: Multifunctional Materials for Advanced Technologies.Chemistry-A European Journal, 18(33), 10144-10158.

[9] Tumino, F., Carrozzo, P., Mascaretti, L., Casari, C. S., Passoni, M., Tosoni, S., ... & Bassi, A. L. (2015). Two-dimensional TiO x nanostructures on Au (111): a scanning tunneling microscopy and spectroscopy investigation. 2D Materials, 2(4), 045011.

[10] Özgür, Ü., Alivov, Y. I., Liu, C., Teke, A., Reshchikov, M., Doğan, S., ... & Morkoc, H. (2005). A comprehensive review of ZnO materials and devices. Journal of applied physics, 98(4), 041301.

[11] Diebold, U., Koplitz, L. V., & Dulub, O. (2004). Atomic-scale properties of low-index ZnO surfaces.Applied Surface Science, 237(1), 336-342.

[12] Dulub, O., Boatner, L. A., & Diebold, U. (2002). STM study of the geometric and electronic structure of ZnO (0001)-Zn,(0001)-O,(1010), and (1120) surfaces.Surface Science, 519(3), 201-217.

[13] Kołodziejczak-Radzimska, A., & Jesionowski, T. (2014). Zinc oxide—from synthesis to application: a review. Materials, 7(4), 2833-2881.

[14] Claeyssens, F., Freeman, C. L., Allan, N. L., Sun, Y., Ashfold, M. N., & Harding, J. H. (2005). Growth of ZnO thin films—experiment and theory. Journal of Materials Chemistry, 15(1), 139-148.

[15] Freeman, C. L., Claeyssens, F., Allan, N. L., & Harding, J. H. (2006). Graphitic nanofilms as precursors to wurtzite films: theory. Physical review letters, 96(6), 066102.

[16] Tang, Q., & Zhou, Z. (2013). Graphene-analogous low-dimensional materials. Progress in Materials Science, 58(8), 1244-1315.

[17] Topsakal, M., Cahangirov, S., Bekaroglu, E., & Ciraci, S. (2009). First-principles study of zinc oxide honeycomb structures. Physical Review B, 80(23), 235119.

[18] Tu, Z. C. (2010). First-principles study on physical properties of a single ZnO monolayer with graphene-like structure. Journal of Computational and Theoretical Nanoscience, 7(6), 1182-1186.

[19] Kang, J., Zhang, Y., Wen, Y. H., Zheng, J. C., & Zhu, Z. Z. (2010). First-principles study on the structural and electronic properties of ultrathin ZnO nanofilms. Physics Letters A, 374(8), 1054-1058.

[20] Peng, Q., Liang, C., Ji, W., & De, S. (2013). A first principles investigation of the mechanical properties of g-ZnO: the graphene-like hexagonal zinc oxide monolayer. Computational Materials Science, 68, 320-324.

[21] Schmidt, T. M., Miwa, R. H., & Fazzio, A. (2010). Ferromagnetic coupling in a Co-doped graphenelike ZnO sheet. Physical Review B, 81(19), 195413.

[22] Guo, H., Zhao, Y., Lu, N., Kan, E., Zeng, X. C., Wu, X., & Yang, J. (2012). Tunable magnetism in a nonmetal-substituted ZnO Monolayer: a first-principles study. The Journal of Physical Chemistry C, 116(20), 11336-11342.

[23] Tang, Q., Li, Y., Zhou, Z., Chen, Y., & Chen, Z. (2010). Tuning electronic and magnetic properties of wurtzite ZnO nanosheets by surface hydrogenation. ACS applied materials & interfaces, 2(8), 2442-2447.

[24] Chen, Q., Wang, J., Zhu, L., Wang, S., & Ding, F. (2010). Fluorination induced half metallicity in two-dimensional few zinc oxide layers. The Journal of chemical physics, 132(20), 204703.

[25] Behera, H., & Mukhopadhyay, G. (2012). Strain-tunable band parameters of ZnO monolayer in graphene-like honeycomb structure. Physics Letters A, 376(45), 3287-3289.

[26] Das, R., Rakshit, B., Debnath, S., & Mahadevan, P. (2014). Microscopic model for the strain-driven direct to indirect band-gap transition in monolayer MoS_2 and ZnO. Physical Review B, 89(11), 115201.

[27] Hu, W., Li, Z., & Yang, J. (2013). Electronic and optical properties of graphene and graphitic ZnO nanocomposite structures. The Journal of chemical physics, 138(12), 124706.

[28] Yao, Q., Liu, Y., Lu, R., Xiao, C., Deng, K., & Kan, E. (2014). Will a graphitic-like ZnO single-layer be an ideal substrate for graphene? RSC Advances, 4(34), 17478-17482.

[29] Tusche, C., Meyerheim, H. L., & Kirschner, J. (2007). Observation of depolarized ZnO(0001) monolayers: formation of unreconstructed planar sheets. Physical review letters, 99(2), 026102.

[30] Deng, X., Yao, K., Sun, K., Li, W. X., Lee, J., & Matranga, C. (2013). Growth of single-and bilayer ZnO on Au(111) and interaction with Copper. The Journal of Physical Chemistry C, 117(21), 11211-11218.

[31] Stavale, F., Pascua, L., Nilius, N., & Freund, H. J. (2013). Morphology and luminescence of ZnO films grown on a Au(111) support. The Journal of Physical Chemistry C, 117(20), 10552-10557.

[32] Shiotari, A., Liu, B. H., Jaekel, S., Grill, L., Shaikhutdinov, S., Freund, H. J., ... & Kumagai, T. (2014). Local Characterization of Ultrathin ZnO Layers on Ag(111) by Scanning Tunneling

Microscopy and Atomic Force Microscopy. The Journal of Physical Chemistry C, 118(47), 27428-27435.

[33]Weirum, G., Kratzer, M., Koch, H. P., Tamtögl, A., Killmann, J., Bako, I., ... & Schennach, R. (2009). Growth and desorption kinetics of ultrathin Zn layers on Pd(111). The Journal of Physical Chemistry C, 113(22), 9788-9796.

[34] Weirum, G., Barcaro, G., Fortunelli, A., Weber, F., Schennach, R., Surnev, S., & Netzer, F. P. (2010). Growth and surface structure of zinc oxide layers on a Pd(111) surface. The Journal of Physical Chemistry C, 114(36), 15432-15439.

[35]Martynova, Y., Liu, B. H., McBriarty, M. E., Groot, I. M. N., Bedzyk, M. J., Shaikhutdinov, S., & Freund, H. J. (2013). CO oxidation over ZnO films on Pt(111) at near-atmospheric pressures. Journal of Catalysis, 301, 227-232.

[36]Liu, B. H., McBriarty, M. E., Bedzyk, M. J., Shaikhutdinov, S., & Freund, H. J. (2014). Structural Transformations of Zinc Oxide Layers on Pt(111).The Journal of Physical Chemistry C, 118(49), 28725-28729.

[37]Liu, B. H., Boscoboinik, J. A., Cui, Y., Shaikhutdinov, S., & Freund, H. J. (2015). Stabilization of Ultrathin Zinc Oxide Films on Metals: Reconstruction versus Hydroxylation. The Journal of Physical Chemistry C, 119(14), 7842-7847.

[38] Pan, Q., Liu, B. H., McBriarty, M. E., Martynova, Y., Groot, I. M. N., Wang, S., ... & Freund, H. J. (2014). Reactivity of Ultra-Thin ZnO Films Supported by Ag(111) and Cu(111): A Comparison to ZnO/Pt(111).Catalysis letters, 144(4), 648-655.

[39] Roos, E., Maile, K., Lyutovich, A., Gusko, A., & Udoh, A. (2002). (Cr–Al) bi-layer coatings obtained by ion assisted EB PVD on C/C–SiC composites and Ni-based alloys. Surface and Coatings Technology,151, 429-433.

[40] Ohring, M. (2001). Materials science of thin films. Academic press.

[41] Singh, J., Quli, F., Wolfe, D. E., Schriempf, J. T., & Singh, J. (1999). An Overview: Electron Beam-Physical Vapor Deposition Technology-Present and Future Applications. Applied Research Laboratory, Pennsylvania State University, USA.

[42] Lupis, C. H. (1983). Thermodynamics of Materials.

[43] Chrisey, D. B., & Hubler, G. K. (Eds.). (1994). Pulsed laser deposition of thin films.

[44] Smith, H. M., & Turner, A. F. (1965). Vacuum deposited thin films using a ruby laser. Applied optics, 4(1), 147-148.

[45] Singh, R. K., & Narayan, J. (1990). Pulsed-laser evaporation technique for deposition of thin films: Physics and theoretical model. Physical Review B,41(13), 8843.

[46] Voevodin, A. A., Shtansky, D. V., Levashov, E. A., & Moore, J. J. (Eds.). (2006). Nanostructured thin films and nanodispersion strengthened coatings (Vol. 155). Springer Science & Business Media.

[47] Ashfold, M. N., Claeyssens, F., Fuge, G. M., & Henley, S. J. (2004). Pulsed laser ablation and deposition of thin films. Chemical Society Reviews,33(1), 23-31.

[48] Binnig, G., Rohrer, H., Gerber, C., & Weibel, E. (1982). Surface studies by scanning tunneling microscopy. Physical review letters, 49(1), 57.

[49] Bardeen, J. (1961). Tunnelling from a many-particle point of view. Physical Review Letters, 6(2), 57.

[50] Tersoff, J., & Hamann, D. R. (1983). Theory and application for the scanning tunneling microscope.Physical review letters, 50(25), 1998.

[51] Tersoff, J., & Hamann, D. R. (1993). Theory of the scanning tunneling microscope. In Scanning Tunneling Microscopy (pp. 59-67). Springer Netherlands.

[52] Ohnishi, S., & Tsukada, M. (1989). Molecular orbital theory for the scanning tunneling microscopy. Solid State Communications, 71(5), 391-394.

[53] Tsukada, M., Kobayashi, K., & Ohnishi, S. (1990). First-principles theory of the scanning tunneling microscopy simulation. Journal of Vacuum Science & Technology A, 8(1), 160-165.

[54] Tsukada, M., Kobayashi, K., Isshiki, N., & Kageshima, H. (1991). First-principles theory of scanning tunneling microscopy. Surface Science Reports, 13(8), 267-304.

[55] Doyen, G., Koetter, E., Vigneron, J. P., & Scheffler, M. (1990). Theory of scanning tunneling microscopy.Applied Physics A, 51(4), 281-288.

[56] Chen, C. J. (1990). Origin of atomic resolution on metal surfaces in scanning tunneling microscopy.Physical review letters, 65(4), 448.

[57] Chen, C. J. (1990). Tunneling matrix elements in three-dimensional space: The derivative rule and the sum rule. Physical Review B, 42(14), 8841.

[58] Chen, C. J. (2008). Introduction to scanning tunneling microscopy. Oxford University Press.

[59] Besenbacher, F. (1996). Scanning tunnelling microscopy studies of metal surfaces. Reports on Progress in Physics, 59(12), 1737.

[60] Wöll, C., Chiang, S., Wilson, R. J., & Lippel, P. H. (1993). Determination of atom positions at stacking-fault dislocations on Au (111) by scanning tunneling microscopy. In Scanning Tunneling Microscopy (pp. 114-117). Springer Netherlands.

[61] Harten, U., Lahee, A. M., Toennies, J. P., & Wöll, C. (1985). Observation of a soliton reconstruction of Au (111) by high-resolution helium-atom diffraction.Physical review letters, 54(24), 2619.

[62] Casari, C. S., Foglio, S., Siviero, F., Bassi, A. L., Passoni, M., & Bottani, C. E. (2009). Direct observation of the basic mechanisms of Pd island nucleation on Au (111). Physical Review B, 79(19), 195402.

[63] Barth, J. V., Brune, H., Ertl, G., & Behm, R. J. (1990). Scanning tunneling microscopy observations on the reconstructed Au (111) surface: Atomic structure, long-range superstructure, rotational domains, and surface defects. Physical Review B,42(15), 9307.

[64] Bulou, H., & Goyhenex, C. (2002). Local strain analysis of the herringbone reconstruction of Au (111) through atomistic simulations. Physical Review B, 65(4), 045407.

[65] Barth, J. V., Brune, H., Ertl, G., & Behm, R. J. (1990). Scanning tunneling microscopy observations on the reconstructed Au (111) surface: Atomic structure, long-range superstructure, rotational domains, and surface defects. Physical Review B,42(15), 9307.

[66] Meyer, J. A., Baikie, I. D., Kopatzki, E., & Behm, R. J. (1996). Preferential island nucleation at the elbows of the Au (111) herringbone reconstruction through place exchange. Surface science, 365(1), L647-L651.

[67] Ma, D., Wang, Q., Li, T., Tang, Z., Yang, G., He, C., & Lu, Z. (2015). CO catalytic oxidation on Al-doped graphene-like ZnO monolayer sheets: a first-principles study. Journal of Materials Chemistry C,3(38), 9964-9972.